



DISSERTATION

# High Precision Neutron Polarization For PERC

ausgeführt zum Zwecke der Erlangung des akademischen Grades eines  
Doktors der Naturwissenschaften unter der Leitung von

**Univ.-Prof.Dipl.-Phys. Dr.rer.nat Hartmut Abele**

E141-Atominstitut

und unter Zweitbetreuung durch

**Dr.rer.nat Dipl.- Phys. Torsten Soldner**

Institut Laue-Langevin, F-Grenoble

eingereicht an der Technischen Universität Wien  
bei der Fakultät für Physik

von

**Christine Klauser, MSc.**

Matrikelnummer 1029662

25 rue Lachmann, F-38000 Grenoble

Wien, im Oktober 2013



Ihr zahmen Täubchen, ihr  
Turteltäubchen, all ihr Vöglein  
unter dem Himmel, kommt und  
helft mir lesen, die guten ins  
Töpfchen, die schlechten ins  
Kröpfchen.

---

Jakob und Wilhelm Grimm, Die  
schönsten Kinder- und  
Hausmärchen [1]





## Kurzfassung

Der Zerfall des freien Neutrons in Proton, Elektron und Anti-Elektron-Neutrino ist ein einfaches System, welches erlaubt, den semi-leptonischen Zerfall in der schwachen Wechselwirkung zu untersuchen. Hochpräzisionsmessungen von Winkelkorrelationskoeffizienten dieses Zerfalls sind eine Möglichkeit, das Standardmodell der Teilchenphysik zu prüfen. Der Proton Electron Radiation Channel PERC ist Teil einer neuen Generation von Experimenten, welche die Messung solcher Winkelkorrelationskoeffizienten mit einer Genauigkeit von  $10^{-4}$  zum Ziel haben. Vergangene Experimente waren auf eine Genauigkeit von  $10^{-3}$  beschränkt, wobei einer der größten systematischen Fehler die Ungenauigkeit der Neutronenpolarisation war. Diese Dissertation beschäftigt sich mit der Entwicklung einer stabilen, hochpräzisen Neutronenpolarisation für einen divergenten kalten Neutronenstrahl mit großem Querschnitt. Die "Opaque Test Bench", ein Versuchsaufbau welcher den Strahl auf mehr als 99.99% polarisiert und ihn mit einer Genauigkeit von  $10^{-4}$  analysiert, wird beschrieben und validiert. Es besteht aus zwei stark opaken polarisierten Heliumzellen.

Depolarisierende Effekte in polarisierenden Superspiegeln, welche üblicherweise zur Polarisation in Neutronenzerfallsexperimenten benutzt werden, werden in der Opaque Test Bench offenbar. Diese Effekte werden detailliert untersucht. Sie sind durch imperfekte laterale Magnetisierung in den einzelnen Superspiegelschichten bedingt und können durch ein signifikant erhöhtes Magnetfeld sowie durch kleine Einfallswinkel und die Verwendung kleiner m-Werte minimiert werden. In einem daraus folgendem Test in der gekreuzten (X-SM) Geometrie wurden Polarisationen nur durch Superspiegel bis zu 99.97% gemessen. Dies verbessert die Neutronenpolarisation durch Superspiegel um eine Größenordnung.

Diese Dissertation untersucht ferner andere neutronenoptische Komponenten der PERC Beamline. So wurden Monte-Carlo-Simulationen der Beamline zum Primärleiter durchgeführt. Zudem wurde durch Rechnung gezeigt, dass ein Aufbau von PERC an der European Spallation Source statistische vorteilhaft wäre. Des Weiteren wurden Beamline-Komponenten experimentell getestet. Die Effizienz eines Radiofrequenz-Spinflippers wurde als besser als 0.9999 bestimmt.



## Abstract

The decay of the free neutron into a proton, an electron and an anti-electron neutrino offers a simple system to study the semi-leptonic weak decay. High precision measurements of angular correlation coefficients of this decay provide the opportunity to test the standard model on the low energy frontier. The Proton Electron Radiation Channel PERC is part of a new generation of experiments pushing the accuracy of such an angular correlation coefficient measurement towards  $10^{-4}$ . Past experiments have been limited to an accuracy of  $10^{-3}$  with uncertainties on the neutron polarization as one of the leading systematic errors. This thesis focuses on the development of a stable, highly precise neutron polarization for a large, divergent cold neutron beam. A diagnostic tool that provides polarization higher than 99.99 % and analyzes with an accuracy of  $10^{-4}$ , the Opaque Test Bench, is presented and validated. It consists of two highly opaque polarized helium cells. The Opaque Test Bench reveals depolarizing effects in polarizing supermirrors commonly used for polarization in neutron decay experiments. These effects are investigated in detail. They are due to imperfect lateral magnetization in supermirror layers and can be minimized by significantly increased magnetizing fields and low incidence angle and supermirror factor  $m$ . A subsequent test in the crossed (X-SM) geometry demonstrated polarizations up to 99.97% from supermirrors only, improving neutron polarization with supermirrors by an order of magnitude. The thesis also discusses other neutron optical components of the PERC beamline: Monte-Carlo simulations of the beamline under consideration of the primary guide are carried out. In addition, calculation shows that PERC would statistically profit from an installation at the European Spallation source. Furthermore, beamline components were tested. A radio-frequency spin flipper was confirmed to work with an efficiency higher than 0.9999.



# Contents

<b>1</b>	<b>Introduction</b>	<b>1</b>
<b>2</b>	<b>Polarized Neutron Beta Decay</b>	<b>3</b>
2.1	The Neutron Weak Decay . . . . .	4
2.2	Polarized Asymmetry Measurements . . . . .	5
2.3	The PERC instrument . . . . .	7
<b>3</b>	<b>Polarization Methods</b>	<b>11</b>
3.1	Polarization Analysis . . . . .	12
3.2	Spin Manipulation . . . . .	15
3.3	Polarizing Methods . . . . .	16
3.3.1	Stern-Gerlach Effect . . . . .	16
3.3.2	Polarizing Crystals . . . . .	17
3.3.3	Polarizing Mirrors and Supermirrors . . . . .	17
3.3.4	Helium Spin Filter . . . . .	22
<b>4</b>	<b>Polarizer Experiments</b>	<b>26</b>
4.1	The Opaque Test Bench . . . . .	28
4.1.1	Set-up And Data Acquisition . . . . .	28
4.1.2	Data Analysis And Error Treatment . . . . .	30
4.2	Depolarization Measurements In Polarizing Mirrors . . . . .	35
4.2.1	Samples . . . . .	37
4.2.2	The Experimental Set-up . . . . .	39
4.2.3	General Observations . . . . .	45
4.2.4	Individual Layers . . . . .	52
4.2.5	Pseudo-Supermirrors . . . . .	62
4.2.6	Depolarization By A Bender . . . . .	62
4.2.7	Summary . . . . .	63

4.3	Depolarization By Beamline Elements . . . . .	64
4.3.1	Aluminium Window . . . . .	64
4.3.2	Flipper . . . . .	65
4.4	Single Polarizing Supermirrors . . . . .	67
4.5	Polarizing Supermirrors In Crossed Geometry . . . . .	70
<b>5</b>	<b>PERC beamline</b>	<b>72</b>
5.1	Optimization Of The Primary Guide Coating . . . . .	74
5.1.1	Simulation Method: McStas . . . . .	74
5.1.2	Beamline Set-Up . . . . .	75
5.1.3	Supermirror Coatings Of The Primary Guide . . . . .	76
5.1.4	Beam Characterization At The End Of The Primary Guide . . . . .	80
5.1.5	Coating Of The PERC Guide . . . . .	83
5.2	PERC At ESS . . . . .	86
5.2.1	Continuous Source . . . . .	87
5.2.2	Pulsed Source . . . . .	89
5.2.3	Comparison and Optimizing Parameters . . . . .	91
<b>6</b>	<b>Conclusion</b>	<b>94</b>
6.1	Comparison Of Polarization Methods . . . . .	95
6.2	Future Work . . . . .	98
	<b>Bibliography</b>	<b>101</b>
	<b>A Reflectivity Curves of Samples From T3</b>	<b>109</b>
	<b>B PERC in McStas</b>	<b>116</b>

# 1

## Introduction

The standard model of particle physics is a successful theory describing the strong, weak and electro-magnetic interactions of elementary particles. All of the particles it predicts have been experimentally confirmed. Nevertheless, several experimental observations are in disagreement with the standard model. These observations include neutrino oscillations and dark matter and dark energy. Gravity, one of the four fundamental forces, is not included and the hierarchy between the range of gravity and the electro-weak nuclear force remains without explanation. Theories overcoming some or all of the standard models shortcomings have been developed. The weak decay of the free neutron offers a tool to test these and the standard model on the high-precision frontier by asymmetry measurements on angular correlation coefficients with high accuracy. The Proton Electron Radiation Channel PERC is part of a new generation of instruments pushing the accuracy of such an angular correlation coefficient measurement towards  $10^{-4}$ . PERC is going to be built at the FRMII reactor in Garching, Germany. Past experiments have been limited to an accuracy of  $10^{-3}$ , where the uncertainty on the neutron polarization was one of the leading systematic errors. This thesis focuses on the development of a stable, highly precise neutron polarization for a large,

divergent cold neutron beam on the level of  $10^{-4}$ .

Chap. 2 discusses the weak decay and correlation coefficients of the polarized neutron decay. The PERC instrument is presented. Chap. 3 gives an overview over current neutron polarization methods and polarimetry. Particular attention is given to the methods that allow a polarization of a polychromatic, divergent, large cold neutron beam: polarized helium filters and supermirrors. In Chap. 4, the experimental results of this thesis are being resumed. A diagnostic tool based on opaque helium filters, the Opaque Test Bench, is presented and validated. It is used to study depolarization in polarizing supermirrors. The outcome of a close investigation in this depolarization is given account of, studying several parameters such as material, magnetizing field, supermirror factor and incidence angle and wavelength. The results are applied to a measurement of a polarizer in the crossed geometry and improvements are shown. Furthermore, this chapter also includes results on depolarization by beamline components. Chap. 5 discusses the PERC beamline from a neutron optical point of view. Monte-Carlo simulations for the beamline are presented, focusing mainly on the supermirror coating of the guide connecting the reactor and the PERC experiment. In addition, the installation of PERC at the future European Spallation Source ESS is discussed. Chap. 6 summarizes the results and compares and contrasts the polarization methods presented and discusses further work necessary for a satisfying polarization performance on the PERC beamline.



# 2

## Polarized Neutron Beta Decay

The Standard Model of particle physics is described by a gauge group  $U(1)_{\text{charge}} \times SU(2)_{\text{weak}} \times SU(3)_{\text{color}}$ . It unifies three of the four fundamental forces: electromagnetism, strong and weak interactions that occur between the fundamental group of particles composed by  $2 \times 3$  hadrons and  $2 \times 3$  leptons. The Standard Model is a very successful theory as all particles predicted by it have been experimentally confirmed. However, it fails short to explain some phenomena such as the neutrino mass, the different scales of interaction for the electro-weak force and gravity (not included in the Standard Model), the nature of dark energy and dark matter, as well as the asymmetry between matter and anti-matter in the universe. Multiple theories that include these observations are being developed. In order to test these against the Standard Model, two approaches are possible: a) The high energy approach focuses on creating new particles that might be linked to a novel theory and have not been found at energies already experimentally available. b) The high precision approach concentrates on effects which this new physics might have at a low energy level that distinguishes it from the Standard Model physics. Here, detection of new particles is not aimed at, rather, their influence on already well-observed particles is being studied.

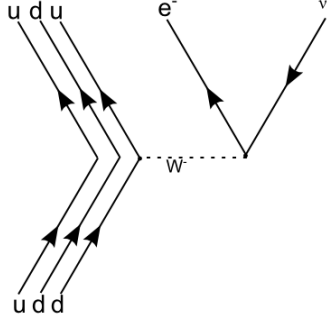


Figure 2.1: The weak decay of a neutron on the quark level

Such effects must be very small, as the Standard Model already applies to a low energy level, and require a high precision in the experiment. The neutron beta decay is one possibility to perform such high precision experiments.

## 2.1 The Neutron Weak Decay

A neutron is composed of two down and one up-quarks. The overall charge is zero, the spin is  $\frac{1}{2}$  and the mass is roughly  $939 \text{ MeV}/c^2$ . The free neutron has a lifetime of about 880 seconds [2]. Neutrons are being attributed a de Broglie-wavelength:  $\lambda = \frac{h}{p} \approx \frac{h}{m_n v} = k \frac{1}{v} \approx 3956 \frac{1}{v} [\frac{\text{m} \cdot \text{\AA}}{\text{s}}]$ . The neutron decays via the weak interaction  $W^-$ -boson, one d quark of the neutron is changed into a u quark, forming a proton and the virtual  $W^-$ -boson decays into an electron and an anti-electron-neutrino, see Fig. 2.1 [2]:

$$n \rightarrow p + e^- + \bar{\nu}_e. \quad (2.1)$$

Due to the high mass of the interaction bosons, the weak force is a short-range force. The lepton spin can couple to the total spin  $S=0$  (Fermi transition,  $\Delta I=0$  for the nucleons) or to  $S=1$  (Gamow-Teller transition,  $\Delta I=0,1$  for the nucleons), see Tab. 2.1.

The weak decay as it is currently described by the Standard Model has a term for each the hadronic interaction and the leptonic nod. It is a so called V-A decay where V stands for the vectorial coupling and A for the axial coupling. On the quark and lepton level in the Standard Model, the coupling constants  $g$  are 1 and -1, respectively. The hadronic interaction in

interaction	$\vec{\sigma}_n$	$\vec{\sigma}_e + \vec{\sigma}_\nu$	S
Fermi	$\uparrow$	$\uparrow\downarrow - \downarrow\uparrow$	0
Gamow-Teller	$\uparrow$	$\uparrow\uparrow$	1
	$\uparrow$	$\uparrow\downarrow + \downarrow\uparrow$	
	$\uparrow$	$\downarrow\downarrow$	

Table 2.1: Spin transitions for Fermi and Gamow-Teller interactions

the neutron and proton renormalizes the axial vector current to  $g_A \neq -1$ , whereas  $g_V$  is conserved (conserved vector coupling (CVC) hypothesis). The ratio of the coupling constants,  $\frac{g_A}{g_V} = \lambda$ , is a defining parameter of the decay as is the lifetime  $\tau$ .

The neutron decay has three free parameters: The Cabibbo-Kobayashi-Maskawa-matrix element  $V_{ud}$ , the ratio of the weak coupling constants  $\lambda$  and the phase  $\phi$  (CP-violation is indicated by  $\phi \neq 0, \pi$ ).

The sum over all different leptonic spin states makes it possible to express the weak neutron decay in terms of the observables momentum, energy and spin as shown in Eqn. (2.2).

$$\begin{aligned}
 W dE_e d\Omega_e d\Omega_\nu \sim p_e E_e (E_0 - E_e)^2 dE_e d\Omega_e d\Omega_n u \\
 \times \left( 1 + a \frac{\vec{p}_e \vec{p}_\nu}{E_e E_\nu} + b \frac{m_e}{E_e} + \langle \vec{s}_n \rangle \cdot \left( A \frac{\vec{p}_e}{E_e} + B \frac{\vec{p}_\nu}{E_\nu} + D \frac{\vec{p}_e \times \vec{p}_\nu}{E_e E_\nu} \right) \right) + \dots
 \end{aligned}
 \tag{2.2}$$

where  $p_e, p_\nu$  are the momenta of the electron and the anti-electron neutrino respectively,  $E_e, E_\nu$  their energies and  $\vec{s}_n$  the neutron spin. In the Standard Model, correlation coefficients can be expressed as a function of  $\lambda$  and  $\phi$ , see e.g. [3, 4];  $\lambda$  is clearly overdetermined by measuring several correlation coefficients. However, in theories beyond the Standard Model, additional coupling constants arise and the correlation coefficients become independent[4].

## 2.2 Polarized Asymmetry Measurements

Historically, the first experimental evidence of a violation of a discrete symmetry, the P-violation, has been given by Wu et al. [5] and was predicted only shortly before by Lee and Yang [6]. The Wu experiment measured the angular distribution of the electron emitted in the nuclear  $\beta$  decay of  $^{60}\text{Co}$ . The Co nuclei were polarized by insertion into a paramagnetic structure (CeMg-Nitrate) that was cooled down. A magnetic field applied would po-

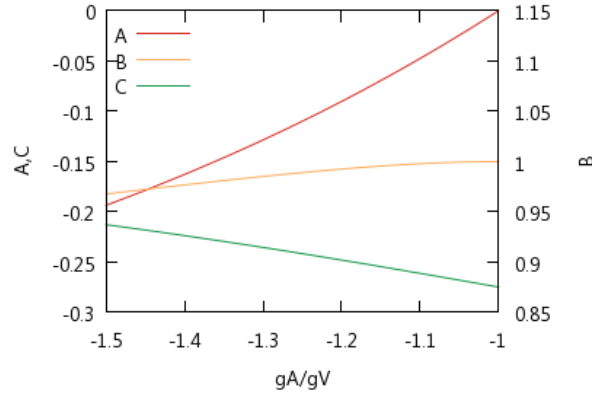


Figure 2.2: The correlation coefficients  $A$ ,  $B$  and  $C$  as a function of the coupling constant ration  $\lambda = g_A/g_V$  around the current value of  $\lambda = 1.2701 \pm 0.0025$

larize the Co nuclei and the angular distribution of the electron with respect to the Co polarization  $\langle \vec{J} \cdot \vec{p} \rangle$  could be measured (from 0 to 180 degrees). The polarization could then be easily flipped by inverting the magnetizing field. For conserved parity, the angular distributions are identical. However, parity was observed to be violated [5].

For the neutron decay, the observables  $A$ ,  $B$  and  $D$  are linked to asymmetry measurements. An additional accessible parameter is the proton asymmetry  $C = x_c(A + B)$ , a linear combination of  $A$  and  $B$ , see e.g. [3].  $D$  measures the T-violation. The parameters have different sensitivities to  $\lambda$ . Fig. 2.2 shows the parameters  $A$ ,  $B$  and  $C$  in proximity of the current value of  $\lambda$ . Clearly, their value varies differently for a given change of  $\lambda$ . While parity and combined parity-charge violations are within the Standard Model, their values cannot describe the state of the world. Deviations between  $A, B, C$  and the predictions made by the Standard Model (Tab. 2.2) may indicate new physics. The most optimistic theoretical estimates claim that at the low energy frontier, the correlation coefficients must be known with a precision of  $10^{-4}$  in order to make a qualitative distinction between Standard Model physics and different theories (e.g. [7]). Such a precision necessitates a neutron polarization also of  $10^{-4}$  as its error enters linearly in to the error on the coefficient, see Eqn. (2.2).

The polarization-related correlation coefficients  $A$ ,  $B$ ,  $C$ ,  $D$  have been measured in the past. Their current values can be found in Tab. 2.2. First

coefficient	expression	exp. value	exp. error
$A$	$-2\frac{\lambda^2+\lambda+1\cos\phi}{1+3\lambda^2}$	-0.1176	0.0011
$B$	$2\frac{\lambda^2+\lambda+1\cos\phi}{1+3\lambda^2}$	0.9807	0.0030
$C$	$-x_c(A+B)$	-0.2377	0.0026
$D$	$-2\frac{\sin(\phi) \lambda }{1+3\lambda^2}$	-0.00012	0.0002

Table 2.2: Polarization-related correlation coefficients in the Standard Model prediction [4] and their current experimental averages as given by the Particle Data Group. [2]

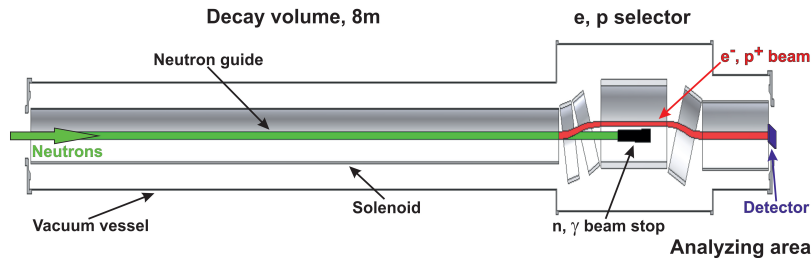


Figure 2.3: The decay-volume of PERC including the magnetic extraction of the charged decay products and detector area. Picture by M. Horvath, TU Wien.

measurements of correlation coefficients have been carried out in the late 1960s. Those results are not competitive anymore in terms of accuracy. The modern-day measurements started in the 90s and are continuing on with new experiments planned and funded in Europe, Japan and America. While historically cold neutrons were used to perform correlation coefficient measurements, recently, an ultra-cold neutron (UCN) experiment could deliver competitive results [8, 9, 10]. UCNs, despite very low statistics, have different systematics than cold neutrons. Experiments planned are PERC (see following section for details), ABba and PANDA [11, 12, 13] as well as UCNA [14] and UCNB, [15]. Furthermore, already existing experiments, PERKEO III [16] and aSPECT [17] plan measurements of polarized neutron decay, in particular  $C$ .

## 2.3 The PERC instrument

The Proton Electron Radiation Channel (PERC) is the next generation of instruments studying neutron beta decay correlation coefficients. It allows

access to parameters  $a$ ,  $A$ ,  $C$  and possibly  $R$  and  $b$ . PERC is built in the tradition of former PERKEO generations [18, 19, 16, 20, 21, 22] but with the goal of a new accuracy of  $10^{-4}$  [23]. It is designed to deliver a high flux of decay particles ( $10^6$  decays per second per meter, collected over a decay volume of 8 meters) providing high statistics. PERC is going to be built on the Garching Campus of the Technical University of Munich at the FRM II reactor. A high flux neutron beam of cold neutrons is guided from the reactor via a primary guide to the East Hall where PERC is going to be installed. The active decay volume, depicted in Fig. 2.3, is constructed from neutron guide segments of 2 meter length each. A longitudinal magnetic field of 1.5 T ( $B_0$ ) collects the charged decay products over the whole volume. The magnetic field has a slight gradient of the order of  $10^{-2}$  to avoid magnetic trapping of the charged decay particles. At the end of the decay volume, a magnetic chicane is installed. It serves two purposes: 1.) it increases the magnetic field up to 6 T ( $B_1$ ) and decreases afterward to 0.5 T ( $B_2$ ). By adjusting the ratio between the different magnetic fields ( $B_1$  can vary between 3 and 6 T), the maximum angle allowed between the collected particle and the  $B_0$ -field can be selected. This phase space selection minimizes systematics. 2.) The chicane is bent, so that the particles are transported around the neutron beam stop and can be detected behind it. Currently, different detector types are being discussed: An  $\vec{R} \times \vec{B}$ -spectrometer would allow to measure momentum of both the proton and the electron [24]. Plastic scintillators are being tested to measure the electron energy spectrum and a proton detection system [25] based on the potential barrier principle that is used in the aSPECT experiment [17].

In order to obtain statistics sufficient for  $10^{-4}$  accuracy, PERC needs to measure 2 days in continuous or 50 days in chopped mode. This includes a polarizer system with 10 % transmission. Systematic errors arise from different sources and are given in Tab. 2.3.

The correction on the polarization in the table is based on the results from Kreuz et al. [26]. Current values for neutron polarization have lower errors and corrections as shown in this thesis. For the measurement of polarization-sensitive parameters with PERC, it is important that PERC itself as a neutron guide does not alter the polarization of the neutron beam when neutrons are reflected. The common NiTi supermirrors are not suited for this task and the development of a non-depolarizing neutron guide is ongoing. Candidates

Source of error	comment	size of correction	size of error
non-uniform n-beam	for $\Delta\Phi/\Phi = 10\%$ over 1 cm width	$2.5 \times 10^{-4}$	$5 \times 10^{-5}$
other edge effects on e/p-window	for max. gyr. radius = worst case	$4 \times 10^{-4}$	$10 \times 10^{-4}$
magn. mirror effect, continuous n-beam		$1.4 \times 10^{-2}$	$2 \times 10^{-4}$
magn. mirror effect, pulsed n-beam	for $\Delta B/B = 10\%$ over 8 m length	$5 \times 10^{-5}$	$< 10^{-5}$
non-adiabatic e/p-transport		$5 \times 10^{-5}$	$5 \times 10^{-5}$
background from n-guide	seperately measurable	$2 \times 10^{-3}$	$1 \times 10^{-4}$
background from n-beam stop	separately measurable	$2 \times 10^{-4}$	$1 \times 10^{-5}$
backscattering off e/p-window		$1 \times 10^{-3}$	$1 \times 10^{-4}$
backscattering off e/p-beam dump		$5 \times 10^{-5}$	$1 \times 10^{-5}$
backscatt. off plastic scintillator	worst case	$2 \times 10^{-3}$	$4 \times 10^{-4}$
same with active e/p-beam dump	worst case	-	$1 \times 10^{-4}$
neutron polarization	status 2008	$3 \times 10^{-3}$	$1 \times 10^{-3}$

Table 2.3: Summary of errors and corrections relevant to PERC, detailed explanation given in [23].

are CuTi and Ni(Mo)Ti guides. First tests revealed promising [27].



# 3

## Polarization Methods

Nowadays, polarized neutrons know a vast variety of applications in experimental techniques. In function of the experiment's requirements including geometric and energetic restrictions, different methods are used to obtain a polarized beam. The first part of this chapter is dedicated to describe general properties and principles applied for neutron polarization, while the second part focuses on current neutron polarization methods. The methods described are focusing on cold neutrons, in particular methods that are applicable for large, cold neutron beams as used in neutron beta decay experiments. Parts of this chapter base on the comprehensive overview by Williams [28].

The neutron is a fermion with spin  $s = \frac{1}{2}$ . The neutron's spin has first been predicted in 1936 [29] and was experimentally confirmed in 1949 [30, 31]. The spin couples via the magnetic moment  $\vec{\mu} = \frac{2g}{m_n} \vec{s}$  to a magnetic field  $\vec{B}$  as a potential energy  $V_{\text{mag}}$  term in the Hamiltonian:

$$V_{\text{mag}} = \vec{\mu} \cdot \vec{B}. \quad (3.1)$$

A spin precesses in a magnetic field around the field axis. The average change in spin per time for a neutron with a kinetic energy much higher

than the coupling to the magnetic field can be expressed as

$$\frac{d\vec{\mu}_n}{dt} = \vec{\mu}_n \times \vec{B}. \quad (3.2)$$

In a quantization field, two spin orientations are possible along the field lines for the neutron: up ( $\frac{1}{2}$ ) and down ( $-\frac{1}{2}$ ). A *polarized* neutron beam contains neutrons of predominantly one spin direction.

### 3.1 Polarization Analysis

When talking about polarization of a neutron beam, we are not interested in the individual neutron spin, but in the average spin orientation of the beam. A neutron beam can be represented by a two-dimensional vector

$$\vec{J} = \begin{pmatrix} N_{\uparrow} \\ N_{\downarrow} \end{pmatrix} \quad (3.3)$$

where the first entry  $N_{\uparrow}$  corresponds to the number of up-spin neutrons and the second entry  $N_{\downarrow}$  to the number of down-spin neutrons. The total neutron flux is the sum of the two entries,  $N_{\uparrow} + N_{\downarrow}$ , and in an unpolarized beam  $N_{\uparrow} = N_{\downarrow}$ .

The neutron polarization  $P$  is defined in terms of the polarization degree: the relative difference of  $N_{\uparrow}$  and  $N_{\downarrow}$

$$P = \frac{N_{\uparrow} - N_{\downarrow}}{N_{\downarrow} + N_{\uparrow}}. \quad (3.4)$$

Similarly, the transmission  $T$  of a neutron beam through an entity is the total sum of up ( $N_{\uparrow}$ ) and down ( $N_{\downarrow}$ ) components getting through relative to the initial amount  $N'_{\uparrow} + N'_{\downarrow}$ :

$$T = \frac{N_{\downarrow} + N_{\uparrow}}{N'_{\downarrow} + N'_{\uparrow}}. \quad (3.5)$$

Polarizing components in a neutron beam aim to maximize the polarization degree of the beam with minimum flux loss. For the perfect polarizer, the transmission of an initially unpolarized beam is 50%, as in this case one and only one spin direction gets completely transmitted.

A high polarizing power is desirable when performing high accuracy measurements, as the analysis can be done more precisely: The polarization (Eqn. 3.4) of the neutron indicates the averaged ratio between up- and down-spin neutrons,  $f = \frac{N_{\uparrow}}{N_{\downarrow}}$ . This equation can be rewritten in the form of this ratio as:

$$P = \frac{f - 1}{f + 1} \quad (3.6)$$

When one desires to know  $P$  with a high precision, it is advantageous to seek out a high polarization of the neutron beam: The polarization is sensitive to  $f$  in the following way

$$\frac{dP}{df} = \frac{2}{(f + 1)^2}. \quad (3.7)$$

This sensitivity  $\partial_f P \rightarrow 0$  for  $f \rightarrow \infty$ . This corresponds to  $P \rightarrow 1$ . This means, it is easier to accurately measure polarization at high degrees of polarization in terms of statistics and systematics.

When modeling the evolution of the spin throughout a beam-line, the different elements in the beam-line can be represented as ( $2 \times 2$ ) matrices  $\mathbf{M}$  acting on the different spin components, including absorption or spin-flipping. The matrix elements can be chosen to be sensitive to parameters such as wavelength or time. The calculation is carried out from the initial beam as a vector on the right, the subsequent beam-line element in the matrix form from right to left and finished off by the detector component, a row vector  $\vec{D} = (1, 1)$  that allows to collapse the beam to a single count rate  $N_i$ :

$$N_i = \vec{D} \mathbf{M} \vec{J}. \quad (3.8)$$

Standard detectors themselves are not spin-sensitive, therefore the measured count rate  $N_i$  is always a mix of both spin directions. The count rate  $N_i$  has to be corrected for a certain dead time in the acquisition electronics. The actual count rate  $N'_i$  of a duration  $T$  versus the measured one  $N_i$  for a detector with dead time  $\tau$  is [32, p.123 ]

$$N'_i = \frac{N_i}{1 - N_i \frac{\tau}{T}}. \quad (3.9)$$

A polarizer  $P$  can be represented by:

$$\mathbf{P} = \begin{pmatrix} P_1 & 0 \\ 0 & P_2 \end{pmatrix}. \quad (3.10)$$

In order for the polarizer to polarize the beam,  $P_1 \gg P_2$  (or  $P_1 \ll P_2$  if the other component is preferred). In any case,  $P_1, P_2 \leq 1$ . In an ideal polarizer, only one spin orientation gets transported through the polarizer, thus  $P_2 = 0$  ( $P_1 = 0$ ). If the performance of a polarizing device is to be measured, a second polarizing device is required: the device polarizes the beam with its polarizing power  $P$  and the second one is used as a so called "analyzer" with an analyzing power  $A$ .

$$\mathbf{A} = \begin{pmatrix} A_1 & 0 \\ 0 & A_2 \end{pmatrix}. \quad (3.11)$$

For a perfect analyzer,  $\mathbf{A}_\uparrow$ :  $A_1 = 1, A_2 = 0$ , or for the opposite orientation  $\mathbf{A}_\downarrow$   $A_1 = 0, A_2 = 1$ . The analyzer determines the exact amount of  $N_\uparrow$  and  $N_\downarrow$  let through by the polarizer. Four count rates can be measured where the devices either let through the same spin component ( $N_w$ , "white" configuration) or opposite components ( $N_b$ , "black" configuration). Eqn. (3.14) shows how the polarizing power  $P$  for the  $N_\uparrow$  component can be determined by a perfect analyzer:

$$N_w = \vec{D} \mathbf{A}_\uparrow \mathbf{P} \vec{J} \quad (3.12)$$

$$N_b = \vec{D} \mathbf{A}_\downarrow \mathbf{P} \vec{J} \quad (3.13)$$

$$P = \frac{N_w - N_b}{N_w + N_b} \quad (3.14)$$

In reality, Eqn. (3.14) accesses the combined product of polarizing and analyzing power,  $AP$ , as both imperfect devices influence the count rates  $N_b, N_w$ . This is particularly true if  $A$  and  $P$  are similar. The statistical error of such a measurement of the combined analyzing and polarizing power  $\sigma_{AP}$ , provided that the number of counts are high enough to allow for the error on the count rate itself to be simply its square-root,  $\sigma_{N_i} = \sqrt{N_i}$ , Eqn. (3.4)

and error propagation lead to:

$$\sigma_{AP} = \sqrt{\sum_{i \in \{w,b\}} (\partial_{N_i} AP(N_i) \cdot \sigma_{N_i})^2} = \frac{2\sqrt{N_w^2 N_b + N_w N_b^2}}{(N_w + N_b)^2} \quad (3.15)$$

The fact that the analyzer in Eqn. (3.14) is optimized once for the  $\uparrow$  and once for the  $\downarrow$  necessitates to either invert the analyzer or flip the spin between the two devices via a spin flipper, see Sec. 4.3.2. Of course, neither polarizer nor analyzer or spin flipping devices are perfect, and measurements are affected by this. However, using the correct configurations, flaws of certain devices can cancel out, allowing for a correct characterization of another component. A detailed example on procedures is given in [33].

## 3.2 Spin Manipulation

Spin flipping can be achieved either by changing the spin orientation by 180 degrees or by inverting the experimental set-up by 180 degrees. Usually, it is simpler and experimentally cleaner to flip the spin orientation of the neutron than to physically turn a set-up.

An ideal spin flipper  $\mathbf{F}$  can be described as a completely off-diagonal matrix

$$\mathbf{F} = \begin{pmatrix} 0 & 1 \\ 1 & 0 \end{pmatrix}. \quad (3.16)$$

A real spin-flipper is imperfect, its flipping efficiency

$$f = 1 - 2\epsilon \quad (3.17)$$

is smaller than 1 by the inefficiency  $\epsilon$ . This is the most important characteristic number of a flipper:

$$\mathbf{F} = \begin{pmatrix} \epsilon & 1 - \epsilon \\ 1 - \epsilon & \epsilon \end{pmatrix}. \quad (3.18)$$

A spin flip is successful if the process of Eqn.(3.2) is either completely adiabatic or non-adiabatic. For the latter, the spin orientation in the lab frame remains while the B-field is inverted. This can be achieved by current sheets which abruptly disrupt previous B-fields. In case of an adiabatic flip, a popular method is the fast adiabatic passage flipping via radio frequency.

A static B-field that remains the main quantization field is applied: the holding field. Additionally, a radio frequent B-field is applied perpendicular to the holding field. The neutron precesses around the resulting (effective) field. The magnitude of the holding field changes slowly (adiabatically). If the Larmor frequency of the holding field is equal to the rotation frequency of the radio-field, the spin flip occurs. Throughout the procedure, the change of the effective field is held to be adiabatic. [28, p. 127-128], [34]

### 3.3 Polarizing Methods

#### 3.3.1 Stern-Gerlach Effect

A particle with a magnetic moment entering a B-field shifts in energy depending on the moment orientation due to the sign of the coupling (Eqn. 3.1). This can be used to manipulate a neutron's spin as the moment and the spin are parallel. A gradient in the quantization field implies thus a force (Eqn. 3.19) acting on the particle with opposite orientation for opposite moments (spins), eventually leading to a spatial separation. This effect is known as the Stern-Gerlach effect [35]:

$$F_m = \nabla(\vec{\mu} \cdot \vec{B}). \quad (3.19)$$

This method does not require an interaction of the neutron with a material, hence it prevents any intensity loss due to absorption. Furthermore, it should lead to very high polarization degrees up to 100 % if the beams are completely spatially separated.

The Stern-Gerlach effect is commonly used in ultra-cold neutron experiments. However, this method is rarely applied to warmer neutrons and is limited to very small, low divergent beams. The complete spatial separation of the two beams is difficult to achieve (but can be improved using a drift-space behind the magnet). A further difficulty are the asymmetric divergences of the two beams. In terms of a polarization analyzer, the Stern-Gerlach effect can be used to give very precise indication of the polarization [28, p. 125-126]. Early experiments measuring spin-related correlation coefficients in the neutron decay have used the Stern-Gerlach effect as an analyzing tool [36, 37].

Polarizing neutrons with the Stern-Gerlach method reduces the intensity

only by a factor of 2, as there is no interaction with matter in the polarizing process. As pointed out before, polarizing a neutron beam implies an intensity loss of at least 50%, as the devices only transmit spin one direction. However, [38] proposed a method for UCNs to prevent intensity loss; it was successfully tested [39]. The method uses the fact that kinetic energy differs for the two spin directions in a magnetic field arrangement, hence, the time they would spend in it differs. The gist is to adjust the time difference such that the slower spin component performs an additional Larmor precession, lining it up with the fast direction at the exit. [40]

### 3.3.2 Polarizing Crystals

Polarizing crystals can be used for a variety of neutron energies. They have the unique feature that they do not only polarize but also monochromatize the beam. Based on the desired wavelength, different alloys are used. All the polarizing crystals have in common that their nuclear scattering length and their magnetic scattering length are of the same magnitude, the magnetic part having a sign-dependence in function of the spin component. The neutrons get reflected in the (periodic) crystal grid that gives rise to Bragg scattering (monochromatization). Because of the unique relation between magnetic and nuclear scattering length, only one spin direction gets reflected, resulting in the polarization of the beam. Compared to a crystal that only monochromatizes, the transmission of a polarizing crystal is 0.25. Polarizing crystals are made of various alloys such as  $\text{Cu}_2\text{MnAl}$ ,  $\text{Co}_{0.92}\text{Fe}_{0.08}$ ,  $\text{Fe}_3\text{Si}$ ,  $\text{HoFe}_2$ . They work well around  $1 \text{ \AA}$  but have cut-off wavelength up to  $6.5 \text{ \AA}$ . [28, p. 98-102]

### 3.3.3 Polarizing Mirrors and Supermirrors

Mirrors are the oldest and still most common method to polarize neutrons. They have the advantage of accepting a relatively high divergence and wavelength range with constant performance. Currently, all precision experiments measuring the polarized decay of cold neutrons have been using mirrors and supermirrors to polarize their beam. The mirrors are made out of ferromagnetic material (Fe, Co or an alloy thereof). If a neutron in the void encounters a medium, this quantum-mechanically translates to an abrupt change in potential energy  $V_{\text{pot}}$ . The averaged potential energy (macroscopic) from

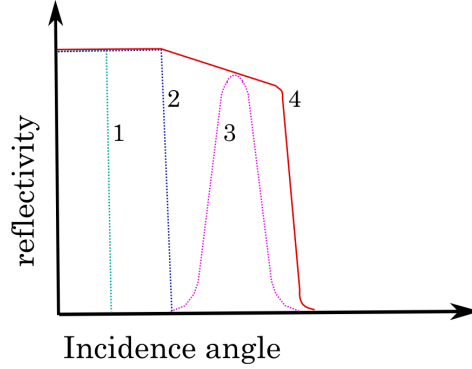


Figure 3.1: Idealized sketch of reflectivity in function of the incidence angle: (1) Reflectivity for spin-down component in mirror (2) Reflectivity for spin-up component in mirror (3) Example of constructive Bragg peak for up-component (4) Reflectivity for the up-component in a supermirror

a medium as seen by the neutron is called the *Neutron Optical Potential*  $V_{\text{opt}}$ . It is the same over the complete extent of the (homogeneous) medium given that it is an averaged quantity.  $V_{\text{opt}}$  depends on the averaged atomic number density in the medium  $N$  and the coherent scattering length  $b_c$ . It is therefore specific to each medium:

$$V_{\text{opt}} = \frac{2\pi\hbar^2}{m_n} N b_c. \quad (3.20)$$

A neutron entering a medium from the void changes in kinetic energy and direction as the boundary conditions require conserved energy and momentum. Hence, it is possible to define a refractive index, similarly to the case in classical optics. In addition, this makes it possible to have total reflection of the neutron on the void-medium interface up to a certain critical angle  $\theta_c$ . Up to  $\theta_c(V_{\text{opt}})$ , total reflection takes place. Above this critical angle, the reflectivity gets imaginary and the neutron is transmitted, see curve 1 in Fig. 3.1. This critical angle can be expressed as follows, assuming that  $\theta_c$  is small.

$$\theta_c \approx \lambda \sqrt{\frac{N b_c}{\pi}} \quad (3.21)$$

Note that  $\theta_c$  is intimately linked to the neutron's kinetic energy via the wavelength  $\lambda$ .

This is the principle of a neutron mirror. In the case of a ferromagnetic material, this mirror can be used to polarize neutrons: The ferromagnetic



material	$Nb_{\text{tot}} \uparrow [10^{14}\text{m}^{-2}]$	$Nb_{\text{tot}} \downarrow [10^{14}\text{m}^{-2}]$
Co	6.494	-1.946
Fe	13.16	3.018
Ti	-1.945	-1.945
Si	2.073	2.073

Table 3.1:  $Nb_c$  is tabulated for different materials for both possible spin orientations. [41]

material has an internal magnetic field, the potential energy differs for neutrons with spins  $\vec{s} \sim \vec{\mu}_n$  parallel and anti-parallel to this magnetic field due to the coupling (Eqn. 3.1). In order to polarize neutrons, a quantization field is already in place. However, it does differ in strength from the internal magnetic field of the mirror. The difference of field strength leads to the magnetic scattering of the neutron at the interface. The coupling of the neutron spin to the internal magnetic field can be translated to a magnetic scattering length  $b_m$ , such that the total scattering length  $b_{\text{tot}}$  for parallel (anti-parallel) spin orientations including the scattering from the optical potential (Eqn. 3.20) can be described as

$$b_{\text{tot}} = b_c \mp b_m \quad (3.22)$$

The critical angle (Eqn. 3.21) depends now on not only  $b_c$  but on  $b_{\text{tot}}$ . Hence, the angles for critical angles are different for the two possible spin states, this is represented by the curves 1 and 2 in Fig. 3.1. The different critical angles permit to polarize a beam, either in transmission or in reflection when the incidence angle is such that only one of the two spin directions gets reflected. The relevant parameter for the potential (Eqn. 3.20) of the most common materials in neutron polarization are given in Tab. 3.1. The two polarizing materials, Co and Fe, have different potentials and thus critical angles.

The difference in critical angles for the up and down spin direction can be enhanced employing the supermirror technique: With this technique, the Bragg scattering in analogy to polarizing crystals is combined with the polarizing mirror. It has first been introduced by Mezei [42, 43] and bases on thin-layer techniques developed for photon optics. Polarizing supermirrors are built of alternating layers of a ferromagnetic material (Fe, Co) and a non-ferromagnetic material (Si, Ti), sputtered on a carrier. Each spacing of the ferromagnetic material introduces a constructive Bragg interference

peak for the spacing thickness. By varying the thicknesses, the critical angle for the up-component can be artificially continuously enlarged. Classically speaking, this means that several constructive Bragg-peaks are constructed for different angles, leading to a quasi-continuous reflection up to the critical angle. The idealized approximation of the resulting reflection curve is a four-part function; a sketch is given by curve 4 in Fig. 3.1: The reflectivity is a constant for incidence angles inferior to the critical angle of the bulk of the ferromagnetic material. After that, it declines as a linear function with negative slope until a bit before the critical angle of the supermirror. The transition at the critical angle itself is modeled with a tangent hyperbolic and everything beyond this incidence angle is again a constant horizontal function at height 0. Supermirrors are characterized by their critical angle via the supermirror factor  $m$ : The reference critical angle is the one of <sup>58</sup>Ni,  $\theta_{\text{cNi}}$ , the supermirror factor  $m$  is now the ratio with respect to  $\theta_{\text{cNi}}$

$$m = \frac{\theta_{\text{c}}}{\theta_{\text{cNi}}}. \quad (3.23)$$

The layers have to become thinner the higher the aimed  $m$ -value is. The number of layers needed scales with the fourth power of the  $m$ -value. This is a challenge, especially in terms of surface roughness that causes off-specular scattering<sup>1</sup> and hence a disturbance of the transported phase-space. Roughness and diffusion between the layers that becomes acute for thin layers as the diffusion length is comparable to the layer thickness, can be partially prevented by adding air and/or N to the mix during the sputtering process, limiting grain sizes and creating diffusion barriers [44]. Layers are sputtered on the carrier starting with the thinnest layer. This prevents to much absorption at grazing incidence angle as these absorption-susceptible neutrons have to cross the least matter. Furthermore, the roughness of the thinnest layers is more easily controllable if deposited first. A reflection of the wrong spin direction by the carrier material (typically glass or Si) can be prevented by a deposit of an absorbing layer. [45]

In the case of polarizing supermirrors, the spin component that is transmitted should not reflect on any of the layers. Thus, the non-magnetic material is chosen so that its neutron optical potential is as close as possible

---

<sup>1</sup>incidence angle is not equal to reflected angle due to a non-flat surface, the scattering remains elastic

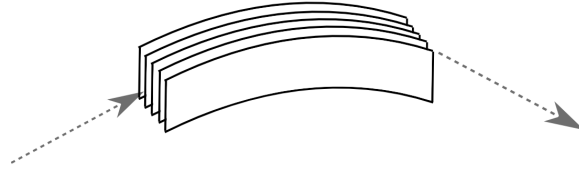


Figure 3.2: Example of a bender. The direct sight is prevented.

to the potential of the ferromagnetic material.

### Benders And The X-SM Geometry

Past neutron decay experiments with polarized neutrons exclusively relied on polarizing supermirrors to polarize a beam [46].

The challenge for polarizing with a reflective plane is to cover the whole beam for reflection. Naturally, this gets difficult for beams with a large cross section. Benders offer an elegant solution. The principle was first introduced by Soller [47] for simple coated guides and has since been applied to supermirrors as well. A comb of guide plates is introduced in the beam-line. The plates are bent (and therefore the actual beam direction is bent), enforcing a reflection of each neutron that will continue in the beam-line, as the exit of the bender is not in direct sight of the entry, see Fig. 3.2 [28, p. 118-126]. The curvature of the bender changes the direction and the divergence of the beam. Benders can cover large beam cross sections, in the order of  $3 \text{ cm} \times 5 \text{ cm}$  and have curvature radii in the order of 30 m.

The performance of polarizing mirrors can be enhanced by the crossed geometry of two supermirrors (X-SM geometry [26]). This method employs the complete phase space available for reflection: The neutrons are reflected on a first supermirror (possibly a bender) with polarizing power  $P_1$ . The spin then gets adiabatically turned by 90 degrees with respect to its initial orientation. A second reflection in this twisted state on a supermirror with polarizing power  $P_2$  completes the polarization process. The orthogonality of the two reflections makes the incidence angles independent. The total polarization obtained suppresses imperfections of the polarizing components quadratically under the assumption that those are small:

$$P_{tot} \approx 1 - \frac{1}{2}(1 - P_1)(1 - P_2). \quad (3.24)$$

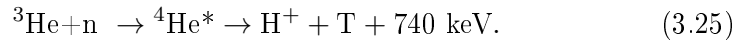
This set-up was first tested in 2005 and the maximal polarization reached was 99.7(1) %. It was used for some of the PERKEO II measurements ([20, 21, 22]). This is the highest polarization degree reached in a  $\beta$ -decay measurement. The measured polarization however was below the anticipated value of 0.9998. A depolarization of the beam by the mirrors was suspected and estimated to be at least several times  $10^{-3}$ . Changing the holding field in the bender housing changed the performance of the set-up indicating that the magnetization of the mirror might be responsible for this behavior [26].

### 3.3.4 Helium Spin Filter

In spin filters, as the name indicates, one spin orientation does get transmitted while the other one gets absorbed in the filter material, preferably completely. Sm was used as the first filter material. The challenge in these materials is to ensure that the "good" spin orientation does not get absorbed while the other one does so entirely. In practice, this mostly translates to perfectly polarize the filter material, which often is technically difficult. It is important however to note, that while the filter material polarization is linked to the resulting neutron polarization, the filter material polarization can often be much lower in order to get the desired neutron polarization [28, p. 105-107].

In the following, the helium spin filter is going to be described in detail, but much of it is also true for other spin filters of similar kind.

The  $^3\text{He}$  isotope captures neutrons, forming a metastable  $^4\text{He}$  excitation with the width  $\Gamma = 270$  keV before promptly decaying into tritium and a proton:



The neutron capture is sensitive to the orientation of the neutron spin relative to the  $^3\text{He}$  spin (parallel ( $\uparrow\uparrow$ ) or anti-parallel ( $\uparrow\downarrow$ )). The absorption of the anti-parallel orientation has an absorption cross section of  $\sigma_{\uparrow\downarrow} [\text{b}] \approx 6000 \cdot \lambda [\text{\AA}]$ , while  $\sigma_{\uparrow\uparrow} [\text{b}] \approx 5$ . This translates to a transmission  $T$  sensitive to the neutron spin orientation of a neutron crossing a  $^3\text{He}$  volume of length  $l$  and number density  $n_{\text{He}}$ , polarized to a degree of  $P_{\text{He}}$  and a (unpolarized) neutron capture cross section  $\sigma [\text{b}] \approx 3000 \cdot \lambda [\text{\AA}]$  [48, 49].

$$T_{\pm} = \exp(-\sigma(1 \mp P_{\text{He}})n_{\text{He}}) \quad (3.26)$$

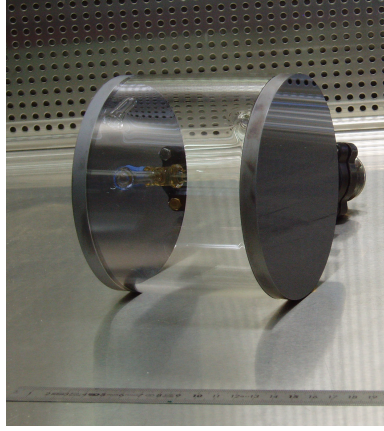


Figure 3.3: An empty He-cell, not yet covered with Cs. The windows are made of Si. Courtesy of D. Jullien, Neutron Optics Service at ILL.

Therefore, *polarized*  $^3\text{He}$  can be used to polarize a neutron beam by filtering out one spin direction. The entity of  $l \cdot n_{\text{He}} \cdot \sigma$  is referred to as the helium *opacity* and will be named  $Q$  in this text. It can be rewritten in terms of the easily accessible helium pressure  $p$  in bar, the path  $l$  in centimeters and the neutron wavelength  $\lambda$  ( $\sim$  energy) in Ångström via

$$Q = p \cdot l \cdot \lambda \cdot 0.0728 \frac{1}{\text{bar} \cdot \text{cm} \cdot \text{Å}}. \quad (3.27)$$

The total transmission (Eqn. 3.5) of the neutron beam through a volume of polarized helium can be written therefore as

$$T = e^{-Q} \cosh(Q \cdot P_{\text{He}}). \quad (3.28)$$

The resulting degree of polarization in the neutron beam can be written by Eqn. (3.4) as follows:

$$P = \tanh(Q \cdot P_{\text{He}}). \quad (3.29)$$

The polarization of the helium is obtained via optical pumping. Two methods are currently employed: The Metastable Exchange Optical Pumping (MEOP) polarizes the helium atoms via a scattering process with excited (metastable)  $^3\text{He}$  that is excited with a Rb laser of 1083 nm. In the other method, the Spin Exchange Optical Pumping (SEOP), the laser light of 795 nm polarizes rubidium atoms that pass-on the polarization to the helium atoms. SEOP can be used to polarize helium cells at the pressure of 1 bar

directly in the beam while MEOP necessitates a helium pressure at the mbar level and in addition, polarization is lost during the compression process [50]. Nowadays, SEOP [51] and MEOP both routinely reach cell polarizations of 76%.

In the experimental set-up, the helium atoms are kept oriented with a magnetic field. It is possible to flip the helium spin and thus effectively flipping the neutron spin exiting the helium volume by fast adiabatic flipping, making an external neutron spin flipper obsolete. To this goal, the ILL has developed so-called magic boxes: They are magnetic cavities made out of  $\mu$ -metal shielding exterior magnetic fields including the earth field. Inside the magic box, a holding field of about 1 mT keeps the helium spins oriented. The  $\mu$ -metal shielding homogenizes the magnetic field as it acts like a magnetic mirror [52, 49]. Coils fastened on the magic box' inner wall allow a fast, adiabatic spin flipping of the helium nuclei with radio-frequency, similar to the method described for the neutron flipper.

Polarized helium is mostly contained in quartz cells of varying volume and shape, see Fig. 3.3. For all the results presented in this work, cylindrical cells have been used of 1 liter of volume. Their entry and exit windows were made out of Si instead of glass to minimize beam broadening and depolarization by refraction and scattering.

The helium polarization decreases over time. The most prominent factor to this relaxation are the collisions of the helium atom with the cell wall. Other factors are inhomogeneities in the quantization field and magnetic dipole interaction at the collision of two atoms. Following the notation from [52], the development of polarization  $P_{\text{He}}$  over time  $t$  of a helium cell can be approximated by an exponential, with the initial polarization degree  $P_{\text{He}0}$

$$P_{\text{He}} = P_{\text{He}0} \cdot e^{-\frac{t}{T_1}} \quad (3.30)$$

where the cell's lifetime  $T_1$  is the sum of all the contributions to a possible depolarization.

$$\frac{1}{T_1} = \frac{1}{T_{\text{wall}}} + \frac{1}{T_{\text{field}}} + \frac{1}{T_{\text{dipol}}} + \dots \quad (3.31)$$

The dominant wall interaction can be decreased by sprinkling Cs on the glasses inner wall, while inhomogeneities in the B-Field simply have to be below  $5 \cdot 10^{-4}$  relative. Inter-atomic interactions cannot be controlled but also only become important at high pressure. [52]

Helium spin filters are not commonly used in neutron beta decay experiments. However, because of their easily tunable performance and high precision and high divergence acceptance, they were proposed by Zimmer [53, 54, 46]. The PERKEO II experiment used helium spin filters as polarization analyzers [21]. Neutron beta decay experiments are mostly carried out at high intensity beams. Sharma et al [55] have reported a decrease of performance for Rb-coated SEOP helium cells in high intensity beams.

# 4

## Polarizer Experiments

This chapter gives account of the experiments carried out during this thesis regarding polarization-related tools. The goal was to establish a precise measurement method for high polarizations and to develop tools that can produce such a high polarization. This requires to measure the analyzing and polarizing power as well as possible depolarization occurring in components. Two instruments were used: The Opaque Test Bench (OTB) and SuperADAM [56].

SuperADAM is a polarized neutron reflectometer. It provides a narrow, monochromatic, polarized beam with an incident flux of  $2 \cdot 10^5$  neutrons/s/cm<sup>2</sup>. The neutrons are polarized with a periodic multilayer that allows for polarized Bragg scattering and the incident polarization is about 98.6%. The 4.4 Å beam is very narrow both in terms of wavelength ( $\frac{\Delta\lambda}{\lambda} = 0.7\%$ ) and divergence (ca 0.2 mrad). The beam is analyzed with a fan-like supermirror analyzer that covers all scattering angles, see Fig. 4.1. Two spin flippers with efficiencies up to 99.9% allow to track all four possible intensities,  $I_{++}$ ,  $I_{+-}$ ,  $I_{-+}$ ,  $I_{--}$ . Neutrons can be detected over a wide area thanks to a position-sensitive detector [56].

The Opaque Test Bench can be used for high precision polarimetry. It is



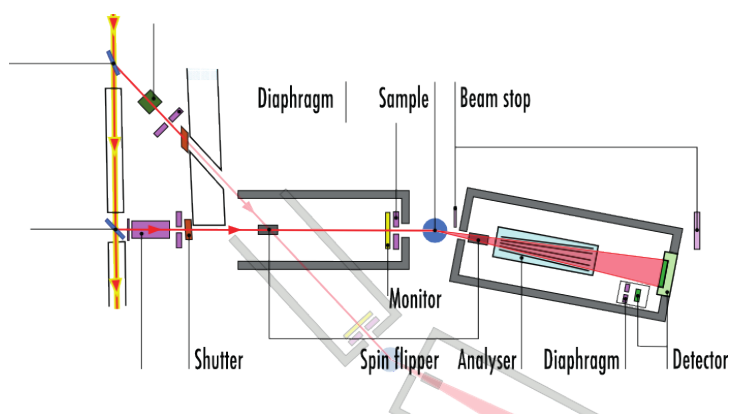


Figure 4.1: The SuperADAM instrument, current set-up options, the bold option was used for the data presented. [56] Picture courtesy of A. Devishvili, ILL

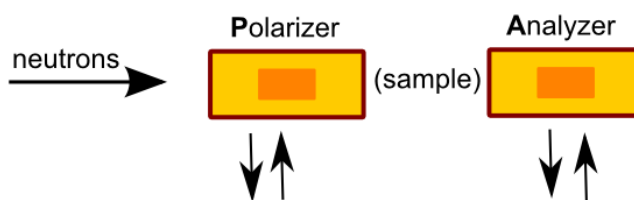


Figure 4.2: The Opaque Test Bench

built from two highly opaque helium cells, one acting as polarizer, the other as an analyzer of the beam, see Fig. 4.2. The helium spin in both cells can be flipped independently, so all possible intensities  $I_{++}$ ,  $I_{+-}$ ,  $I_{-+}$ ,  $I_{--}$  can be measured. Sec. 4.1 gives details of the set-up and validates this test bench as a source for very high, accurate polarization better than 99.99%. The OTB can be used to precisely measure depolarization by placing a sample between the analyzer and polarizer cell. By comparing the polarization of the beam with and without the sample present, the influence of the sample on the polarization can be determined. In order to test supermirrors, the OTB geometry was altered to a reflectometer set-up, details in Sec. 4.2.2. The chapter is organized as follows: in Sec. 4.1, the OTB is characterized. The depolarization in polarizing supermirrors is looked at in Sec. 4.2 in detail using data from both the OTB and SuperADAM. In Sec. 4.3.1 and 4.3.2 the depolarization from beamline components is reported. Sec. 4.4 reports the

polarizing powers for a single reflection from supermirror samples. Finally, Sec. 4.5 reports results from a crossed (X-SM) geometry measurement with improvements deduced from the earlier sections.

## 4.1 The Opaque Test Bench

In this section, the description of a polarization analysis with an accuracy of better than  $10^{-4}$  is given. The core system consists of two identical helium cells placed in magic boxes (MB) [52], one polarizing, the other analyzing the neutron beam. As pointed out in Sec. 3.3.4, helium cells provide very high polarization power for high opacity and helium polarization.

### 4.1.1 Set-up And Data Acquisition

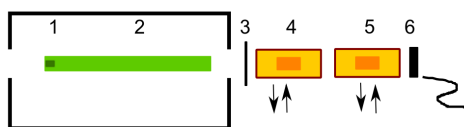


Figure 4.3: The Opaque Test Bench: schematic set-up for validation. (1) Beryllium filter (2) Neutron guide (3) Chopper (4) Polarizing helium cell in magic box (MB1) (5) Analyzing helium cell in magic box (MB2) (6) Detector.

The experiment took place at the high intensity cold beam position PF1B at the ILL [57]; a schematics of the set-up is depicted in Fig. 4.3. A neutron guide leads from the H113 exit through the casemate. At its end, just inside the PF1 experimental zone, a chopper running with about 2000 rpm was installed for wavelength resolution of the cold, white neutron beam. Two helium cells, each in an MB, were placed one after the other. The identical cylindrical Cs coated cells were 15 cm long and had a diameter of 14 cm. They were made out of glass with Si entry and exit windows. They were prepared off-site at the helium laboratory of the Service d'Optique des Neutrons at ILL with the MEOP method to about 75% helium polarization and exchanged every day. The distance between the magic boxes was about 30 centimeters. The guiding field was given by the guiding field of the magic boxes.

The cells were adjusted for different wavelength by using different opacities, which was achieved by filling them with different pressures: 1 bar, 1.4 bar

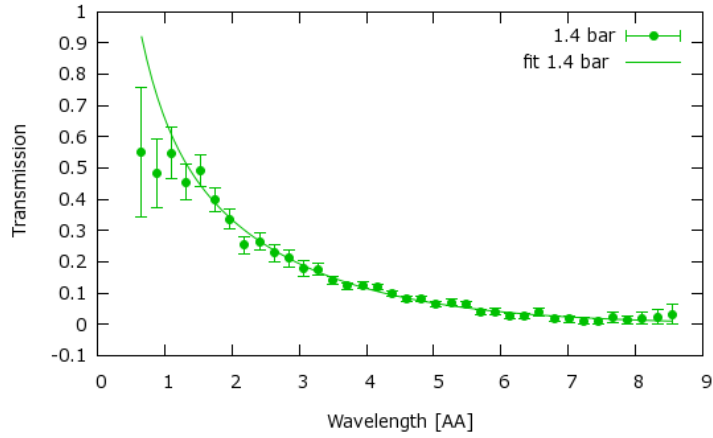


Figure 4.4: Wavelength-resolved transmission at 1.4 bar for the white component

and 1.7 bar. Each measurement used two cells with identical pressure. The time-resolved detection of the neutrons was performed by a helium detector with a 10% efficiency.

A 40 mm thick Be filter was placed inside of MB1 in front of the helium cell. It was used to scatter off wavelengths shorter than  $4\text{\AA}$ . The parameters of the set-up were not optimized for these short wavelengths that would only have contributed to background. The influence of the filter is shown in Fig. 4.5 (a). While it effectively suppresses the short wavelengths by about a factor of 15, the loss of the desired longer wavelengths is minor. The transmission of the decreases exponentially (see Eqn. 3.28) with wavelength as shown in Fig. 4.4.

The chopper was placed inside a lead castle, a boron tunnel led out. In general, great care for a good protection from outside background was given via boronated rubber and  $B_4C$  bricks. The detector was protected from neutrons through borated polyethylene and from gammas by a lead castle. As boron rubber has ferromagnetic impurities, it is not suited for beam collimation of a polarized beam. Therefore, inside the magic boxes, the collimation was achieved via Gd-painted cardboard boxes. The ambient background was measured with the chopper turned off or with a turned-off beam. The influence from the ambient background with no beam was found to be negligible. However, the running chopper, cutting off most of the

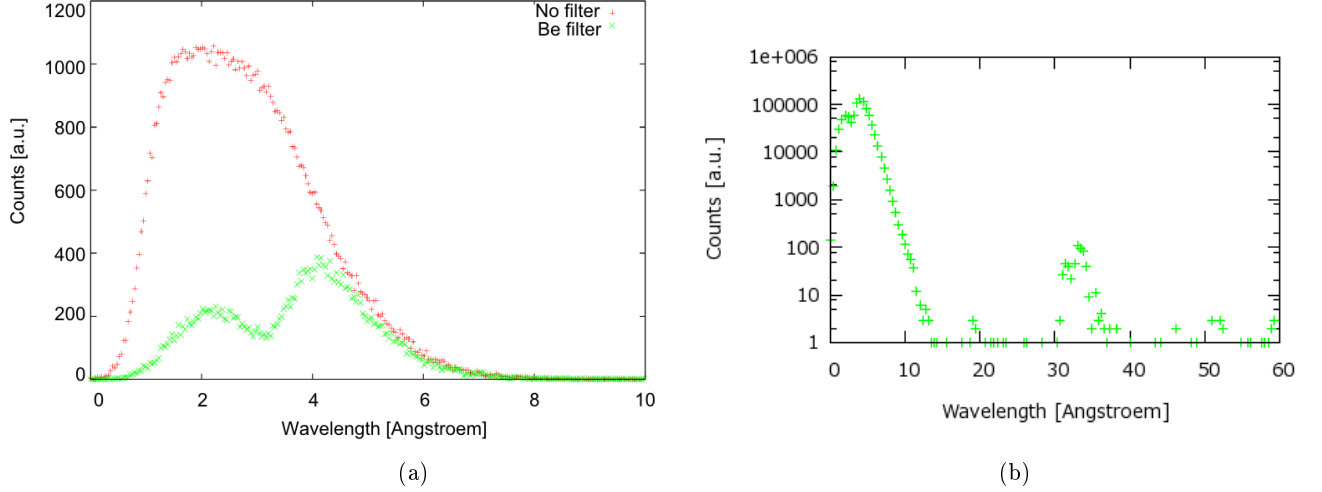


Figure 4.5: Spectrum at the end of the OTB with a 1.4 bar cell batch in "white" configuration (a) with and without a Be filter (b) Logarithmic display of the complete spectrum with the Be crystal. The intensity peak at 30 Å results from leakage through a second, imperfectly closed slit.

beam, is an influence on the background. Fig. 4.5 (b) shows the spectrum detected after the analyzing MB. For the data analysis, the background was taken from the time-of-flight measurement, using count rates in the range from 44 to 58 Å.

As explained in Sec.3.1, the cells' helium polarization can either be parallel or anti-parallel, their configuration can thus either be white or black. For cells with a reasonable opacity, the count rate in the black configuration is low. Therefore, the measurement time in this configuration was longer than in the white configuration by a factor of 20 in order to gain sufficient statistics. The measurement protocol was established such that drift effects were corrected for and is shown in Tab. 4.1. For both the black ( $N_b$ ) and the white ( $N_w$ ) count rate, only the sum of the respective counts over a complete measurement cycle was tracked.

#### 4.1.2 Data Analysis And Error Treatment

It is crucial to the experiment that the cells do not significantly depolarize over the course of one measurement. The polarization decreases exponen-

configuration	time [s]
black	400
white	20
white	20
black	400
white	20
black	400
black	400
white	20

Table 4.1: Measurement protocol for the OTB.

tially with time, Eqn. (3.30, 3.31). For the measurement in Tab. 4.1 lasting  $1680 \text{ s} \approx 0.5 \text{ h}$ , the neutron polarization loss would be  $6 \cdot 10^{-7}$  for a  $5 \text{ \AA}$  beam at 1.4 bar in a cell with  $T_1=200 \text{ h}$  over the course of the measurement. A critical point of the measurement is that the polarization loss in the helium is negligible when the cell polarization gets flipped. By flipping the cell excessively and measuring the transmission afterwards, a depolarization of  $1.5 \cdot 10^{-5}$  per flip for the analyzer and  $4 \cdot 10^{-6}$  per flip for the polarizer magic box was determined for the cell "D22/02". A helium polarization loss of about  $1.5 \cdot 10^{-5}$  translates to a neutron polarization loss of ca  $3.5 \cdot 10^{-6}$  for a freshly polarized cell.

Initial measurements showed a quick depolarization of the helium after only a few flips of its polarization. This was tracked back to a complete, conducting Cs-ring in the cell that had accidentally formed when preparing the cell and was suspected to perturb the magnetic field. Indeed, the use of other cells without such a ring was satisfactory, leading to flipping efficiencies given above. As from the 4 available cells, 2 were affected by such a ring and the cells had to be exchanged every 24 hours, one cell in each batch could be flipped. Hence, only the combined analyzing and polarizing product  $AP$ , Eqn. (3.14) could be determined.

The minimum measurement time for a complete cycle is about 0.5 h, see Tab. 4.1. However, statistics acquired over this period of time is still low. In Fig. 4.6 (a), the  $AP$  of different measurement durations for a batch of cells is shown. While the statistical error would get lower with time, the helium depolarizes and thus the cells' performance decreases. This can be seen, as the  $AP$  gets more stable up to 3h i.e. 6 measurement cycles, while the  $AP$  at

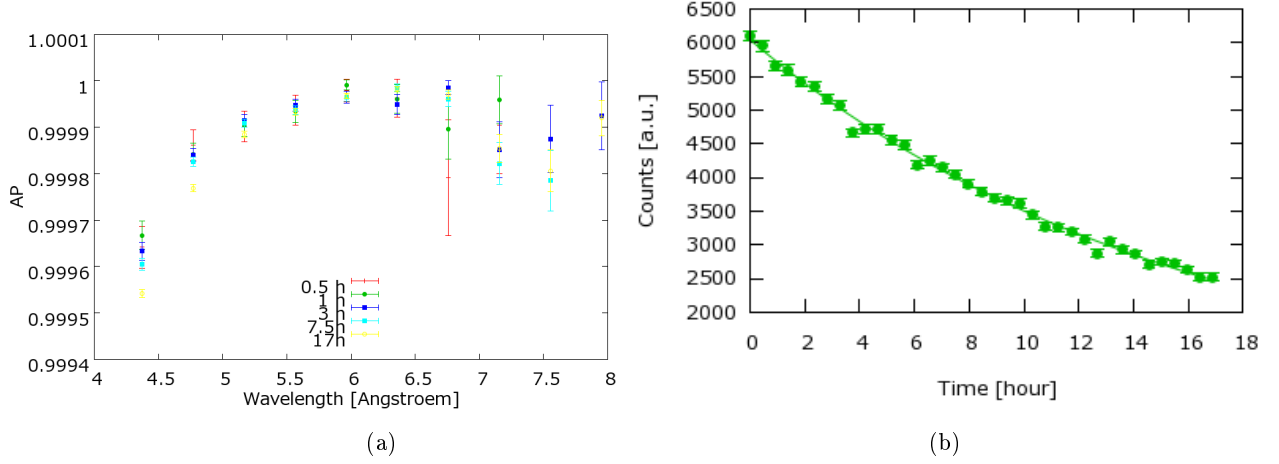


Figure 4.6: (a) Wavelength-resolved  $AP$  measured for different amounts of time.(b) Counts of the white component for a night's measurement with a single exponential fit to the data, modeling He polarization loss

7.5 h and 17 h is significantly lower, as the helium polarization losses becomes important. In general, data from at least 1.5, most of the time 3 h is used in analysis as it enables satisfying statistics with minimum helium polarization change. The depolarization of the helium is shown over the course of time in the form of the count rate of the white (high count rate) component over a night's measurement. The count rate drops due to the lower transmission of the cells with lower helium polarization, Eqn. (3.30, 3.28). The cells polarizer and analyzer have lifetimes with  $T_1^p = 1014$  h,  $T_1^a = 240$  h measured in the optimum environment of the Tyrex filling station of the Service d'Optique des Neutrons. In the experimental environment, in the magic boxes, cells tend to have lower lifetimes [58]. The two cells in the OTB set-up have been approximated by one single, averaged lifetime  $T_1$ . The fit reveals  $T_1 = 110(1)$  h. Cell lifetimes tend to be shorter in the magic boxes as their magnetic field is less homogeneous than in the filling station.

The data acquisition electronics has a dead time (see Eqn. 3.9) of about  $2\mu\text{s}$  per count. It affects wavelengths with high count rates more than longer wavelengths, see Fig. 4.7(a). Beyond  $4 \text{ \AA}$ , the influence is lower than  $10^{-5}$  on the  $AP$  product. Therefore, dead time corrections are not a significant contribution.

The influence of the background correction is bigger. Fig. 4.7 (b) shows the

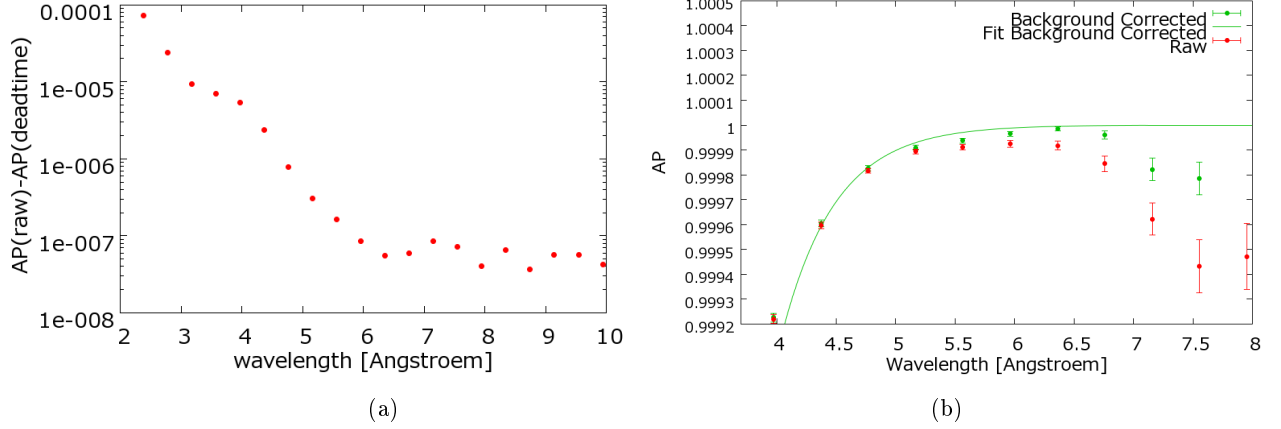


Figure 4.7: Influence of systematic errors for a 1.4 bar cell batch (a) Difference in  $AP$  for raw and dead time corrected data. (b)  $AP$  for raw and background corrected data including a fit to the background corrected data

resulting  $AP$  and compares it to raw data. While for the short wavelengths, the correction does not have an influence, the  $AP$  is raised through background correction for longer wavelengths. At those wavelengths, the signal-to-background ratio is lower due to the lower transmission and thus the background subtraction has a bigger effect on the result. For wavelengths of  $7 \text{ \AA}$  and longer, the background model described in Sec. 4.1.1 is not sufficient. These wavelengths are not in the prime area of interest for this thesis.

The fit function used to fit the polarization data is based on Eqn.(3.29). The measurement is a TOF measurement, the wavelength being determined by the time the detected neutron needs to get from the chopper to the detector. The transmission and the polarization of a neutron beam are very sensitive to the wavelength, see Eqn (3.28,3.29). While the distance between the detector and the chopper is easily determined and constant, the exact determination of the time is influenced by the chopper resolution. The opening function of a chopper with identical slit and beam size is a triangle (convolution of the two rectangular functions made by the rotating and the fix disk). In the analysis, the resolution is approximated by a Gauss function

$$R(\lambda) = \frac{1}{\sqrt{2\pi}\sigma} e^{-\frac{\lambda^2}{2\sigma^2}} \quad (4.1)$$

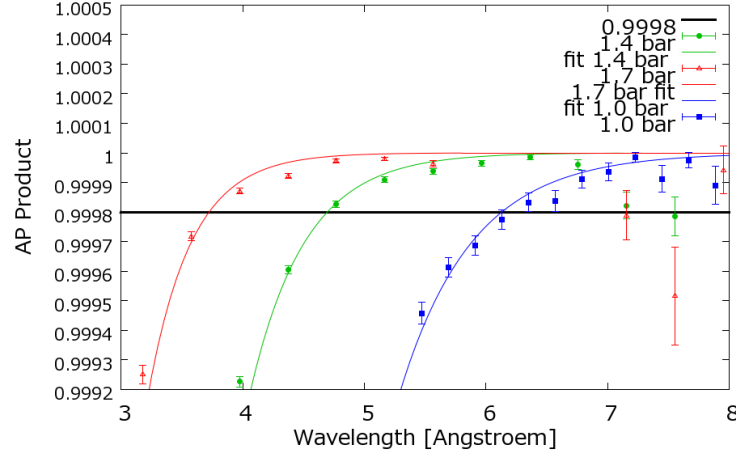


Figure 4.8:  $AP$  measured at 1.0, 1.4 and 1.7 bar with statistical errors and corresponding fits

with the full width at half maximum  $2\sigma\sqrt{2\ln 2}$ . Divergence has not been taken into account. The appropriate fit-function  $P_{\text{fit}}$  is therefore the convolution of the polarization with the resolution induced by the chopper:

$$P_{\text{fit}}(\lambda) = \int_{-\infty}^{\infty} P(\lambda')R(\lambda - \lambda')d\lambda' = \tanh(aP_{\text{He}}(\lambda - a\sigma^2)) \quad (4.2)$$

where  $a$  is the opacity from Eqn. (3.27) divided the wavelength:  $a = \frac{Q}{\lambda}$ . The fit is applied to a certain wavelength range. For shorter wavelengths, the intensity changes too quickly with the wavelength [57], such that the assumption of a Gaussian in Eqn. (4.1) cannot be applied. For wavelengths longer than 8 Å, the intensity is low [57] in addition to a reduced transmission, Eqn. (3.29). In this area, the statistics is too low for a sufficient fit, as the signal-to-background ratio is too low. The fit is applied to the square-root of the measured  $AP$ , as the cells are assumed to provide identical performances with the fit parameter being the helium polarization. Fig. 4.8 reports the  $AP$  measured for three different helium pressures 1.0, 1.4 and 1.7 Å. The fit range was adjusted for the different pressures, as the different resulting opacities have different sensitivities to the above discussed influences on the fit. The fit ranges were [5Å,9Å], [4Å,8Å] and [3.5Å,7.5Å] respectively. Tab. 4.2 gives a summary on the expected wavelength at which the  $AP$  of 0.9998, corresponding to a polarization of 0.9999 (for identical cells) is reached and compares it to the measured wavelength. The wavelengths at which the de-



#### 4.2. DEPOLARIZATION MEASUREMENTS IN POLARIZING MIRRORS 35

pressure	wavelength anticipated [ $\text{\AA}$ ]	measured wavelength [ $\text{\AA}$ ]	$AP$ measured	error
1.0	6.2	6.3	0.99983	$3 \cdot 10^{-5}$
1.4	4.5	4.8	0.99982	$1 \cdot 10^{-5}$
1.7	3.8	4.0	0.99987	$1 \cdot 10^{-5}$

Table 4.2:  $AP$  above 0.9998 for different cell pressures: expected wavelength and measured wavelength. The expected wavelength is corrected for resolution as in Eqn. (4.2)

sired polarization degree is reached are longer than anticipated.

In conclusion, the performance of the OTB is satisfactory having an analyzing power sufficient for  $10^{-4}$  accuracy at a wide wavelength range.

## 4.2 Depolarization Measurements In Polarizing Mirrors

While benders are designed such that each neutron at least encounters one reflection, multiple reflections are common, depending on the divergence. In advanced designs such as S-shaped benders or the X-SM geometry, multiple reflection is essential to the design. A first reflection on a polarizing surface hopefully leads to a polarized beam. A second reflection of a perfect device would simply again reflect the beam, as it is completely polarized. However, if there are depolarizing effects occurring, they are affecting the polarization of the beam in the second reflection. Generally, if there are depolarizing effects in multiple polarizing reflections, it is only the last reflection where the depolarization is important [26], as it determines the final polarization degree. Depolarization in previous reflections however do influence the transmission of the bender.

Depolarization of a polarized neutron beam by a medium is caused by a misalignment between the local magnetization and the neutron spin [59]. The component vertical to the spin induces Larmor rotation of the spin (Eqn. 3.2) that effectively decreases the overall polarization.

When studying the magnetization in supermirrors, there are two different factors that influence the performance: a) in-plane magnetization b) magnetization interaction over different layers. Individual layers have an overall magnetization, but the magnetization between layers can differ.

If the domain orientation between two layers is anti-parallel, this causes inefficiency in the polarizing performance of the supermirror as certain layers reflect the undesired spin component. As supermirrors are built of an aperiodic multilayer system, the coupling between the layers is non-trivial and great effort has to be made to align all layers in the same direction ([60, 61] and references therein). The magnetic properties of a multilayer system differ from the behavior of a monolayer due to these couplings [61]. The initial magnetic orientation of the layers of a remanent supermirror without a holding field has been found to be dominated by its production rather than the crystallography of the layer [61].

Previous investigations in magnetization and consequently depolarization in supermirrors focused especially on remanent supermirrors with a FeCoV alloy as the ferromagnetic layer material. Remanent mirrors have the advantage that they are not limited to one polarization orientation: by inverting the guide field [44], neutron spin directions can be selected. This procedure allows to invert the polarization without having to use an additional spin flipper, provided that the magnetic domains hold their direction. In this section, the study of depolarization in supermirrors is extended to standard FeSi and CoTi mirrors.

Depolarization experiments are a tool to study the magnetism of materials [59, 62] and thus can be used to improve the performance of supermirror polarizers performance.

The magnetization and coupling between layers can be studied by looking at the specular scattering, where incidence and reflection angle are identical. While specular scattering is the tool of choice for in-depth analysis of the sample, off-specular scattering provides information about the in-plane properties. Off-specular scattering arises from inhomogeneities in the sample plane, such as roughness in the sample or magnetism. Inhomogeneities in the magnetic structure of a plane lead to a varying lateral magnetic potential [63]. Kentzinger et al. [60] have performed a comprehensive study on the magnetization of the layers in a remanent FeCoV supermirror. They found imperfections in polarization to be due to inverted magnetizations in layers and reported furthermore spin flips occurring in off-specular scattering due to incomplete in-layer magnetization. For their mirror, Kentzinger et al.

found the thin layers easier to magnetize than thicker layers [60].

This section of the chapter presents depolarization measurements that are aimed for a better understanding of polarizing supermirrors. In this section, supermirrors are not considered a polarizing device but simply a sample that has an influence on the initial polarization. This influence can be both an increase or a decrease of the neutron polarization. The goal is to apply this understanding to create well-performing polarizing devices with supermirrors. Therefore, the investigation is largely phenomenological with conditions similar to the ones encountered in a neutron beta decay experiment. While the main goal is application, the microscopic understanding certainly also contributes to a better performance. The depolarization was tested mainly at PF1b with the OTB in a basic reflectometer geometry (Sec.4.2.2). Additional, refined measurements were taken on the SuperADAM site.

### 4.2.1 Samples

The samples were produced with the generous support from professional supermirror production sites, the Service d'Optique des Neutrons at ILL and SwissNeutronics. Initially, several parameters were to be investigated: magnetizing field strength, materials, supermirror factors, incidence angles and wavelength. This led to the sample set listed in Table 4.3. SwissNeutronics provided a series of FeSi supermirrors produced under identical conditions, samples C, D and E as well as monolayers of different thicknesses, A and B. In addition, ILL provided an iron  $m=3.6$  mirror (sample 2 and 7) as well as a  $m=1.9$  sample and a monolayer of  $2000 \text{ \AA}$ . However, the iron target was changed between the production of mirrors samples 2 and 7 and the production of samples J,K, L and M. The new target was a purer iron [64]. They also manufactured custom-made FeSi pseudo-mirrors that are further described in Sec. 4.2.4. In addition, Thorsten Lauer from University of Mainz provided a  $m=1.5$  mirror as well as two different kinds of iron monolayers. CoTi and Co monolayer samples were all provided by the Service d'Optique des Neutrons at ILL.

Fe			Co		
monolayer thickness [Å]	production site	sample name	monolayer thickness [Å]	production site	sample name
50	SwissNeutronics	A	800	ILL	11
1500	SwissNeutronics	B	2000	ILL	9
1500 (soft)	Uni Mainz	10a			
1500 (hard)	Uni Mainz	10b			
2000	ILL	K			
FeSi			CoTi		
$m$ -value	production site	sample name	$m$ -value	production site	sample name
1.5	SwissNeutronics	C	2.0	ILL	3
2.0	SwissNeutronics	D	2.8	ILL	1
3.8	SwissNeutronics	E	CoTiGd		
1.9	ILL	J	2.8	ILL	5
3.6	ILL	2,7			
1.5	UniMainz	12			
2.0 Pseudo 20 Å	ILL	M			
2.0 Pseudo 100Å	ILL	L			

Table 4.3: The samples (ferromagnetic monolayers and polarizing supermirrors) tested for depolarization .

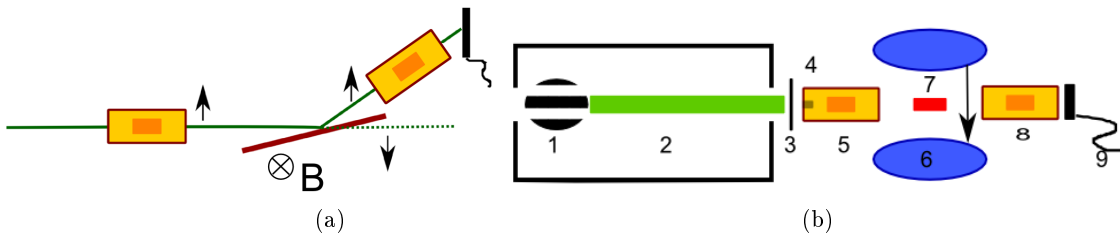


Figure 4.9: Set-up of the OTB in reflectometer geometry. (a) View from above on the central part: Polarization by helium filter, reflection of the  $\uparrow$  and transmission of the  $\downarrow$ , analysis of the reflected beam in the second helium filter and subsequent detection. (b) Detailed view from the side: (1) Velocity selector (2) Neutron guide (3) Shutter (4) Be filter (5) Helium polarizer (6) Electro-magnet (7) Sample (8) Helium analyzer (9) Detector

#### 4.2.2 The Experimental Set-up

Two beamtimes at PF1B, one in November 2011 and one in July 2012, were devoted to study the depolarization in polarizing supermirrors. The 2011 beam time concentrated on CoTi mirrors, the one in 2012 more on FeSi. The set-up of the OTB was used with a mirror between the analyzing and the polarizing cell. The OTB acted as a basic reflectometer, shown in Fig. 4.9 a). The set-up of the OTB got altered, as the sketch in Fig. 4.9 (b) shows, such that a supermirror sample could be placed between the helium analyzer and polarizer. It was exposed to different magnetizing fields via an electromagnet. The measurements were taken at constant wavelengths of  $5.3 \text{ \AA}$  and  $7.4 \text{ \AA}$ . The replacement of the chopper (white, pulsed beam) by a velocity selector (1 wavelength, continuous beam) was favorable in terms of statistics due to the continuity of the beam. The wavelength of  $5.3 \text{ \AA}$  is typical for applications of polarization of a cold neutron beam in neutron beta decay experiments and it is close to the maximum flux of the of the cold beam [57]. In this section, the set-up components are going to be described in detail.

The exit of the polarizer magic box and the entrance of the analyzer magic box were situated at a distance of ca. 85 cm each from the magnet center. In order to provide a continuous quantization axis for the neutrons, a magnetic guide field was installed. It measured about 1.4 mT at the beam center without the electromagnet turned on. It was verified that no large field gradients were present over the neutrons' flight path. Also, the guide field

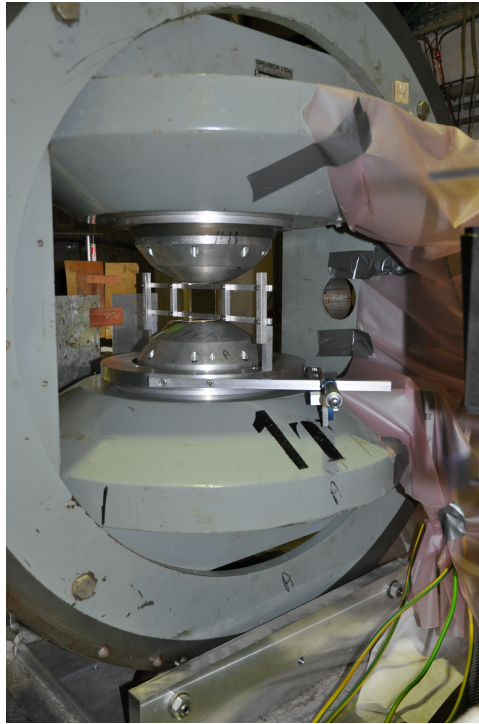


Figure 4.10: The sample holder inside the D3 Magnet with sample.

was sufficiently low to not corrupt the field shielding of the MBs.

The detector behind the analyzer magic box was set on a motorized axis that permits to scan over a distance of 2 m in horizontal direction (perpendicular to the beam). The detector opening accepts a total divergence of about 2mrad. In order to find the reflection peak, the axis was scanned each time a new angle and/or mirror was positioned. Usually and especially during the 2011 beam time, scans with the parallel cells in white and black orientation for reflection were conducted to discriminate the reflection peak clearly against background, Fig. 4.12.

A Dornier velocity selector preceded the casemate guide and replaced the chopper used in Sec. 4.1.1. The beam was confined to a 0.2 mm width at the guide's exit, where additionally a shutter was installed for background measurements. A second slit at the electromagnet's entrance of 1 mm was installed to define the divergence and lateral extension of the beam. Through the two collimating slits before the sample, the beam has a divergence of about 1 mrad. The mirror samples were on the holder in the electromagnet,

#### 4.2. DEPOLARIZATION MEASUREMENTS IN POLARIZING MIRRORS 41

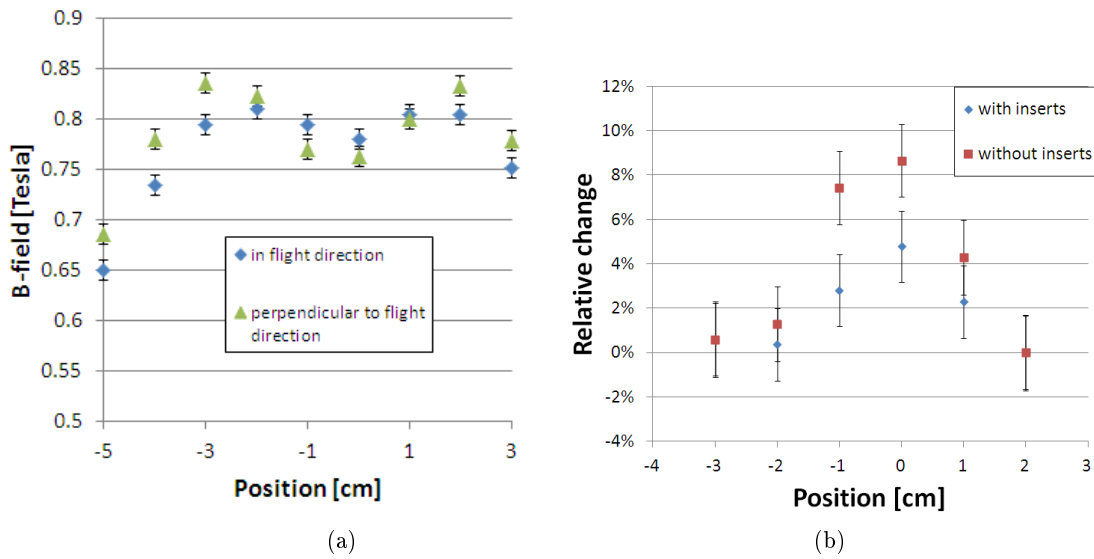


Figure 4.11: Field Scans of the D3 Magnet at 50 Ampere. Measurement errors are conservatively estimated to be 0.01T as for the fluctuation of the Hall probe used. (a) Horizontal Scans in and perpendicular to the flight direction of the neutrons without inserts. (b) Relative change with respect to the edge of the pole hole at position 2 [cm] in the field with and without inserts over the insert area.

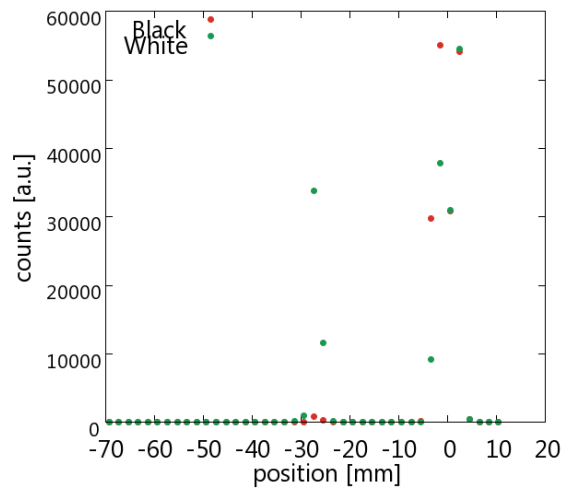


Figure 4.12: Scan for the reflection peak with cells parallel and anti-parallel configuration. Direct beam at position 0, the distance between sample and detector is 156cm.

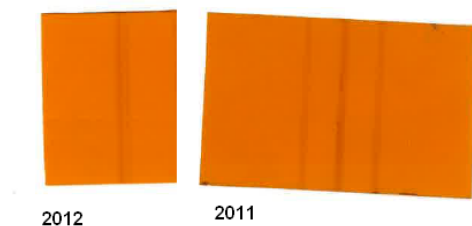


Figure 4.13: Gd Paper used to center the magnet. The paper changes color when irradiated with neutrons. The paper plane was perpendicular to the beam direction and the paper was turned by 180 degrees. Distance 2012: 1 mm. Distance 2011: First 8.5 mm, after adjustments not discernible (center line).

shown in Fig. 4.10. The magnet was kindly provided by Anne Stunault from the D3 instrument at ILL. It is used there normally as a sample environment with central holes in the magnet poles. They lead to inhomogeneities in the magnetic field with sharp edges as can be seen in Fig. 4.11 a. Therefore, polar inserts were added: cylinders made from soft iron. Unfortunately, when positioned to completely fill the polar holes, the attractive magnetic forces were bigger than gravity at maximal field and a permanent, removable fixation not possible. Therefore, the polar inserts had to be distanced a bit more, leaving a 5 mm gap from the insert to the edge of the pole holes. In Fig. 4.11b the horizontal cut of the field map without and with polar inserts are shown. While the inserts could not completely correct the inhomogeneities, they smoothen the field variations.

The electromagnet was positioned to be centered on the neutron beam. This was done with a Gd-paper at the place of the sample, in the sample holder, with the holder turned 90 degree with respect to the beam direction. This orientation succeeded very well in 2011 and a bit less good in 2012, see Fig. 4.13.

Shielding and beam collimation in the area between polarizer and analyzer was made not from the usual boronated rubber which often has small ferromagnetic impurities, but LiF rubber for the second slit and protection on the magnet poles and the frontal areas of the holder. The same Gd-painted cardboard protections already used for the validation of the OTB were installed in the MBs. Neutron background shielding in the area with some distance from the neutron beam, such as in the guide field installations and protection



## 4.2. DEPOLARIZATION MEASUREMENTS IN POLARIZING MIRRORS 43

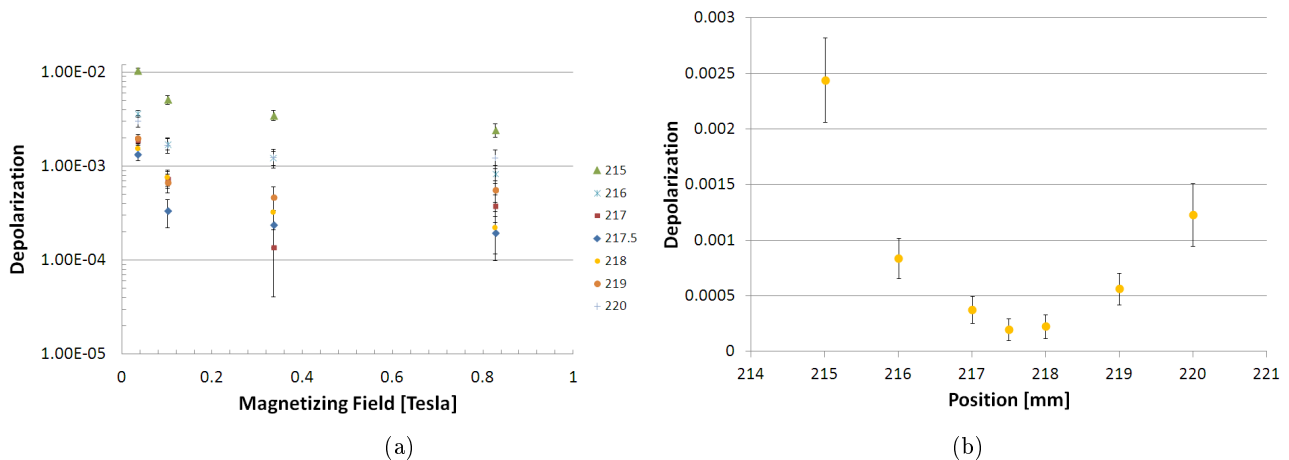


Figure 4.14: Depolarization of a FeSi  $m=2.0$  supermirror at  $\theta = 17.1$  mrad for different detector positions. (a) Magnetic field scan for positions in the transmitted beam (b) Depolarization at maximum field 0.82 T for all positions. Previous scans without sample present had set the center of the direct beam to be at 217.5 mm.

on and around the magic box exit were still made out of boronated rubber and boron loaded polyethylene bricks, as they were not in contact with the polarized beam.

The samples were sputtered on 39 mm x 60 mm Si wafers. The height was determined by the poles' distance in the magnet between which the samples would be placed, the width by the homogeneity of the magnetic field. The thickness of the wafer varies with the manufacturer. Tab. 4.3 resumes all the samples involved in the depolarization measurements. The samples were placed in a sample holder produced from Al: A rectangular structure held the sample in place: The sample was pressed between two rods on the top and bottom, where one of each rods had an indentation of 0.5 mm depth, see Fig. 4.10. The angular position of the sample was set with a micrometer screw. The holder is constructed in a way that the coated wafer plane is in the magnet's center.

Both transmission and reflection of polarized beam interacting with a polarizing supermirror were studied. The transmissive measurements required some more care than the reflective one. The reflection peak can be singled out by scanning the axis, as described above. For transmission, some modification was necessary: The incident beam covers more than the sample if the

angle between sample and beam is in the order of the critical angle. In addition, the neutrons are refracted, not only by the reflective coating but mostly by the Si sample carrier, deflecting the transmitted beam. Consequently it is possible for neutrons that were not in touch with the sample to be mixed with the ones which were. This may overestimate the depolarization as these other neutrons did not encounter the sample or these neutrons possibly came in touch with slightly magnetic set-up equipment such as the holder screws. The detector slit was therefore reduced to 0.5 mm width and the depolarization was measured at different positions behind the sample. Assuming that the maximum magnetizing field minimizes the depolarization from the sample, see Fig. 4.14, the best position to measure the depolarization in transmission was sought out at maximum field. Fig. 4.14 b indicates the optimum position for the least contamination with direct beam neutrons to be close to the center of the direct beam. This made it possible to properly measure depolarization in transmission due to the sample.

The polarization of the beam is determined by flipping one of the two helium cells. This measures the product of analyzing and polarizing power,  $AP$  (compare Eqn. 3.14). The comparison between the direct beam and the beam with the sample present is the depolarization caused by the sample.

In the 2011 beam time, polarization of the direct beam was usually measured once in the morning for each cell batch. Measurement points were taken at 6 field values: 0.02 T, 0.1 T, 0.2 T, 0.33 T, 0.53 T, 0.82 T including two background measurements at 0.02T and 0.82 T. The 2012 beam time followed the same principles as the one from 2011. The measurement protocol was refined based on the results from 2011: Only 4 points in the magnetic field were measured (0.1 T, 0.3 T, 0.5T, 0.82 T) including two background measurements with a closed shutter at 0.1 and 0.82 T, the measurement of each data point was shorter (but still ensured sufficient statistical precision). The polarization of the direct beam was measured more often, ideally after or before each sample change, so that changes in helium polarization could be safely corrected for. This makes it possible to deduce the actual depolarization. The 2012 beamtime concentrated mainly on the FeSi samples. A few Co samples were also measured. The results are consistent with the measurements from 2011. As the measurement of the direct beam polarization was frequent in 2012, the amount of depolarization of the beam can easily be deducted. For the 2011 beamtime, this is more difficult to achieve.

Therefore, the data presented uses the measurements from 2012 when available. First results from 2011 had been published [65] but were re-analyzed for this thesis. As for data from 2011 presented, only relative comparisons can be made. Care is taken to only present subsequent measurements or compare data taken on similar time scales after filling of the cells when comparing measurements from different cell batches. During the measurements, care was taken that the order of the measurement does not corrupt the results: supermirror factors  $m$  as well as incidence angles were not measured in successive order but starting with the extreme values of the parameter and a subsequent non-monotonous scan of the values, as the change in helium polarization might contribute to an undesired drift. During data analysis, particular attention was paid to the measurement order and indeed, all results are free of such order-related issues. The magnetizing field was always constantly driven from lowest to highest value in order to accommodate for possible hysteresis-linked effects.

### 4.2.3 General Observations

In this section, general observations and characterization on supermirrors are made regarding depolarization. For our experiments, we used the magnetizing field as a guide field. Hence, if the mirrors are completely magnetized by the field, the spin should be parallel perfectly parallel to the magnetization.

A clear picture can be drawn from the position sensitive scattering at the instrument SuperADAM. A FeSi and a CoTi  $m=2.0$  mirror have been introduced into SuperADAM's highly collimated beam. All four spin states of the neutrons scattered at different angles have been measured as a function of incident angle using wide angle supermirror analyzer. Fig. 4.15 illustrates typical off-specular maps measured for CoTi  $m=2.0$  supermirror for all four spin channels. The top maps depict non-spin flip off-specular scattering. The bold, diagonal line across the map illustrates the specular scattering where incident angle matches the outgoing one. Large difference between specular signal for  $\uparrow\uparrow$  and  $\downarrow\downarrow$  states indicate very high polarizing power of the mirror. The spin flip maps at the bottom of Fig. 4.15 show rather large spin leak in the specular reflection indicating that analyzing and polarizing efficiency of the instrument is well below 100 % This makes the direct estimation of the absolute polarization of the sample impossible

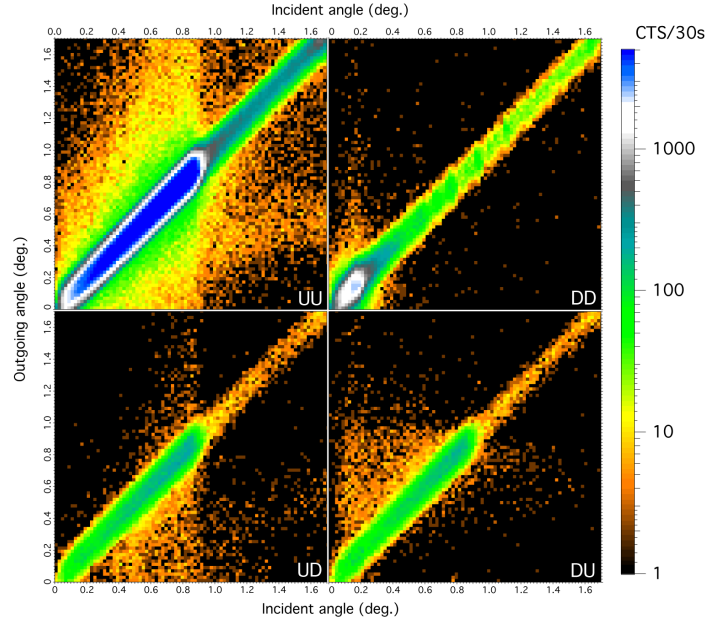


Figure 4.15: Non spin flip and spin flip off-specular scattering of CoTi  $m=2.0$  supermirror at 0.035 T. All four combinations of (U)p and (D)own are shown.

without the knowledge of the exact sample composition. However, the off-specular scattering can give indications about the depolarization processes as it is sensitive to inhomogeneities of the scattering length density along the sample surface. The off-specular scattering in non-spin flip regime is normally symmetric with respect to the specular line. The spin flip scattering on the other hand is anti-symmetric with respect to the specular line e.g.  $I(\theta_f, \theta_i)^{\downarrow\uparrow} = I(\theta_i, \theta_f)^{\uparrow\downarrow}$ . The spin flip maps indeed contain an off-specular feature which is anti-symmetric with respect to the specular ridge. This is a result of the spin flip scattering from the misaligned magnetic domains along the layer surface. The two maps at the top of Fig. 4.16 show the same spin-flip off-specular scattering measured for FeSi  $m=2.0$  supermirror measured at minimal and maximal applied magnetic fields, 0.035 T and 0.8 T respectively. As seen from the maps, the observed asymmetric off-specular feature is significantly suppressed at high magnetizing field. This is direct evidence that the depolarization in supermirrors is primarily caused by misaligned magnetic domains in the mirror. While the specular line in the spin-flip channels possibly can contain small depolarizations from the mirror itself,

#### 4.2. DEPOLARIZATION MEASUREMENTS IN POLARIZING MIRRORS 47

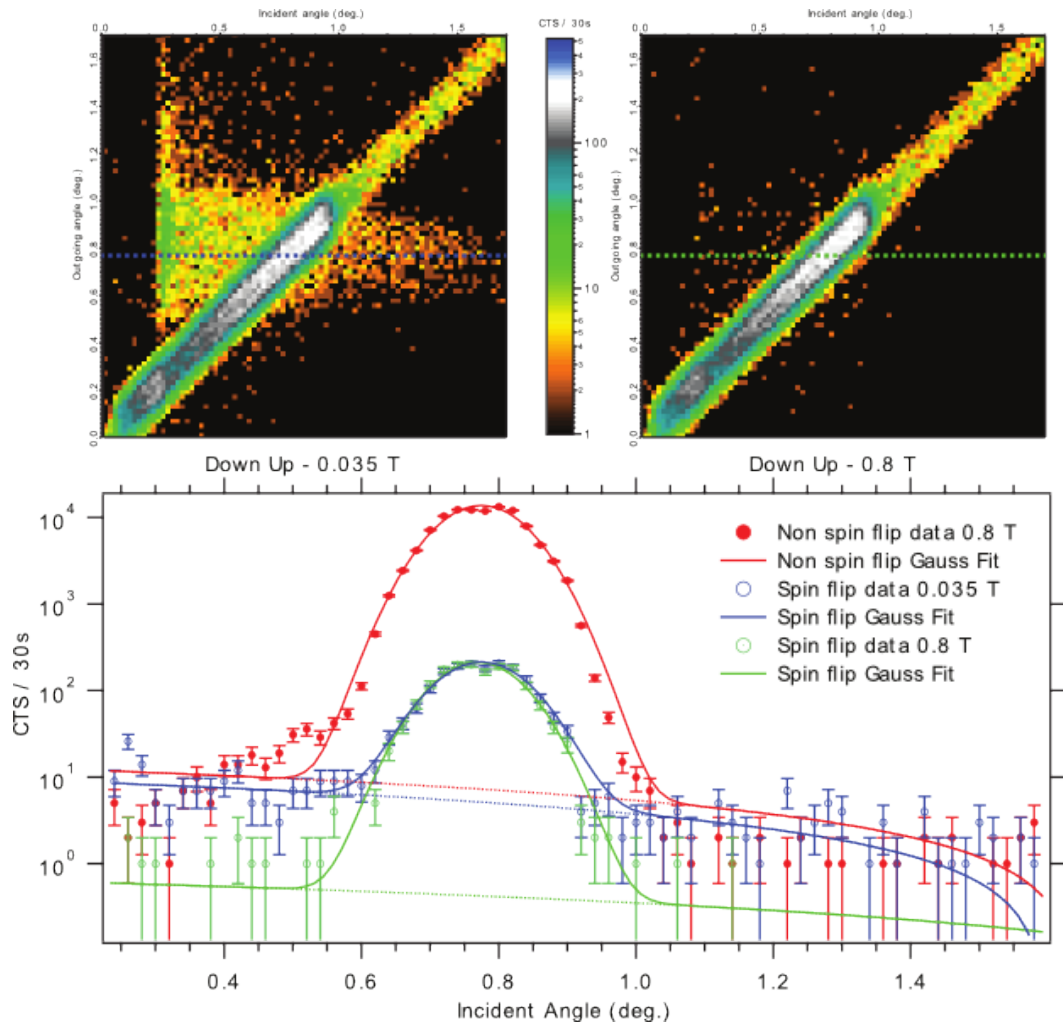


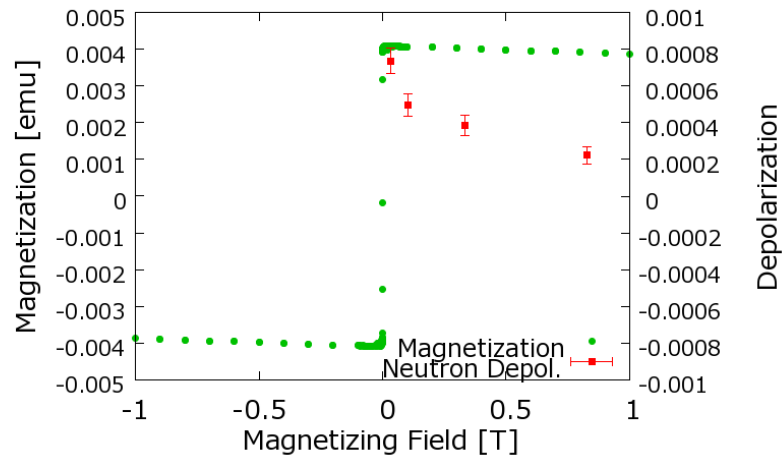
Figure 4.16: Spin flip off-specular scattering of FeSi  $m=2.0$  supermirror for minimal and maximal applied magnetic fields at the top. At the bottom, a horizontal cut is shown for spin flip at maximum and minimum field as well as a non-flip cut at maximum field are shown. This can be used for a first estimation of depolarization. Peaks are fitted as a Gaussian.

the observed off-specular depolarization is only due to the sample and can be used to set lowest boundaries on the depolarization by comparing the off-specular contribution in the specular region of the beam to the specular reflection in the  $\uparrow\uparrow$  state. Such an estimation is illustrated at the bottom of Fig. 4.16 for a fixed outgoing angle. In this cut, the depolarization due to the insufficiencies of the instrument are taken from the 0.8 Tesla measurement of the  $\uparrow\uparrow$ -channel, as it should not contain spin flips due to the sample. As a result, the depolarization due to the sample of the reflected beam at 0.035 T is at least  $4 \cdot 10^{-4}$  and at 0.8 T  $5 \cdot 10^{-5}$ . Those estimates are a first, rough quantity for the lower limit of depolarization.

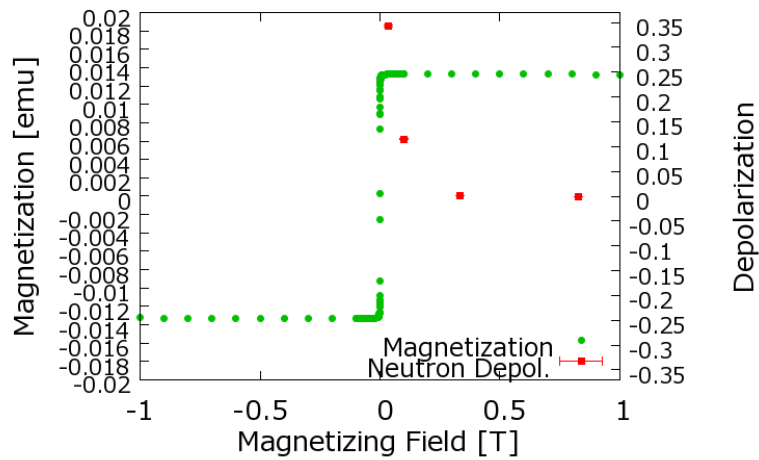
Polarized neutrons and their depolarization through matter are a way to study the magnetization of a material [28, 59, 62]. Fig. 4.17 reports the depolarization of a neutron beam by a Fe and a Co monolayer and their hysteresis curve obtained by a SQUID-measurement. While the SQUID shows a saturation at about 0.1 T, the neutron method shows that in fact there is a significant depolarization beyond this limit up to the maximum 0.8 T that could be attained by the magnet. In this area, the SQUID measurement does not show any change in magnetization within the precision of the measurement. Indeed, the SQUID measures simply the average magnetization while the neutron probes the material more deeply. The SQUID measurement therefore is not sufficient in order to determine the saturation of a mirror on this level of measurement accuracy. Depolarization of neutrons to study magnetism at is applied here is very sensitive to yet not completed magnetization and the relative changes. In the following, results from the OTB are presented with high resolution in the polarization. The resolution of the set-up is such that both the specular and the off-specular scattering are detected. The emphasis lies on the quantitative, precise characterization of the depolarization as it would occur in a neutron beamline.

With the OTB set-up, the hysteresis of supermirrors was investigated. The magnet was ramped several times up to the maximum field with the sample inside. As the field of the electro-magnet could not be easily inverted, the sample was turned by 180 degrees, inverting its orientation to the magnetic field. The results are shown in Fig.4.18. At low field, repetitive runs show less depolarization, hence, a better alignment of the

4.2. DEPOLARIZATION MEASUREMENTS IN POLARIZING MIRRORS 49



(a)



(b)

Figure 4.17: Comparison of the magnetization via SQUID measurement vs. the depolarization of a neutron beam measured by the OTB for a single 2000 Å thick layer (a) Co-layer with incidence angle 5 mrad (b) Fe-layer with incidence angle 6 mrad

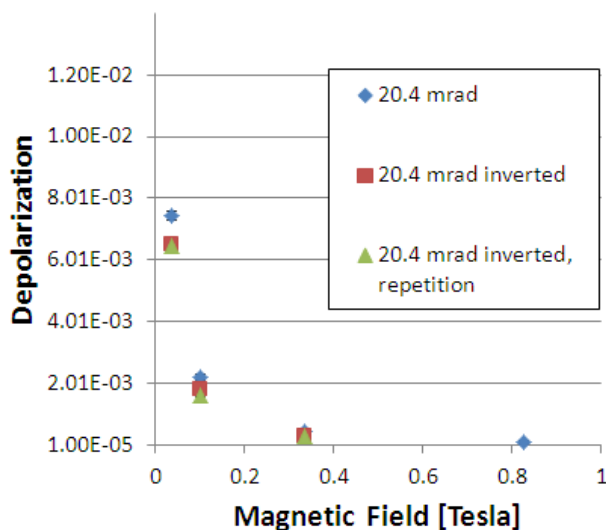


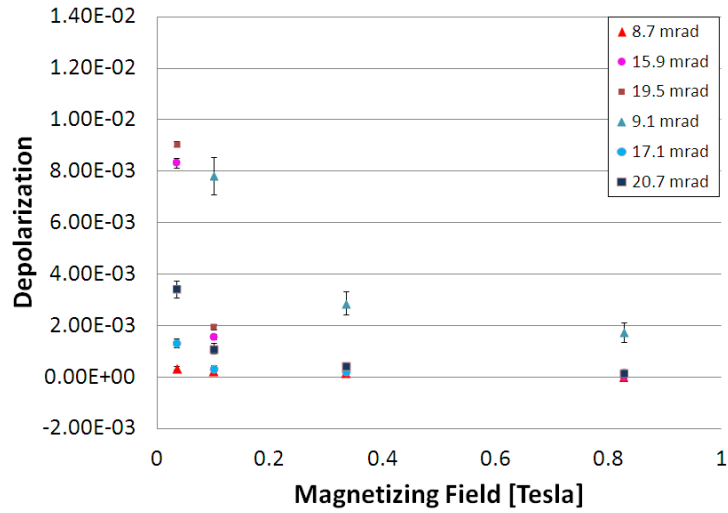
Figure 4.18: Depolarization in a  $m=3.8$  FeSi supermirror at 20.4 mrad incidence angle measured in reflection. The mirror orientation has been inverted with respect to the magnetic field between measurements.

domains. At high field however, the difference is not statistically significant. A subsequent turn of the sample and therefore inversion of the field shows no significant difference to the saturated mirror before the turn. This means, the domains are either still aligned as they were before or switched their orientation completely. Depolarization measurements are only sensitive to perpendicular magnetic components [62]. After initial magnetization, the amount of perpendicular components does not change anymore at a given field.

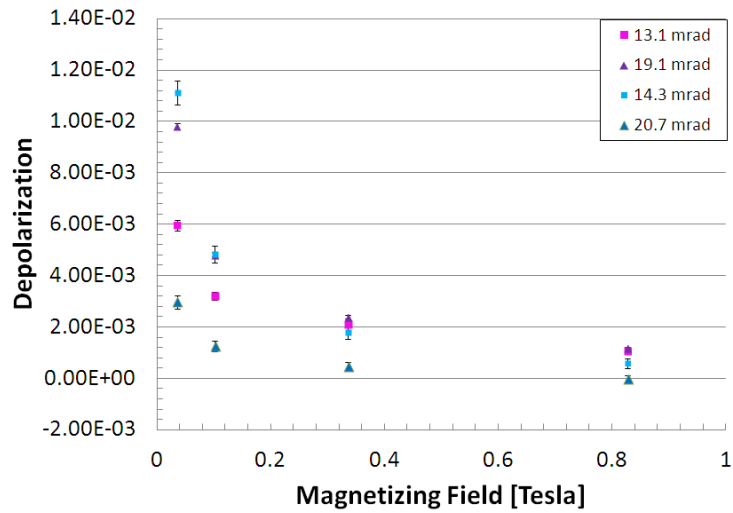
For Fe, two layers of 1500 Å Fe were compared. Beforehand, their magnetic behavior was characterized as "soft" and "hard" by SQUID measurements. The layers were sputtered from the same material but the sputtering parameters were adjusted such that the layers obtained the desired magnetic properties [66]. Their performance in the OTB is shown in Fig. 4.20. It must be noted that the mirrors had been exposed to magnetic fields before the measurements were taken. The early saturation of the soft mirror is clearly visible. Furthermore, it depolarizes generally less than



4.2. DEPOLARIZATION MEASUREMENTS IN POLARIZING MIRRORS 51



(a)



(b)

Figure 4.19: Comparison of the depolarization in reflection (red) and transmission (blue) at different incidence angles (a) FeSi  $m=2.0$  (b) CoTi  $m=2.8$

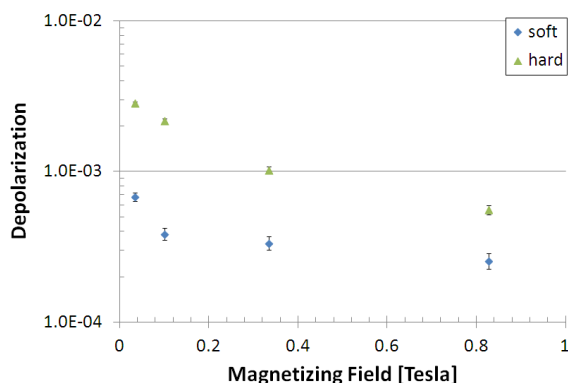


Figure 4.20: Depolarization measured in reflection for 1500 Å thick Fe layers with different magnetic properties.

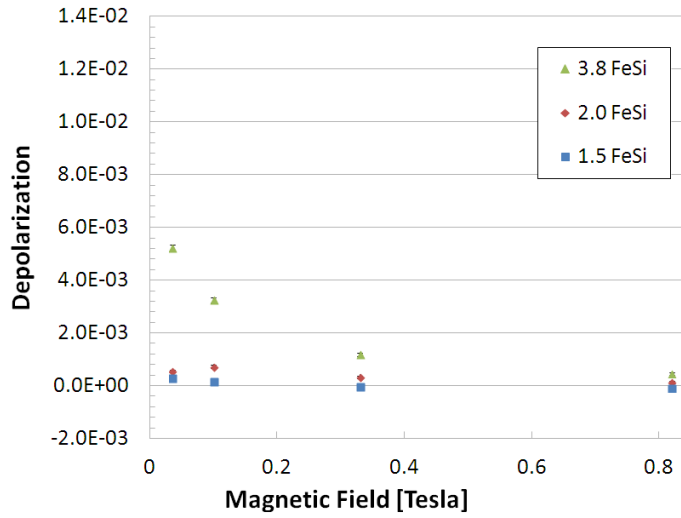
the hard-magnetic layer. In order to apply this result to the supermirror production, it is important to maintain the magnetic "soft" property over all layers despite couplings between layers. This can be tested by specular polarized neutron scattering at varying field if the layer sequence is known.

The results presented up to now were all derived from the reflected beam, but depolarization equally takes place in transmission. A comparison for depolarization for different mirrors is shown in Fig. 4.19. The depolarization is of the same order of magnitude in both modes and shows the same behavior with respect to the increase of the magnetizing field. Measurements in the OTB revealed depolarization up to  $10^{-2}$  at low fields (0.035 T). At high field (0.82 T), this depolarization can be suppressed to be at maximum a few times  $10^{-4}$ . The tendency is that at low magnetizing field, transmission depolarizes the beam more than reflection and that at high magnetizing field, it depolarizes a bit less than reflection. However, the effects are considerably smaller than the influence that is brought by the magnetizing field.

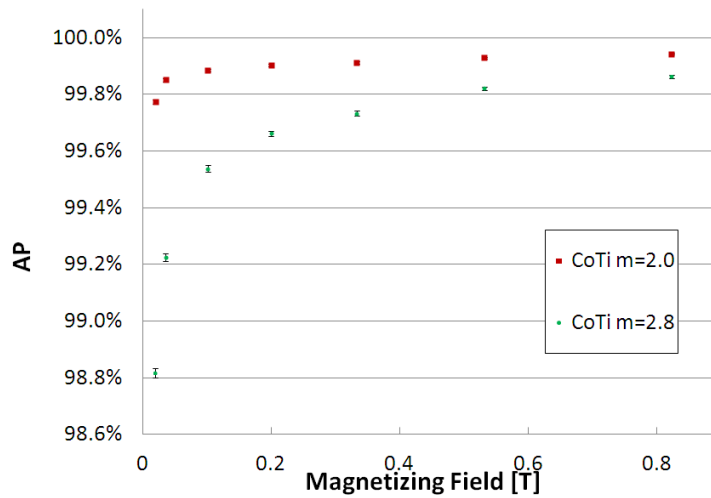
#### 4.2.4 Individual Layers

The previous section discussed the general behavior and origin of depolarization in polarizing supermirrors. In this section, the character of the depolarization is looked at more closely. The information can be used to make the optimum choice when looking for a suitable supermirror for a polarizing

#### 4.2. DEPOLARIZATION MEASUREMENTS IN POLARIZING MIRRORS 53



(a)



(b)

Figure 4.21: Comparison of the depolarization in reflection by mirrors with varying  $m$ -values for constant incidence angle of 20 mrad. (a) FeSi from SwissNeutronics (b) CoTi from ILL, the  $AP$  is shown.

device. By varying the incidence angle and/or the wavelength, different layers of the supermirror are probed. The angular resolution of the set-up on the OTB is not good enough to gain reliable information of a specific layer but general tendencies can be deduced. In addition, the influence of the

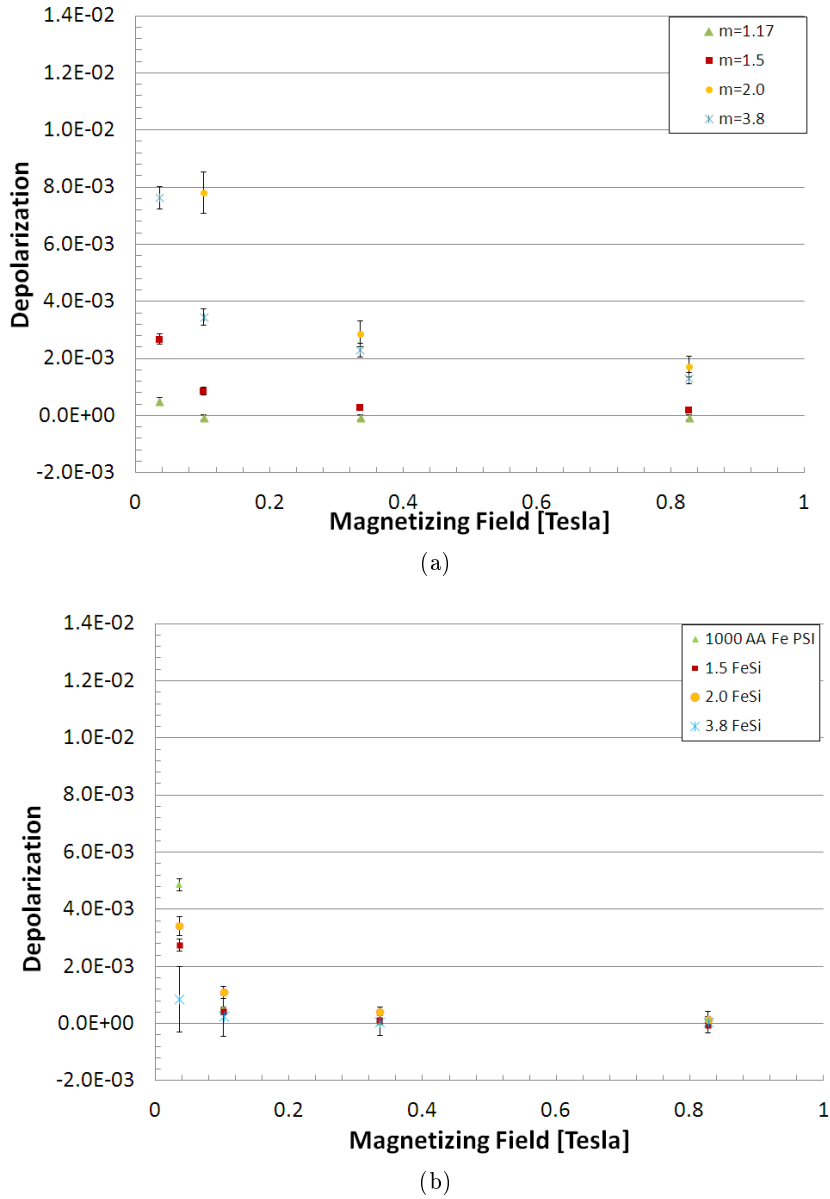


Figure 4.22: Comparison of the depolarization in transmission by FeSi mirrors with varying  $m$ -values for constant incidence angle (a) Incidence angle 9 mrad (b) Incidence angle 20 mrad

supermirror factor  $m$  and of absorbing layers was looked at.

The supermirror factor ( $m$ ) has an influence on the depolarization. Fig. 4.21 depicts the depolarization in a series of FeSi mirrors from

#### 4.2. DEPOLARIZATION MEASUREMENTS IN POLARIZING MIRRORS 55

SwissNeutronics and two CoTi mirrors from ILL. For a given incidence angle, the depolarization is more pronounced for higher  $m$ -values. These measurements were performed in reflection. As supermirrors are sputtered from the thinnest to the thickest layer, the amount of matter traversed by the neutron is the same for the mirrors. However, the roughness of the layers has a tendency to be higher for the layer of a higher  $m$  mirror. In application, the lowest  $m$ -value that is sufficient for the given beam divergence and possible curvature of the mirror is the best choice as it minimizes depolarization effects in these conditions. When measured in transmission, the following picture is given, see Fig. 4.22: For a series of FeSi mirrors at constant incidence angle of ca 9 mrad, the tendency is to have a higher depolarization at higher  $m$  value. The polarizing reflection at this angle takes place on the "bulk", the thickest, the first layer. At the constant incidence angle of ca 20 mrad, just around the critical angle for  $m=2$ , the depolarization is high for all samples that cannot reflect this angle and lower for  $m=3.8$  which still has polarizing power at this angle.

The dependence of depolarization on the incidence angle was probed as well as on the wavelength. The general tendency is to have higher depolarization for low angles at low fields and the contrary at high fields; the field dependence is more pronounced for high angles. This is true for multiple  $m$  factors. Results are shown for several mirrors in Fig. 4.23, 4.24 at different angles and for the two wavelengths available. For 7.4 Å, the effects are more distinct. Thin layers in a supermirror (high angles) are easier to magnetize [60]. This might be expressed by less depolarization at high fields. The results confirm and generalize similar findings [61, 67, 68].

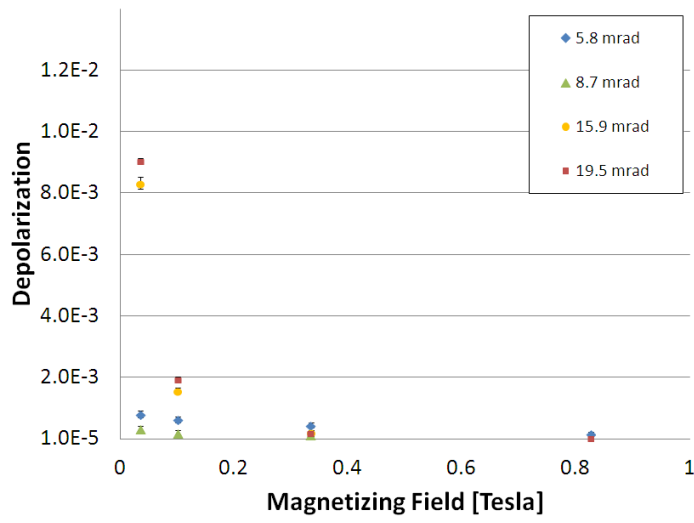
For the transmissive measurements, the results are less clear. While the transmissive depolarization is comparable to the reflective one in order of magnitude, the study of incidence angle is less conclusive, see Fig. 4.19.

Both sample material combinations, CoTi and FeSi, show similar behavior in terms of angle, wavelength and supermirror factor. Amongst the two, CoTi performs better at low field while FeSi has lower depolarization at high field, see Fig. 4.25, Fig. 4.21. For CoTi, the depolarization remaining at maximum field is ca.  $1 \cdot 10^{-3}$  for  $m=2.8$  and ca.  $2 \cdot 10^{-4}$  for the  $m=2.0$  mirror. As for FeSi, the remaining depolarization at maximum field is beyond the experimental sensitivity of the OTB. In a few cases, the

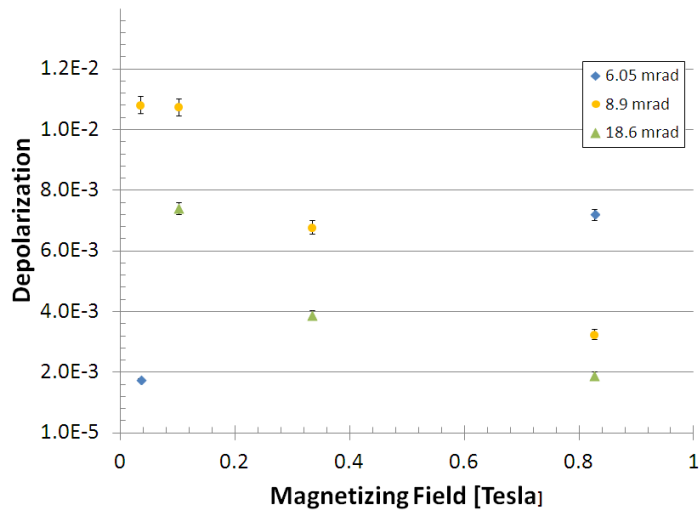
depolarization becomes slightly significantly negative. This translates to a "re-polarization" of the beam by the sample, see Fig. 4.23 (a-c). From the sample set available, the use of FeSi at high field is therefore clearly advised.

Polarizing supermirrors often have an absorbing layer in order to prevent reflection of the wrong spin direction, see Sec. 3.3.3. In the case of CoTi mirrors, this is achieved with a Gd layer. FeSi mirrors do not need an absorbing layer as long as they are sputtered onto a Si carrier as in the presented case, there is no potential difference as it is the same material that is also used for the non-magnetic layer. Mirrors with absorbing layers cannot be used to polarize in transmission, which is why most of the CoTi samples used for the depolarization measurement were produced without a Gd layer. A comparison in the OTB of a CoTi  $m=2.8$  supermirror with and without Gd shows that there is no significant performance change in terms of depolarization between the two mirrors, see Fig. 4.26.

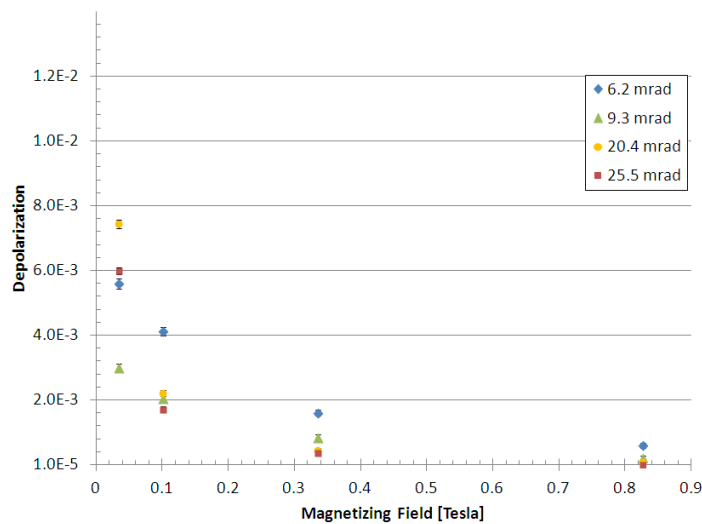
#### 4.2. DEPOLARIZATION MEASUREMENTS IN POLARIZING MIRRORS 57



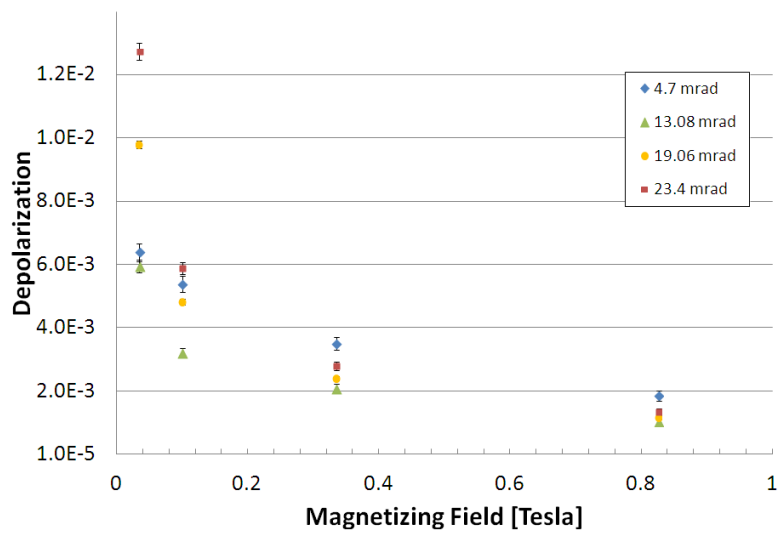
(a) FeSi m=2.0



(b) FeSi m=3.6



(c) FeSi m=3.8

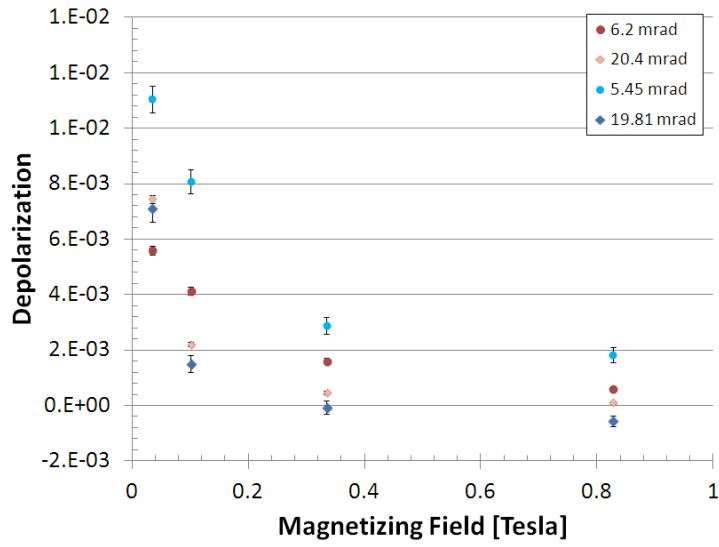


(d) CoTi m=2.8

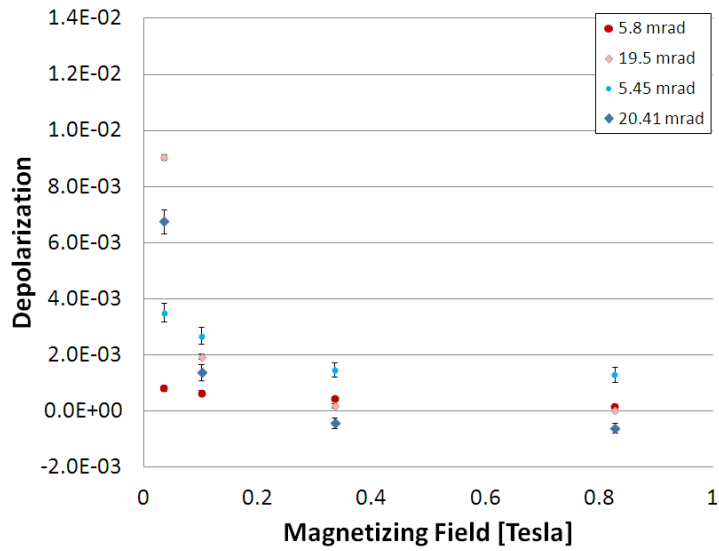
Figure 4.23: Depolarization for different incidence angles on FeSi m=2.0, 3.6 and 3.8 as well as CoTi m=2.8



4.2. DEPOLARIZATION MEASUREMENTS IN POLARIZING MIRRORS 59



(a) FeSi  $m=3.8$



(b) FeSi  $m=2.0$

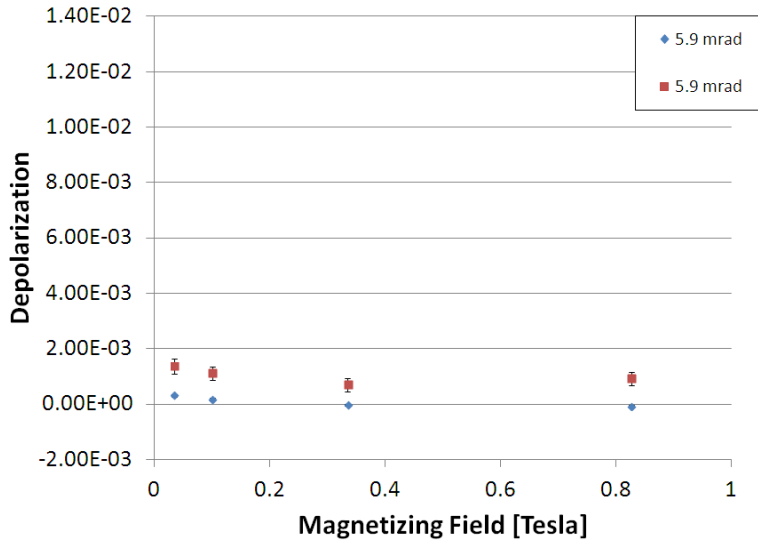
(c) FeSi  $m=1.5$ 

Figure 4.24: Comparison of the depolarization in FeSi supermirrors at 5.3 Å (red) and 7.4 Å (blue) at different incidence angles

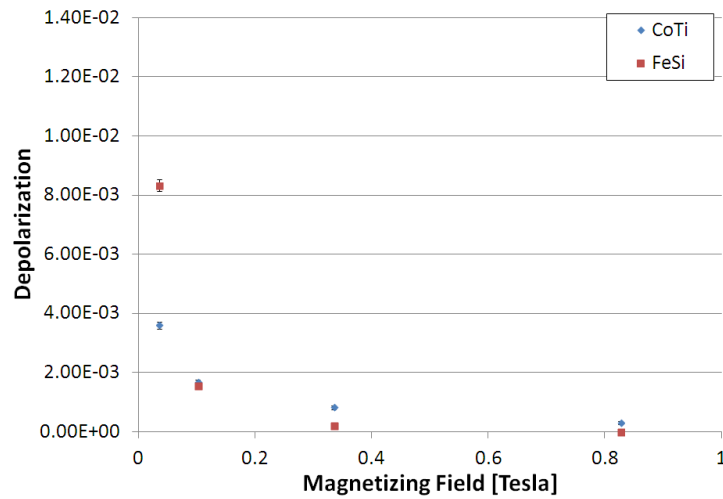


Figure 4.25: Depolarization in  $m=2.0$  supermirrors at 20 mrad incidence angle, measured in reflection

4.2. DEPOLARIZATION MEASUREMENTS IN POLARIZING MIRRORS 61

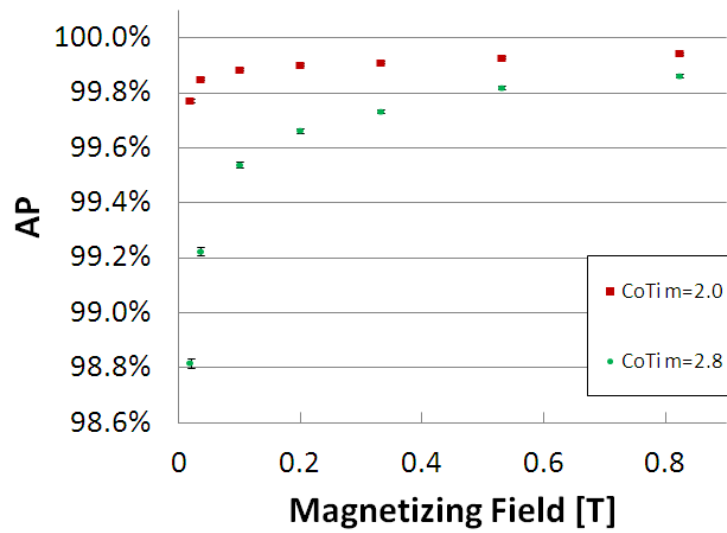


Figure 4.26:  $AP$  comparison of a CoTiGd and a CoTi mirror with  $m=2.8$  at  $\theta = 18$  mrad incidence angle, measured in reflection.

### 4.2.5 Pseudo-Supermirrors

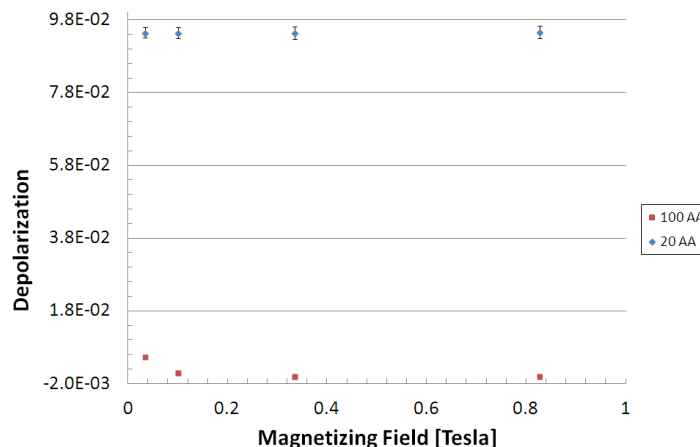


Figure 4.27: Depolarization of two Pseudo-supermirrors with a constant Fe-thickness of 20 Å and 100 Å.

Two pseudo-supermirrors were created for a further investigation into the depolarization process in terms of layer thickness of the ferromagnetic material and coupling between layers. Pseudo-supermirrors were produced based on a FeSi  $m=2.0$  mirrorlayer sequence: the thickness of the iron was constant in all layers while the Si layers varied as they would in a normal mirror. This was done at ILL Service d'Optique des Neutrons for two different thicknesses of iron: 20 Å and 100 Å. Fig. 4.27 resumes the results for the two mirrors. The depolarization at a given angle is lower for the thicker Fe layer. In 2001, Kraan et al performed a similar study on a set of (FeCo)(TiZr) periodic multilayers with constant FeCo width. The depolarization behaved similarly in this range of thickness [61].

### 4.2.6 Depolarization By A Bender

In Sec. 4.2, the depolarization in a supermirror for a single reflection was shown. In this section, the depolarization for a bender typically used in a particle physics experiment is reported; this section resumes results presented in [69]. The TOF-set-up of the OTB (Sec. 4.1) was used to test a CoTi Schärpf bender. Fig. 4.28 shows both the  $AP$  of the two helium cells with and without the bender present. Clearly, the depolarizing effects in the order

## 4.2. DEPOLARIZATION MEASUREMENTS IN POLARIZING MIRRORS63

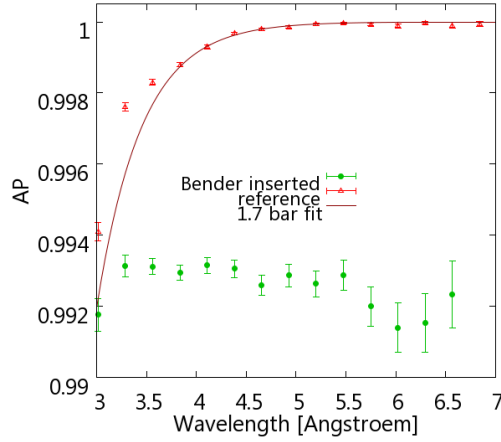


Figure 4.28:  $AP$  comparison of a neutron beam analyzed and polarized by opaque helium cells with and without a bender in-between.

of several times  $10^{-3}$  are visible. The resulting polarization is practically independent of the wavelength in the range shown from 3 to 7 Å. This is in agreement with the depolarization described in the two preceding sections, Sec. 4.2.3 and Sec. 4.2.4. Depolarization in this order of magnitude makes the bender with the current settings not suitable for polarization on the  $10^{-4}$  level. This results furthermore directly confirms suspicions that the crossed X-SM geometry did not perform as well as expected due to depolarization in the second bender in this order of magnitude [26].

### 4.2.7 Summary

In the previous sections, the depolarization in polarizing supermirrors was found to be mainly due to misaligned magnetic domains and has been studied in detail. Depolarization was found to be up to  $\sim 10^{-2}$  for a single reflection. In Tab. 4.4, a qualitative summary of all the parameters studied is given with the most beneficial condition to minimize the depolarization. The quantitative range for the parameters will of course be influenced by constraints and conditions of the actual experiment. The table gives indications such that the optimum choice for a given parameter space can be made. The most influential parameter is the magnetizing field. In the set-up presented in this thesis, it was varied from the typical 0.03 T that is used in polarizing benders to 0.82 T. This is the range for "high" and "low" field.

Parameter	beneficial setting to minimize depolarization
Magnetizing field	high (0.8 T)
supermirror factor $m$	small
incidence angle	small
wavelength	short
CoTi	low field
FeSi	high field
polarize by reflection	high field
polarize by transmission	low field

Table 4.4: Summary of the studied parameters influencing depolarization in polarizing supermirrors.

It is important to stress while all the other parameters certainly influence depolarization, the magnetizing field is the dominant factor. The influence from the other parameters is more important at low field, it vanishes at maximum field.

### 4.3 Depolarization By Beamline Elements

In order to guarantee a high and constant polarization, beamline components in contact with the neutron beam after the polarizing component should not alter the neutron polarization. Two components were tested: A spin flipper, where the conservation of polarization is a particularly sensible matter as it acts on the neutron spin directly and an Aluminium flange window as the neutrons would encounter when entering and exiting a vacuum chamber. The set-up is based on the OTB with the wavelength-resolved set-up from Sec. 4.1, where the beamline component is put between the two cells.

#### 4.3.1 Aluminium Window

Given that many experiments are operated under vacuum conditions, neutrons need to enter these vacuum-tight entities through an Al-layer. An Al-flange that had been used in the PERKEO experiment [16] was tested by being inserted between the two magic boxes. No additional guide field was necessary due to the short distance between the boxes. In the case of the Al window, simply the polarization after the window was measured. Fig. 4.29 reports the polarization over wavelength as well as the polarization of the

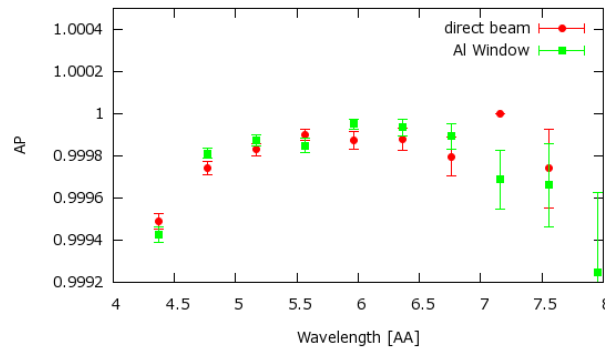


Figure 4.29: Wavelength resolved product of Analyzing and Polarizing power of two opaque helium cells at 1.4 bar with and without a aluminum window between them.

beam without the Al present of two measurements taken immediately one after the other. The Al window does not depolarize the beam within the experimental sensitivity of the OTB.

### 4.3.2 Flipper

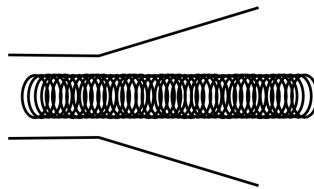


Figure 4.30: "Croccodile" spin flipper, an RF fast adiabatic spin flipper. The holding field is generated through the plates, a slight field gradient is induced due to the growing distance between the plates. The perpendicular RF-field is applied via the coil.

While typically beamline components only act passively on the neutron polarization, the spin flipper is intended to invert the polarization. Hence, in order to measure the spin flip inefficiency that characterizes a spin flipper, a further configuration is added to the measurement scheme, see Tab. 6.1. In this additional, black, configuration  $N_b2$ , the cell polarizations remain parallel and the flipper is turned on. Neutrons detected are thus due to incomplete spin flipping. The spin flipper efficiency  $f$  (Eqn. 3.17) can be

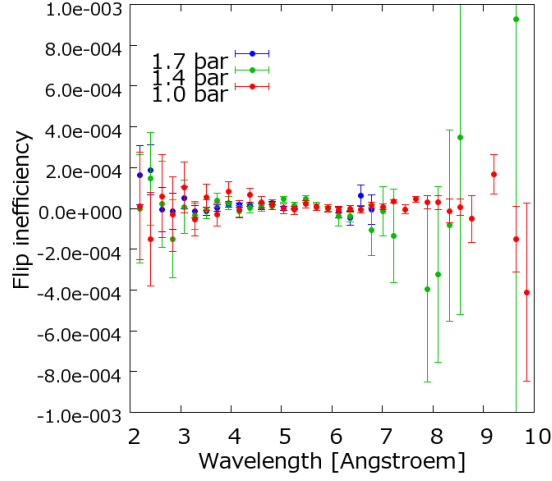


Figure 4.31: Flipping inefficiency  $\epsilon$  for a RF-Flipper measured with helium cell batches of different opacities.

count rate	polarizer cell	flipper	analyzer cell	configuration
$N_w$	UP	OFF	UP	white
$N_b$	UP	OFF	DOWN	black
$N_{b2}$	UP	ON	UP	black

Table 4.5: Measurement configurations for the spin flipper in the OTB.

expressed in term of the count rate as:

$$1 - 2\epsilon = \frac{N_w - N_b}{N_w - N_{b2}} \quad (4.3)$$

The flipper tested is an adiabatic RF-flipper called "Crocodile-flipper". It is composed by an RF-coil and two parallel plates that create the holding field. The plates are having a V-shaped form at the end in order to vary the holding field. A sketch is shown in Fig. 4.30. The inefficiency  $\epsilon$  is reported in Fig. 4.31 as a function of the wavelength. The inefficiency is below  $10^{-4}$  in the range of 4 to 8 Å, the sensitive range of the OTB. The inefficiencies  $\epsilon$  with their Gaussian uncertainties  $\sigma_\epsilon$  shown in Fig. 4.31 are sometimes negative. This is mathematically possible from the way it has been determined, Eqn. (4.3). However, physically it is impossible to have a flipper with negative inefficiency, the inefficiency in the extreme case of the perfect flipper being 0. Therefore, the confidence intervals have to be



wavelength[Å]	$\epsilon$	$\sigma_\epsilon$	$\epsilon_{\min}$	$\epsilon_{\max}$
3.12-4.15	$2.3 \cdot 10^{-5}$	$3 \cdot 10^{-5}$	$4.5 \cdot 10^{-6}$	$5.4 \cdot 10^{-5}$
4.16-5.19	$2.3 \cdot 10^{-5}$	$1.5 \cdot 10^{-5}$	$7.8 \cdot 10^{-6}$	$3.8 \cdot 10^{-5}$
5.2-6.23	$3.0 \cdot 10^{-6}$	$9 \cdot 10^{-6}$	0	$1.17 \cdot 10^{-5}$
6.24-7.27	$3.0 \cdot 10^{-6}$	$8 \cdot 10^{-6}$	0	$1.1 \cdot 10^{-5}$

Table 4.6: Averaged flip efficiency interval  $[\epsilon_{\min}, \epsilon_{\max}]$  with confidence level 68.27% according to [70]. Measured with 1.0 bar cell batch.

adjusted to take into account these physical realities, leading to asymmetric errorbars. Below, the averaged inefficiency per wavelength is reported for the three different opacities with their interval corresponding to a 68.27% , which is the common confidence level used for symmetric cases  $[\epsilon - \sigma_\epsilon, \epsilon + \sigma_\epsilon]$ [70].

wavelength[Å]	$\epsilon$	$\sigma_\epsilon$	$\epsilon_{\min}$	$\epsilon_{\max}$
3.12-4.15	$1.5 \cdot 10^{-5}$	$2.2 \cdot 10^{-5}$	$2.4 \cdot 10^{-6}$	$3.7 \cdot 10^{-5}$
4.16-5.19	$2.0 \cdot 10^{-6}$	$21.2 \cdot 10^{-5}$	0	$1.4 \cdot 10^{-5}$
5.2-6.23	$2.8 \cdot 10^{-5}$	$1.0 \cdot 10^{-5}$	$1.8 \cdot 10^{-5}$	$3.8 \cdot 10^{-5}$
6.24-7.27	$-4.9 \cdot 10^{-5}$	$4.0 \cdot 10^{-5}$	0	$8.0 \cdot 10^{-6}$

Table 4.7: Averaged flip efficiency interval  $[\epsilon_{\min}, \epsilon_{\max}]$  with confidence level 68.27% according to [70]. Measured with 1.4 bar cell batch.

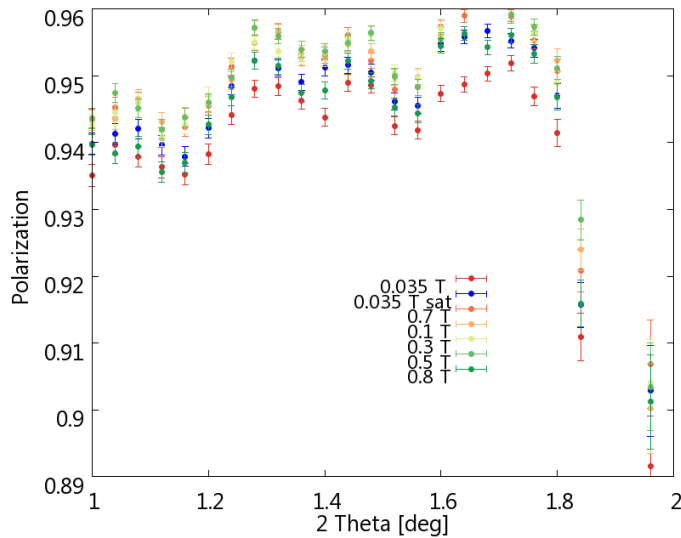
wavelength[Å]	$\epsilon$	$\sigma_\epsilon$	$\epsilon_{\min}$	$\epsilon_{\max}$
3.12-4.15	$2.0 \cdot 10^{-6}$	$9 \cdot 10^{-6}$	0	$1.1 \cdot 10^{-5}$
4.16-5.19	$1.5 \cdot 10^{-5}$	$5 \cdot 10^{-6}$	$1.0 \cdot 10^{-5}$	$2.0 \cdot 10^{-5}$
5.2-6.23	$2.5 \cdot 10^{-5}$	$7 \cdot 10^{-6}$	$1.8 \cdot 10^{-5}$	$3.2 \cdot 10^{-5}$
6.24-7.27	$-1.4 \cdot 10^{-5}$	$4.3 \cdot 10^{-5}$	0	$3.0 \cdot 10^{-5}$

Table 4.8: Averaged flip efficiency interval  $[\epsilon_{\min}, \epsilon_{\max}]$  with confidence level 68.27% according to [70]. Measured with 1.7 bar cell batch.

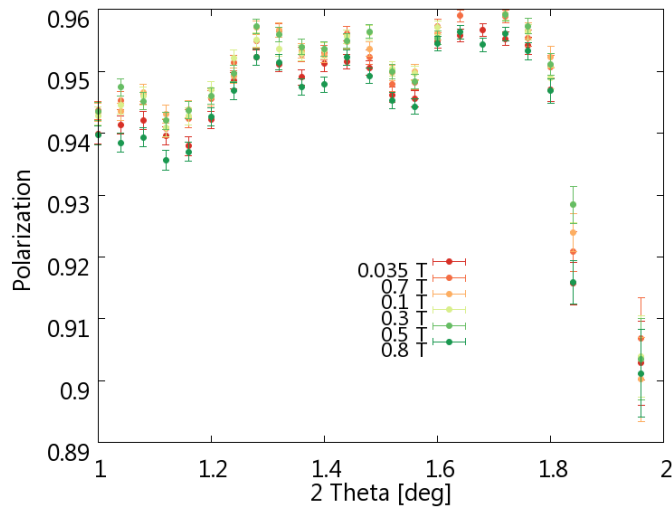
Consequently, the described flipper has an efficiency  $> 0.9999$  between 4 to 8 Å. This is sufficient for the next generation of neutron decay experiments.

## 4.4 Single Polarizing Supermirrors

In Sec. 4.2, it was shown that the depolarization in polarizing supermirrors can be suppressed via high magnetizing fields in the order of 1 Tesla. In this section, the polarizing power measured for a single reflection on supermirrors



(a)



(b)

Figure 4.32: Polarizing power of the specular reflection as a function of the scattering angle  $2\theta$  angle in the polarizing range for a  $m=2.0$  supermirror at different magnetic fields (a) CoTi (b) FeSi

with  $m=2.0$  for CoTi and FeSi are reported. The supermirror samples were placed in a magnetizing field that could be varied. The measurement was performed on the SuperADAM instrument at ILL.

The supermirror samples were placed inside an electro-magnet for mag-

sample	0.1 Tesla		0.8 Tesla	
	polarization	error	polarization	error
CoTi m=2.0	0.98262	$4.2 \cdot 10^{-4}$	0.988185	$3.0 \cdot 10^{-4}$
CoTi m=2.8	0.96943	$7.3 \cdot 10^{-4}$	0.98374	$4.1 \cdot 10^{-4}$
FeSi m=2.0	0.97304	$6.4 \cdot 10^{-4}$		
FeSi m=3.8	0.97596	$5.1 \cdot 10^{-4}$	0.991183	$2.1 \cdot 10^{-4}$

Table 4.9: Polarizing power for different supermirrors measured with an opaque helium cell ( theoretical analyzing power of 0.99999) measured at 5.3 Å

netization. In Fig. 4.32, the polarizing power for both mirror is reported as function of the scattering angle: The specular component has been measured for a magnetizing field varying between 0.035 T and 0.8 T for both mirrors. The mirrors' performance increases with an increasing field. However, this increase is not continuous: The maximum field of 0.8 T is not the maximum of mirror performance. The mirrors perform better at about 0.5 T.

Similarly, the mirrors performance has been tested with a highly opaque helium set-up on the OTB, details in Sec. 4.1 and 4.2.2 with constant incident angle and a varying magnetizing field. These measurements confirm a higher polarization reached for a high magnetizing field, see Tab. 4.9.

In both instruments, the polarizing power increases by a few percent when comparing minimum and maximum magnetizing field. The reached polarization power of this single reflection is higher, but not sufficient for application in a high precision neutron decay experiment.

In addition, the hysteresis of the polarizing power was investigated for a CoTi mirror: Fig. 4.32(a) shows the polarizing power of a CoTi m=2.0 supermirror at 0.035 Tesla, maximum 0.8 Tesla and a 180 deg physical turn of the mirror, remeasured at 0.035 Tesla ("0.035 sat"). The performance of the latter closely follows the one at maximum field, while the first measurement at minimum field is lower. We suspect a better alignment of the domains to be the reason for this better performance at low field in agreement with the results from the depolarization measurement.

In conclusion, it is advisable to expose mirrors to high fields before building a polarizing device, especially if the device is operated at low magnetizing fields.

## 4.5 Polarizing Supermirrors In Crossed Geometry

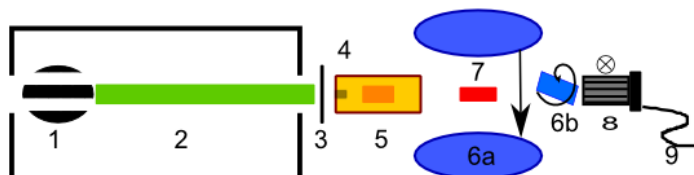


Figure 4.33: Set-up for a crossed supermirror geometry (1) Velocity selector (2) Neutron guide (3) Shutter (4) Beryllium filter (5) Polarization by an opaque helium cell (6a) Electro-magnet (6b) Guide field for adiabatic field turn (7) Sample Supermirror (1st reflection) (8) inclined CoTi Bender (9) Detector

In this section, measurement results for a crossed X-SM geometry [26] are presented. It has been shown in the previous sections (Sec. 4.2, Sec. 4.4) that in a high magnetic field, polarizing power increases and that depolarization is largely suppressed. While the increase magnetizing field is does not lead to sufficient polarizing power in simple reflection, these results can be applied to the crossed crossed geometry, where polarizing inefficiencies enter only quadratically (Sec. 3.3.3) into the performance. The beam preparation was identical to Sec. 4.2.2: a continuous  $5.3 \text{ \AA}$  beam having a cross section of ca  $1 \text{ mm} \times 40 \text{ mm}$ . The set-up involved a polarizing helium cell and crossed X-SM geometry for analysis, see Fig. 4.33. The defining last reflection when using the X-SM geometry as a polarizer [26] is inverted in this set-up to the first reflection in the analyzer. The first reflection on a mirror occurred on a single mirror placed in an electro-magnet with variable field. The field direction was then adiabatically turned by 90 degrees perpendicular to the flight direction. This was realized via a tilted guiding field section constructed from permanent magnets. The guiding field was about 40 Gauss. The second and further reflections take place in a common CoTi-Bender with constant magnetizing field. The magnetizing field on the first mirror can be varied and thus vary the depolarization of the beam in this first reflection. relatively low supermirror factor  $m$  was chosen as depolarization is lowest, see Sec. 4.2.4.

Fig. 4.34 reports the combined analysis and polarization power product  $A \cdot P$  measured where the single mirror was a FeSi  $m=2$  mirror and a CoTi

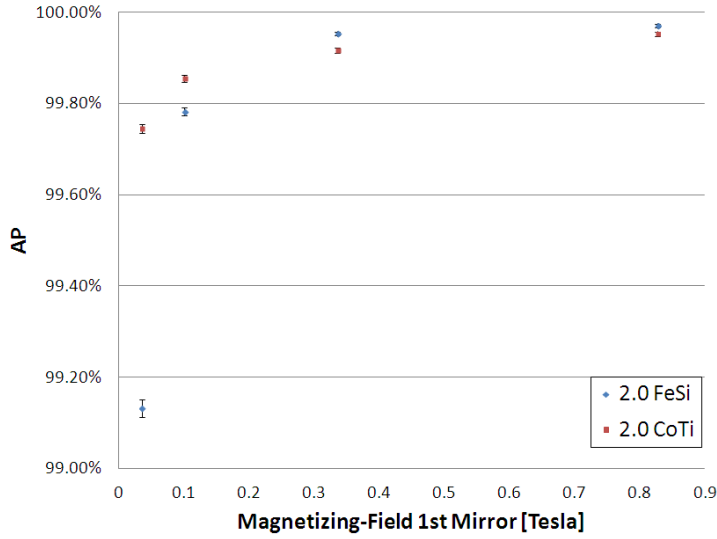


Figure 4.34: Analysis by a X-SM geometry with a CoTi bender and a CoTi or FeSi  $m=2.0$  supermirror in function of its magnetizing field. Polarization by a highly opaque helium cell.

$m=2$  mirror. Both combinations increase performance with an increased magnetizing field in the first mirror, as the depolarization by it is lowered accordingly. In agreement with results from 4.2.4, CoTi performs better at low field and FeSi better at higher fields. The maximum polarization reached with this set-up is  $AP=0.99970(3)$ . This experiment shows that the unexpectedly low performance in [26] is due to depolarization in the bender and furthermore shows that this can be overcome with an increased magnetizing field. The results for the crossed geometry [26] are increased by an order of magnitude. This makes a polarization system that bases purely on supermirrors competitive for neutron polarization on the  $10^{-4}$  level.

The measurement has been performed for a wavelength band that is realistic for the PERC set-up, a  $5.3 \text{ \AA}$  beam with  $\frac{\Delta\lambda}{\lambda} \sim 10\%$ . For an application to a large beam cross section typical for neutron decay experiments, the first single mirror would be replaced by another bender. There is loss of flux to be expected equally from both benders, as they confine the beam in perpendicular directions. Counting with a flux loss of 0.5 for each bender due to geometry plus the flux loss due to polarization, the transmission of such a geometry is around 12.5%.

# 5

## PERC beamline

PERC will be built in Garching at the FRM II reactor. A high flux neutron beam of cold neutrons is guided from the reactor via a primary guide to the East Hall where PERC is going to be installed, see Fig. 5.1. This chapter is dedicated to investigations in this beamline. Sec. 5.1 shows simulations carried out in order to optimize the coating of the primary guide to achieve a high, homogenous flux. Sec. 5.2 discusses the possibility of a high-intensity, pulsed neutron source for PERC.

The primary guide is bent with a curvature radius of 3 km to avoid contamination of the beam with fast neutrons and gammas. The direct sight ends two meters before the end of the guide. The guide will be coated with a NiTi  $m=2.5$  supermirror. The decision of this supermirror factor is based on simulations that will be presented in the next section.

In Fig. 5.2, the details of the PERC beamline after the primary guide are given. An aperture reduces the beam to the  $6 \text{ cm} \times 6 \text{ cm}$  cross section. Just before entering the building, a Dornier velocity selector [71] is placed, selecting neutrons around  $5 \text{ \AA}$  with a resolution of  $\frac{\Delta\lambda}{\lambda} = 11\%$ . The technical data for the selector purchased for PERC are listed in Tab. 5.1. The position of the selector in front of the building wall reduces background at the detector

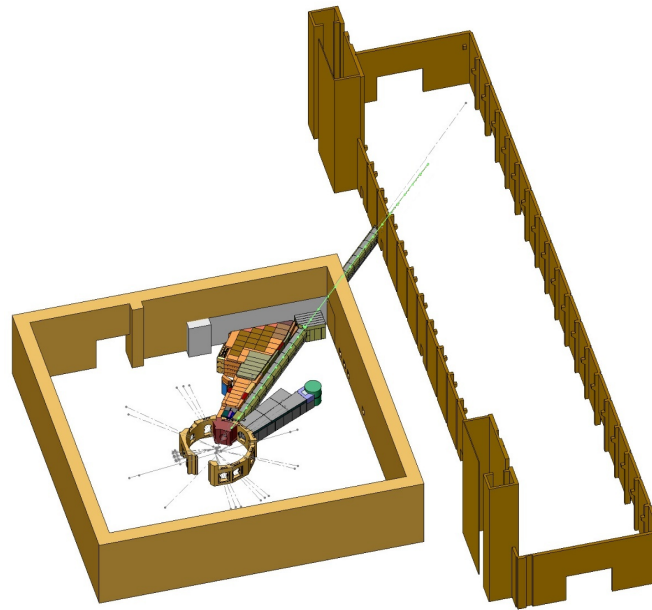


Figure 5.1: The new MEPHISTO guide connecting the reactor and the East Hall, picture courtesy of J. Klenke.

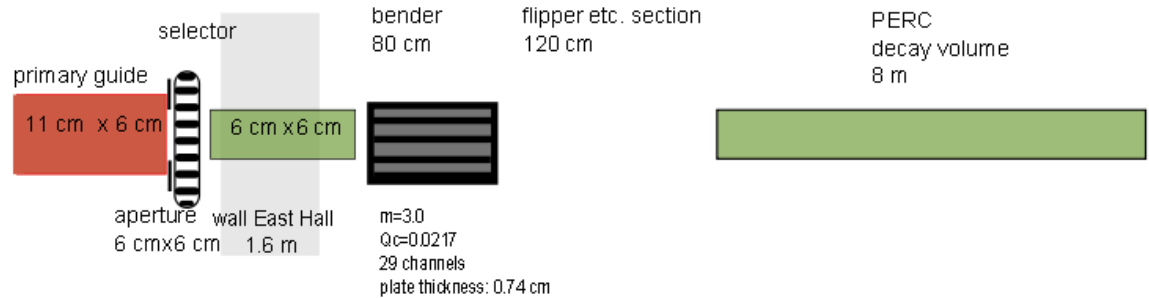


Figure 5.2: Set-up of the PERC beamline as used in simulations. The selector is set to 5 Å.

blade length	250 mm
blade width	0.4 mm
number of blades	72
torsion angle	48.27 deg
frequency	424 Hz
window width	150 mm
window height	65 mm
total length of selector	400 mm

Table 5.1: Technical data Dornier selector [71] at 5 Å.

area of PERC. A rectangular, straight  $6\text{ cm} \times 6\text{ cm}$  guide of 1.6 m length cuts transversely through the wall of the East Hall. It is followed inside the hall by the polarization system. Its detailed geometry has yet to be determined, for propositions and indications see results from this thesis, Sec. 6.1. Before entering the actual decay volume after polarization, a spin flipper and possibly a chopper are placed. In addition, space is needed to adiabatically turn the neutron polarization, created perpendicular to the flight direction in the polarizing unit, parallel to the longitudinal B-field in the decay volume without polarization loss. In total, the distance between the wall and the beginning of the decay volume is estimated to about 2 m. The decay volume is a 8 m long  $6\text{ cm} \times 6\text{ cm}$  rectangular guide. It is going to be built of segments of maximum 2 m length. To this date, the supermirror factor of the non-depolarizing PERC guide forming the decay volume is not definitely defined. However,  $m=2.0$  is estimated to be achievable [72].

## 5.1 Optimization Of The Primary Guide Coating

The primary guide (MEPHISTO) was optimized for the PERC instrument. In this section, the goals of the optimization, the simulation method and the results are presented.

### 5.1.1 Simulation Method: McStas

The simulations on the neutron beam in this work were carried out by the McStas code[73]. It is a meta-language that allows for easy, versatile assembling of the different components on a beamline. It is based on a Monte Carlo method written in C. Monte Carlo methods rely on the Central Limit Theorem wherein the sum of a realization of a function on a surface converges to the integral of a function over a surface. For a code simulating the behavior of a neutron beam, this means practically that a large number of neutrons is generated and put through a beamline, taking into account possible absorption, reflection and transmission of a beam. At the end, the number of neutrons coming through indicates the neutron flux (integral over the before mentioned parameters taking into account initial energy and divergence distribution). With McStas, a "Pseudo" Monte Carlo code, the calculation process is significantly accelerated by attributing each neutron a weight that indicates the probability of the neutron's existence at this place



and moment. Hence, the weight is adjusted after each component the neutron has encountered. Simulation also allows for microscopic effects to be taken into account, such as surface roughness, that are difficult to realistically calculate analytically[73, p.25-31 ].

The simulations presented were carried out using McStas, version 1.12b. Gravity was not considered and the neutrons are unpolarized. The simulations do not take into account Al flanges that would need to be traversed at several times on the journey from the reactor to the beamstop.

### 5.1.2 Beamline Set-Up

The primary guide is fed by a cold source and connected to it by a "insert" unit. This unit has already been installed in the reactor building. The insert is coated with a supermirror factor of approximately  $m=3.2$ . The MEPHISTO guide (primary guide) is 38 meter long and bent with a curvature radius of 3000 m. In the simulation, it is cut into 2 meter long straight pieces which are rotated by a small angle relative to each other. The guide is 60 mm wide and 110 mm high, the McStas component used is the 'wavy\_guide' (no gravity). The primary guide ends close to the wall of the East Hall.

By default, the selector is included in most simulations. This implies in particular that most of the comparison and optimization carried out is done for the wavelength of 5 Å only if not mentioned otherwise. Transmission through the selector for 5 Å is of about 67% for the divergence present coming from a MEPHISTO guide coated with  $m=2.5$ . Simulation of the selector does not take into account transmission of neutrons with small wavelengths. Such transmission are due to weaker absorption in the selector for small wavelength. The technical data of the selector suggests a suppression of thermal neutrons  $< 5 \cdot 10^4$  when working at wavelength 4.5 Å. The blades are boron coated. To further suppress these wavelengths, one could insert a beryllium filter in front of the selector which effectively reduces the intensity below 4 Å, as shown in Sec. 4.1.

The supermirror factor for the guide leading through the East Hall wall is identical to PERC. For the polarizer, given that the exact geometry of the polarizing unit is not fixed yet, a simple bender is assumed. As the simulations are made for unpolarized neutrons, the bender unit simply changes the direction and distribution of the beam. The technical data of this bender

correspond mainly to the polarizer of PF1b, characterized in [74], repeated in table 5.2 for the specific case of these calculations. Note that  $m=3.0$  is used whereas the PF1b bender consists of supermirrors with  $m=2.8$ .

width	80 mm
height	80 mm
Glass thickness	0.74 mm
number of channels	29
supermirror factor	$m=3.0$

Table 5.2: Technical data bender from [74]

After the bender, 1.2 meter are simulated as "free flight" until the beginning of the actual PERC guide. This space is needed for a possible spin flipper and electron detection which should not influence the neutrons' flight path. The simulations are carried out for a continuous beam.

The interest of the simulations was to look at the development of the flux in the decay volume of PERC. To observe the development of neutron flux in PERC, the guide (component: 'guide\_wavy') was cut into 8 pieces, each 999 mm long, and separated by 1 mm from each other. The 1 mm slot is used to put McStas monitors. Gaps needed for pumping or probing the neutron flux at different points in the decay volume are not included in the simulation. An example of McStas components that build the PERC beamline is given in Annex B, not including monitors. To observe absorption in the neutron guide it-self, a new component for McStas has been written called "Guide\_wavy\_loss\_ck\_binningdiv.com ". It allows to track absorbed neutron intensity in a guide in function of the z-coordinate, the wavelength, x and y divergence. It is thus a good tool to provide close studies of the absorption phenomena itself. However, it cannot track the flux along the complete guide. For this reason, general comparisons are better done when sticking with the straight-forward cutting into 1-meter pieces of the guide.

### 5.1.3 Supermirror Coatings Of The Primary Guide

For the  $m$ -value of the primary guide, several options for coatings were investigated. The goal was to have a high, constant flux through out the decay volume of PERC. High flux is desired for statistics, but more importantly, a small flux gradient with minimum loss is advantageous for systematic reasons: Minimum loss implies minimum background creation due to neutrons

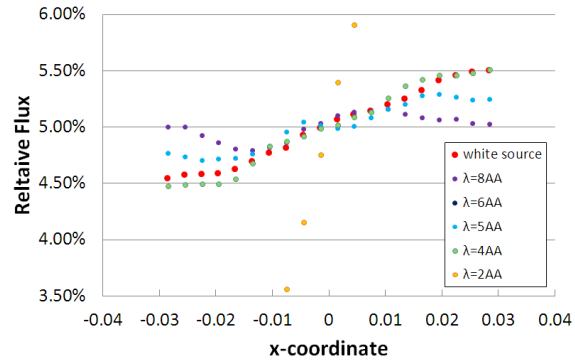


Figure 5.3: Horizontal cut through the beam profile at the end of the primary guide. Data for  $m=1.5$  in the primary guide.

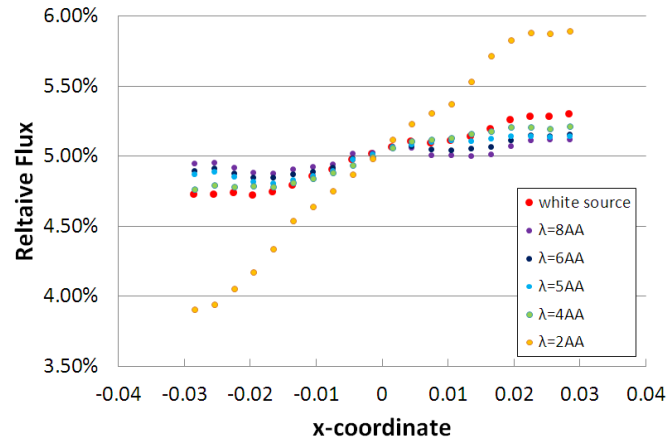


Figure 5.4: Horizontal cut through the beam profile at the end of the primary guide. Data for  $m=2.5$  in the primary guide.

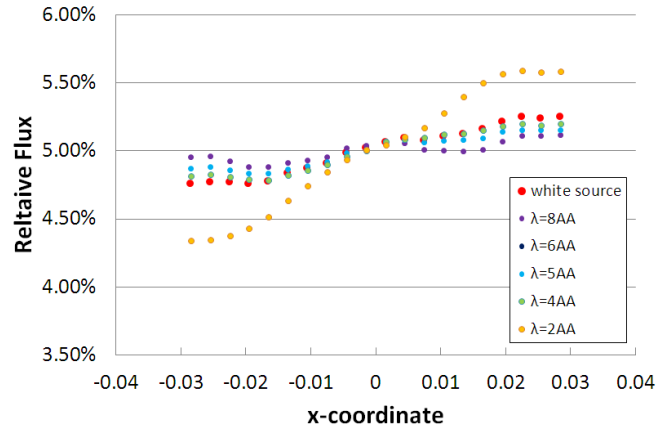


Figure 5.5: Horizontal cut through the beam profile at the end of the primary guide. Data for  $m=3.2$  in the primary guide.

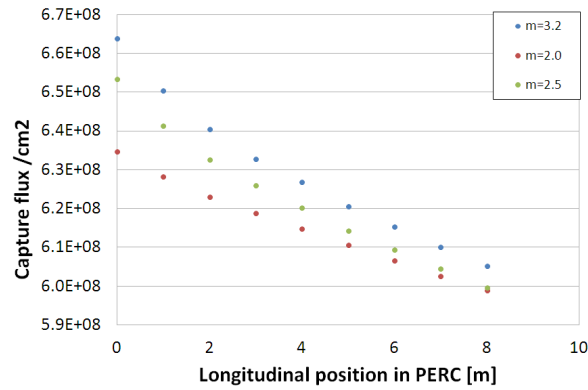


Figure 5.6: capture flux gradient in PERC for different supermirror factors of the primary guide, PERC guide :  $m=2.0$

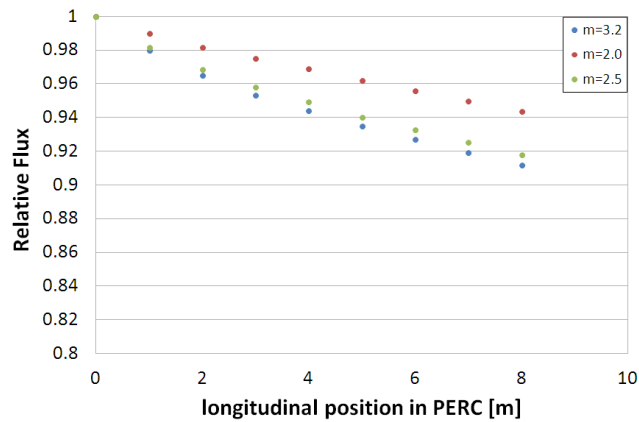


Figure 5.7: Flux gradient (relative change) in PERC for different supermirror factors of the primary guide, PERC guide:  $m=2.0$

and furthermore, corrections on the magnetic mirror effect are more easily made.

Reflectivity curves ranging from  $m=1.5$  to  $m=3.2$  based on fits of reflectivity curves of mirrors produced at FRMII and SwissNeutronics were provided by Jens Klenke from FRMII [75]. When comparing this horizontal cut for different supermirror factors of the MEPHISTO guide, the discrepancy between the left and right correlates with the supermirror factor, as the cut-off angle for the Garland reflections is determined by the coating. Horizontal cuts for  $m=1.5$  and  $m=3.2$  can be found in Fig. 5.3, 5.4, 5.5. Fig. 5.6 and 5.7 give a picture of the capture flux gradient along PERC for supermirror factors of  $m=2.0$ ,  $m=2.5$  and  $m=3.2$ , the coating for the decay volume of PERC is  $m=2.0$  for all cases. The main part of the flux loss takes place in the first few meters of the decay volume. The loss is, as expected, less for low supermirror factor  $m=2.0$  but in the same order as for  $m=2.5$  where 8 % of flux get lost in PERC. The change of height and width between the MEPHISTO and the PERC guide also plays a role in how and which divergences do get absorbed. In the example of a 60 mm x110 mm primary guide and a 60 mm x60 mm cross section of the decay volume, simply the change of height provides an absorption and when combined with a change of the supermirror factor, an asymmetry in the absorption pattern is manifest: While in the x-direction, mostly neutrons with high divergences get absorbed, in the y direction the highest intensity absorbed is observed for low divergent neutrons due to the

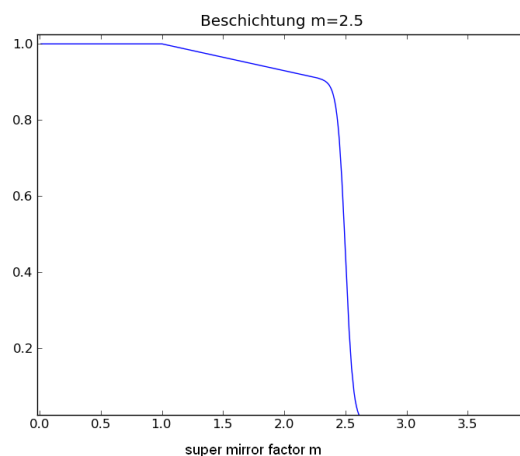


Figure 5.8: Reflectivity curve of a  $m=2.5$  guide.

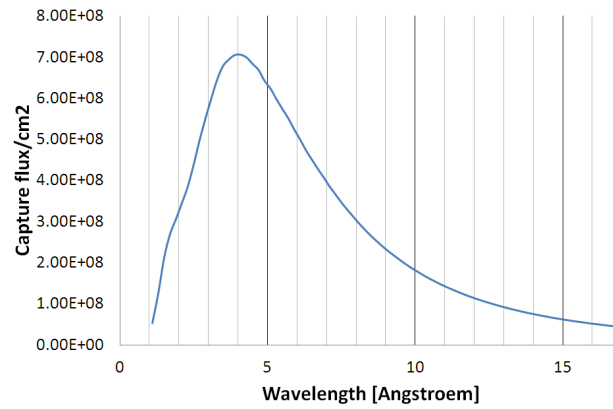
reduction of the beam height.

The difference in coating between the primary guide and PERC defines most of the flux gradient in PERC. At the general PERC collaboration meeting on November 29, 2010 it was decided to take  $m=2.5$ . A measured supermirror factor curve used for the simulations is provided by C. Breunig from the FRMII Neutron Optics Group, see Fig. 5.8. While a smaller difference between the coating and the PERC guide would have a smaller flux gradient in the decay volume, this choice makes it possible to accommodate for PERC guide coatings up to  $m=2.5$ .

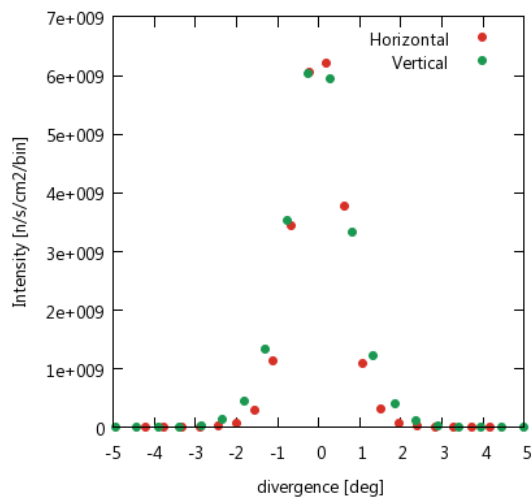
#### 5.1.4 Beam Characterization At The End Of The Primary Guide

In this section, the beam provided by a  $m=2.5$  coated primary guide is presented.

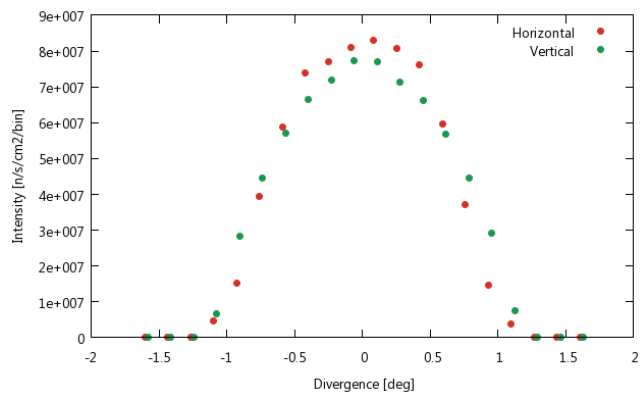
The simulated spectrum for is shown in Fig. 5.9. In addition, the divergence is also shown. As expected, the transported vertical divergence is higher than the horizontal one as the height of the guide is 11 cm compared to a width of 6 cm. After the bender, which changes the divergence in both cases in addition to the fact that the height of the beam was also reduced to 6 cm, the divergence is lower in both cases. The maximum divergence of



(a)



(b)



(c)

Figure 5.9: (a) The spectrum of at the end of the primary guide, simulated with a  $m=2.5$  coating . (b) Horizontal and vertical divergence at the end of the primary guide, simulated for a  $m=2.5$  coating. (c) Horizontal and vertical divergence at the entry of the decay volume, simulated for a  $m=2.5$  coating of the primary guide.

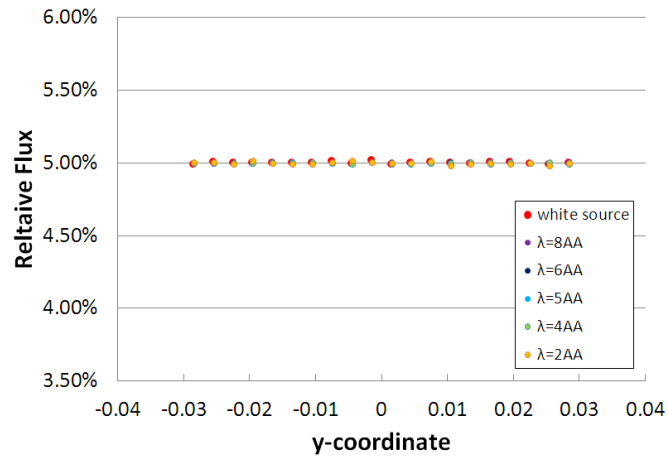


Figure 5.10: vertical cut through the beam profile at the end of the primary guide. Data for  $m=2.5$  in the primary guide.

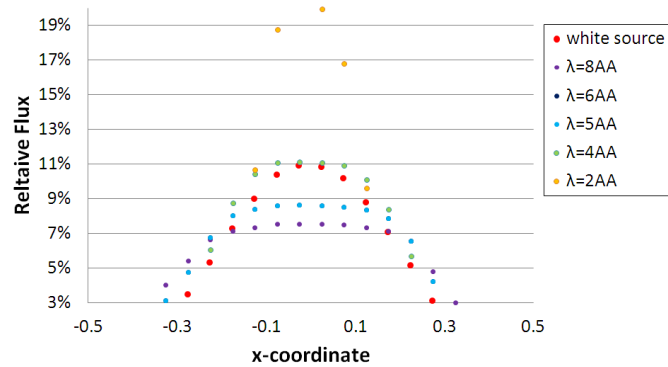


Figure 5.11: Horizontal cut of the simulated flux distribution along the x-axis at a distance 20 meters from the end of the primary guide.



1.3 degrees would lead to 4 reflections in the decay volume. When looking at the flux distribution in horizontal (x) and vertical (y) direction at the end of the primary guide, the following observations can be made:

- in the *vertical* direction, there is no significant variation in distribution as shown in Fig. 5.10.
- on the *horizontal* axis however, a clear asymmetry is visible in Fig. 5.4 which is due to the curvature of the guide. Due to Garland reflections, the intensity on the right side (outer side of the guide) is higher than on the left side. However, the longer the wavelength gets, the smaller the discrepancy between the two sides gets. For 2 Å, the ratio between minimal and maximal flux is 0.775, for 5 Å it is 0.939.
- When setting monitors at 20 meters distance from the end of the last MEPHISTO guide piece (Fig. 5.11), the center of the beam is still in tangential direction. It is therefore justified to set PERC tangential to the last primary guide segment.

### 5.1.5 Coating Of The PERC Guide

This section discusses the coating of the decay volume, the PERC guide and the contrast between the primary guide and the PERC guide coating.

The working assumption for the coating of the decay volume is a supermirror factor of  $m=2.0$ . Initial simulations were carried out for  $m=1.5$ . For this lower supermirror factor, some effects linked to the change in supermirror factors between the MEPHISTO guide and the decay volume are enhanced as the change is bigger.

The general picture concerning the supermirror factor in the primary guide remains the same, however the losses are higher than in the case of  $m=2.0$  for PERC and the differences between the supermirror factors in the primary guide are much more distinct. However, one notes that the gradient in PERC does have a much more distinct shape when compared to  $m=2.0$ , as it is shown in Fig. 5.6 for a primary guide supermirror factor of  $m=2.5$ . The absorption of neutrons in the guide wall is high on the first 3 to 4 meters and then goes into an area of lower absorption and thus a less steep flux gradient.

In conclusion: A too steep flux gradient in or immediately before PERC should be avoided to not unnecessarily produce background and furthermore

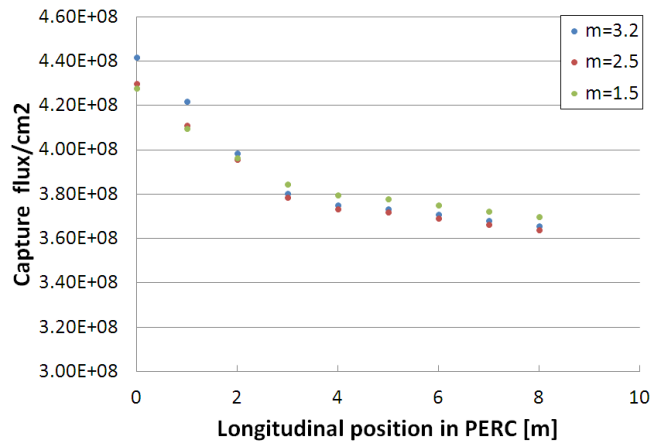


Figure 5.12: For a supermirror factor of  $m=1.5$  in PERC a comparison of different supermirror factors for the primary guide in terms of the capture flux in PERC.

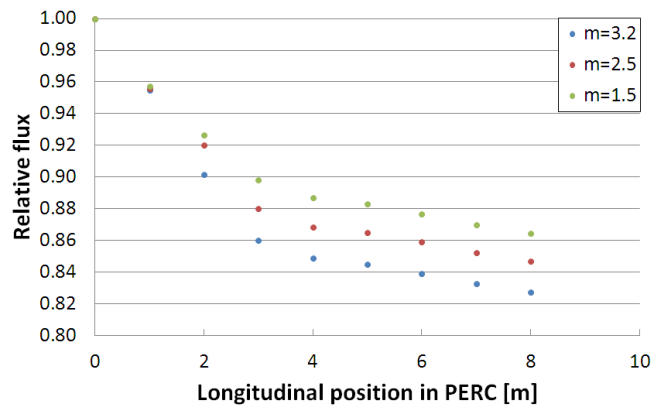


Figure 5.13: For a supermirror factor of  $m=1.5$  in PERC a comparison of different supermirror factors for the primary guide in terms of the flux through PERC relative to the initial flux at the PERC entry.

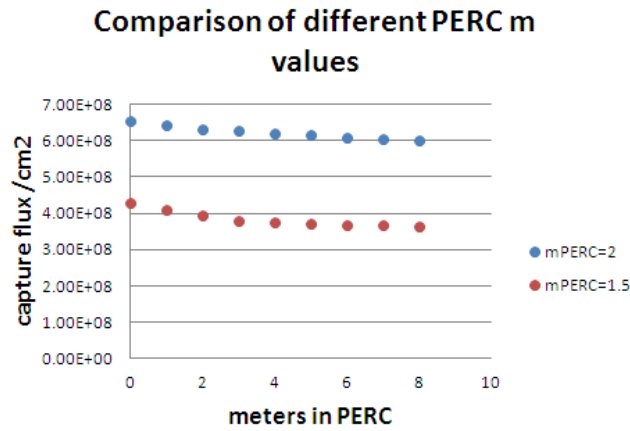


Figure 5.14: For a primary guide of  $m=2.5$ , the flux gradient in PERC for coatings  $m=2.0$  and  $1.5$ . They do not start at the same value because already the guide through the East Hall wall is coated with PERC's supermirror factor.

to minimize corrections necessary due to the magnetic mirror effects. These are the reasons why the guide element(s) between the primary guide and PERC are a) already at the same cross section as PERC and b) have the same coating. This effectively shifts the gradient due to the change in aperture and coating away from PERC towards the primary guide. This idea could be extended by even coating the last pieces of the primary guide with a supermirror factor similar to PERC. This is schematically shown in Fig. 5.15.

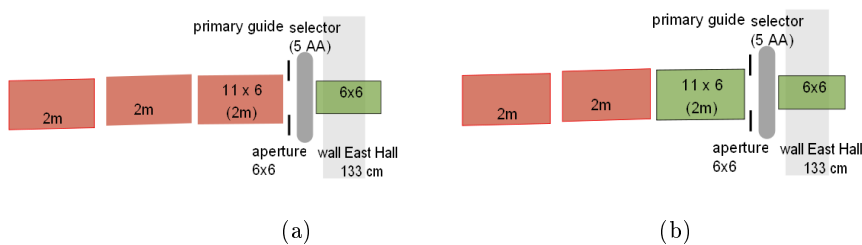


Figure 5.15: Set-up of the beamline between the last two primary guide segments and the guide through the East Hall wall (a) original (b) modified set up, using the supermirror factor of the PERC guide for the last guide piece of the primary guide

## 5.2 PERC At ESS

The European Spallation Source ESS will be the new European neutron user facility, planned to start operation in 2019. It creates a neutron flux via accelerated protons that hit on a heavy metal target. The proton beam is pulsed, which generates a time structure inherent to the neutron beam. The peak flux is supposed to be 30 times higher than the continuous flux of today's most powerful neutron source, the ILL reactor[76].

$$\phi_{0,ESS}(\lambda) = 30 \cdot \phi_{0,ILL}(\lambda) \quad (5.1)$$

The flux FRM II reactor is comparable to the one of the ILL reactor. ESS' most prominent feature is the time structure of its highly intense flux. Chopping the beam that travels through PERC would allow for a more precise correction of the magnetic mirror effect ([16, 77]) and background analysis could possibly profit from a non-continuous beam. A pulsed mode for PERC is planned with a chopper right in front of the decay volume. This section of the beamline chapter analytically discusses the optimum beamline parameters for operating PERC in a pulsed mode at both a continuous and pulsed source, comparing the time-averaged flux. This is an extended version of [78].

For this comparison, the important part of the beamline is the chopper

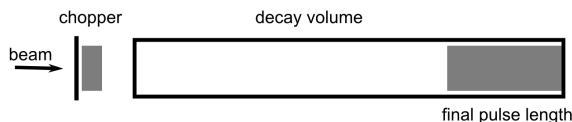


Figure 5.16: Chopper in front of PERC for pulsed mode. The pulse dilates spatially while traveling through the decay volume. Distance between chopper and decay volume exaggerated for

right in front of PERC and the decay volume itself, see Fig 5.16. On its path through the decay volume, the neutron pulse will spatially extend provided it contains different wavelengths. For an effective control on the systematics in the pulsed mode, the final pulse length should not be too large. A conservative assumption is to limit the final pulse length to  $p = 2$  m which is the length the guide modules in PERC will have. Furthermore, it is important that only one pulse at a time is in the decay volume. To

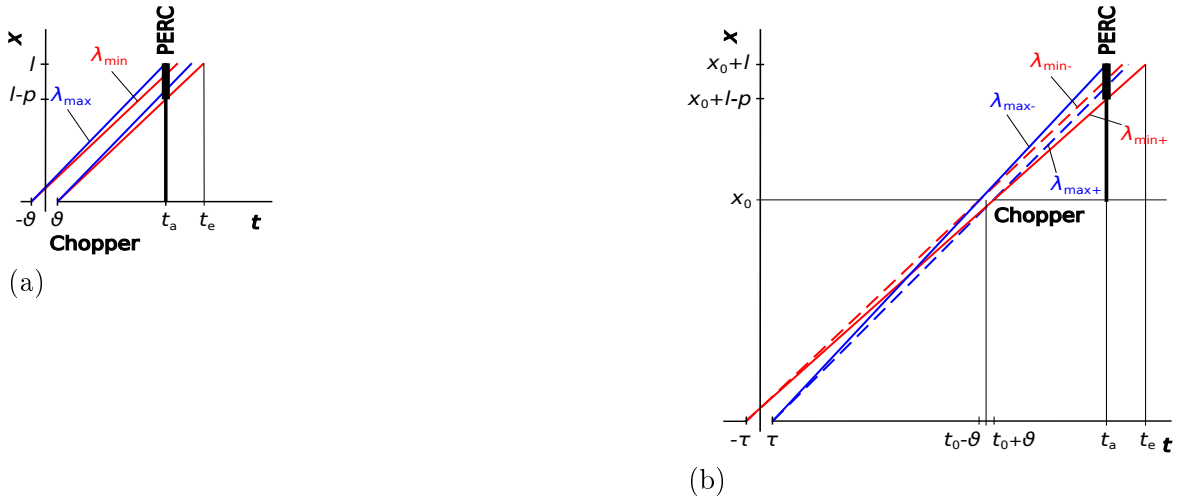


Figure 5.17: (a) Space-time-diagrams for a continuous source. At each moment, the full wavelength band  $(\lambda_{\min}, \lambda_{\max})$  arrives at the chopper. (b) Space-time-diagrams for a pulsed source. The wavelength band  $(\lambda_{\min,+}, \lambda_{\max,-})$  at  $x_0$  depends on the time  $t$  and changes during the opening of the chopper. For the dimensioning of the chopper opening time, only the fastest neutrons  $\lambda_{\min,+}$  at  $t_0 - \vartheta$  and the slowest neutrons  $\lambda_{\max,-}$  at  $t_0 + \vartheta$  are important.

guarantee maximum statistics, it would be ideal to have the new pulse enter the decay volume at the moment the old one exits. In the case of ESS, of course, the frequency of the pulses is given by the source. The condition of the defined final pulse length and the entry-when-exit rule completely define the operating conditions for a chopped mode both at a continuous and a pulsed source. Opening and closing times of the chopper are neglected.

As a reference wavelength,  $\lambda_0 = 5 \text{ \AA}$  is taken. The flux is assumed to be wavelength independent in the region of interest, as the involved wavelength band is closed to the maximum and considered small ( $\Delta\lambda/\lambda < 0.1$ ). Chopper opening and closing are assumed to be negligibly fast. Possible background measurements leading to omission of certain pulses are not taken into account in either calculation.

### 5.2.1 Continuous Source

At the continuous source, the reactor, the wavelength spectrum is determined by the selector in front of PERC. It has the resolution of  $\Delta\lambda$ . For the continuous source, the spectrum is time-independent, see Fig. 5.17(a). In the

setup, there is therefore a Dornier selector [71] at 5 Å and a total wavelength band  $\Delta\lambda$  from 4.5 to 5.5 Å placed in front of the chopper for wavelength selection. The complete transmission of the 5 Å pulse and a triangular wavelength selection are (optimistically) assumed. This makes the total efficiency of the selector  $\kappa$  to be 0.5. Typical McStas simulations show a real transmission efficiency of ca 0.4 for the divergence in PERC beamline as it had been presented in Sec. 5.1. The condition on the final pulse length defines the chopper opening time  $2\vartheta$  and the entry-when-exit policy defines the frequency  $f$  and therefore the efficiency of the chopper. The two devices, chopper and selector, work independently from each other. The integral over time and wavelength for this configuration therefore a simple multiplication. The total flux can be estimated as:

$$\Phi_{ILL} = \phi_{0,ILL} \cdot f \Delta\lambda 2\vartheta. \quad (5.2)$$

The chopper opening time, defined by the resolution  $\Delta\lambda$  and the final pulse length  $p$  is

$$2\vartheta(x_0) = 2 \frac{p(t_0 + \tau) - 2l\tau}{2(x_0 + l) - p}. \quad (5.3)$$

And the repetition frequency at which such a chopper can open is defined by the opening time of the chopper plus the time the slowest neutron takes to travel through the decay volume:

$$\frac{1}{f} = \frac{\lambda_0(l+p) + \Delta\lambda(p-l)}{k} \quad (5.4)$$

with  $k = \frac{h}{m_n}$ . The optimum selector resolution can be achieved  $\partial_{\Delta\lambda}\Phi_{ILL} = 0$ , it depends only on the ratio of the total length of the decay volume and the final pulse:

$$\frac{\Delta\lambda}{\lambda} = \frac{l+p}{l-p} - \frac{l}{l-p} \sqrt{\frac{2 \cdot (l+p)}{2l-p}}. \quad (5.5)$$

$\Delta\lambda$  is 7.3 % for the optimum selector. State-of-the art Dornier selectors currently have a resolution of about 10% [71] which is close to the optimum resolution.

### 5.2.2 Pulsed Source

At pulsed sources like the ESS, the intensity and spectrum have a natural time structure. The spatial dilation of the pulse over time requires a careful choice of the position of an instrument that requires itself a finite spatial dilation of the pulse like PERC. The chopper in front of PERC at position  $x$  with respect to the source does both shape the pulse and select the wavelength by opening during  $2\vartheta$ . It is set such that the chopper is fully open at  $t = t_0$  when the reference  $5 \text{ \AA}$  emitted in the middle of the pulse arrives. The wavelength band has the limits:

$$\begin{aligned}\lambda_{\max,-} &= \frac{h}{m_n} \frac{t_0 - \tau - \vartheta}{x} \\ \lambda_{\min,+} &= \frac{h}{m_n} \frac{t_0 + \tau + \vartheta}{x}\end{aligned}\quad (5.6)$$

The allowed wavelength band varies with the distance between the source and the PERC position: It is larger at close positions and narrows down for larger distances. The spatial separation of these two wavelengths at the beam stop has to be the final pulse length  $p$  with a decay volume length of  $l$ . The chopper is set at position  $x$  and opens for:

$$2\vartheta(x) = 2 \cdot \frac{p(t_0 + \tau) - 2 \cdot l \cdot \tau}{2(x + l) - p}.\quad (5.7)$$

The resulting time-averaged flux is therefore the integral over the wavelength and the chopper opening time:

$$\Phi(x) = \int_{-\tau}^{+\tau} \left( \int_{\lambda_{\min}(t)}^{\lambda_{\max}(t)} \phi(\lambda(t), t) d\lambda \right) dt.\quad (5.8)$$

This double integral can be understood as follows: The spallation source is assumed to emit all wavelengths with constant intensity over the whole pulse  $2\tau$ . At each moment the chopper is open, i.e. in the time frame  $[t_0(x) - \vartheta, t_0(x) + \vartheta]$ , a wavelength band with the constant width  $\frac{k}{x} 2\tau$  arrives. However, the final intensity is not equally composed of all wavelengths. Not for every wavelength its whole initial intensity emitted over the complete spallation pulse is being used. A given wavelength  $\lambda$  is defined by two parts in time,  $T$  and  $\Delta$  beyond the reference time from the reference wavelength  $t_0: \lambda = \frac{k}{x}(t_0 + T + \Delta)$  where  $\Delta \in [-\vartheta, +\vartheta]$  and  $T \in [-\tau, +\tau]$ , the chopper being installed at position  $x$ . Fig 5.18(a) shows how to determine the fraction of

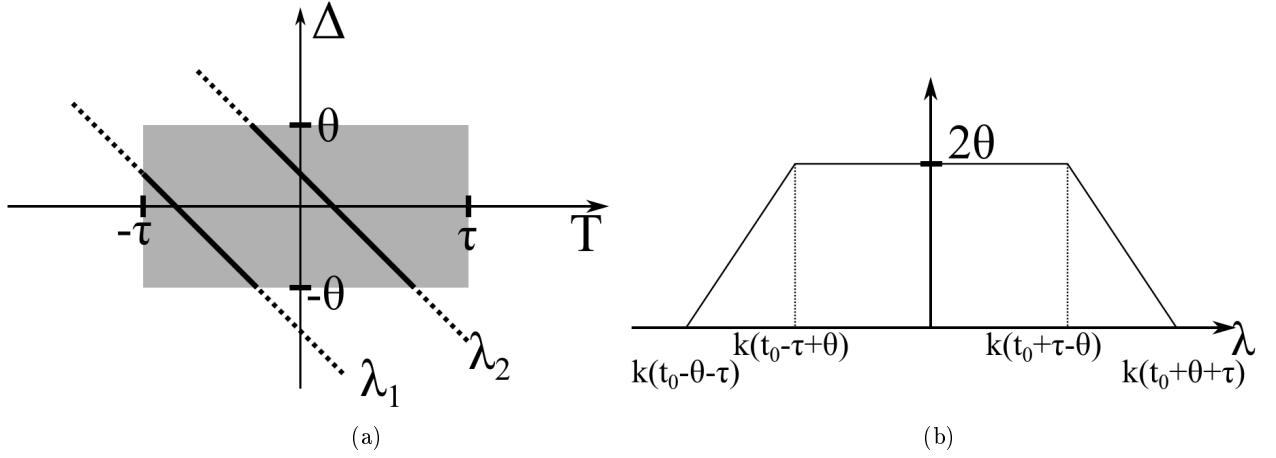


Figure 5.18: (a) Available time space from chopper ( $\Delta$ -axis) and spallation pulse ( $T$ -axis) to form a given wavelength, e.g.  $\lambda_1$  and  $\lambda_2$ . (b) Fraction of the wavelength emitted during  $2\theta$  contributing to the final intensity in function of the wavelength

the pulse a certain wavelength that contributes to the final intensity: Any wavelength can be described as a linear function with slope -1 in the box that is formed by the two time dimensions pulse and chopper, i.e.,  $T = \frac{\lambda}{k} - t_0 - \Delta$ . The length of the linear function inside the box determines the fraction of the pulsed used and is represented in Fig 5.18(b). Hence, the resulting intensity integrated over chopper and pulse is the area of this graph, i.e.  $2\tau k 2\theta$ .

$$\Phi(x) = \int_{-\tau}^{+\tau} \left( \int_{\lambda_{\min}(t)}^{\lambda_{\max}(t)} \phi(\lambda(t), t) d\lambda \right) dt = f \cdot \phi \cdot 2\tau \frac{k}{x} \cdot 2\theta(x) \quad (5.9)$$

The flux depends on the distance of the experiment from the source in a non-linear way due to the counteracting of chopper-opening time and wavelength spectrum. This is depicted in Fig. 5.17(b) in the form of a space time diagram: At short distances, the accepted wavelength band is wide but the chopper opens only for a short time whereas the contrary is true for long distances. Fig. 5.19 represents both parameter as a function of distance to the source.



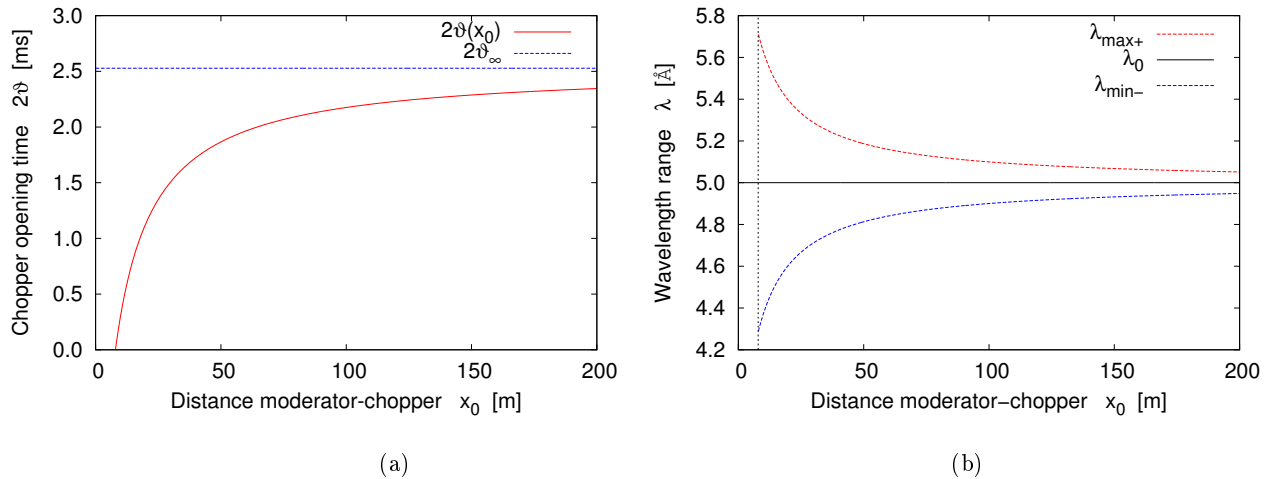


Figure 5.19: Chopper opening time (a) and minimum and maximum wavelength in a pulse for PERC at the ESS (b) as function of distance. The dashed line in (b) indicates the minimum distance  $x_{0,\min}$ .

### 5.2.3 Comparison and Optimizing Parameters

Fig. 5.20 shows the gain in flux by an installation of PERC at the ESS compared to the continuous ILL source. The maximum gain attained is about 7 at the optimum distance. As pointed out before, the wavelength band (i.e., the resulting intensity) and the time structure are independent for a continuous source. Therefore, the devices creating them can be optimized separately and there is no influence in terms of statistics on the distance from the source. Measurement background and space concerns advise to choose a position far away from the source, as long as losses in the neutron guide can be neglected.

The pulsed source on the other hand entangles closely the time structure and the wavelength band and therefore the distance from the source is an important parameter to optimize. At close distances, the wavelength band allowed by the final pulse width is large, but the chopper opens only shortly, such that only few neutrons emitted over the complete initial pulse make it through the chopper in front of PERC. At larger distances however, the chopper can be opened for a longer time, but the wavelength band available is much smaller. These two counter-acting effects lead to a maximum that for the parameters considered here is at about 19 m. The distance is very

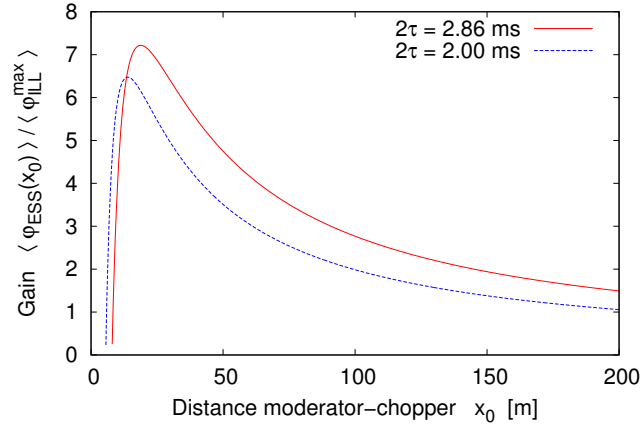


Figure 5.20: Gain for PERC at the ESS as function of distance to the moderator, compared to the optimum at the ILL. The gain for an initial pulse length of 2 ms obtained by a chopper at the moderator exit is also shown.

close to the source and there are space and background concerns. At larger distances, the gain gets smaller but is still existent.

This gain factor is obtained for a condition where the pulses at the continuous source follow one after another into the decay volume such that there is always one and only one pulse inside. The continuous source modeled after the example of ESS has a frequency of 14 Hz. This leads to breaks between pulses where the decay volume is empty. If the source would perform at the optimum frequency for the 8 m decay volume at the optimum distance, the wavelength band would allow for a frequency of  $f_{\text{ESS}}^{\text{opt}} = 83$  Hz. This would increase the gain factor up to 43. This is higher than the assumed initial difference in intensity in Eqn. (5.1): The transmission function assumed for the velocity selector at the continuous source reduces the flux in the wavelength band  $(\lambda_0 - \Delta\lambda, \lambda_0 + \Delta\lambda)$  by a factor of 2. On the other hand, optimum bandwidth  $2\Delta\lambda = 0.73 \text{ \AA}$  and chopper opening time  $2\vartheta = 1.24$  ms are slightly larger than at the pulsed source:  $\lambda_{\text{max}} - \lambda_{\text{min}} = 2k\tau/x_0 = 0.60 \text{ \AA}$  and  $2\vartheta = 1.07$  ms, respectively.

One can think of two strategies to increase the gain at the ESS with the current repetition rate:

- *Restrict the initial pulse length.* The reduction of the pulse length at

the source makes it possible to increase the fraction of the wavelength used, making Fig. 5.18 more rectangular. This is advantageous at short distances, as there the chopper opening tends to be short. With the given ESS pulse length, the maximum is already at the short 19 m distance and reducing the pulse shifts the minimum towards the source even more. An example is given for  $2\tau = 2$  ms in Fig. 5.20.

- *Use multiple wavelength bands.* The low frequency of ESS can be turned to an advantage by selecting multiple wavelength bands of a pulse. This increases the total flux used for measurements and in addition can help to study systematic errors related to the wavelength such as polarization. At a continuous source, different wavelength bands can be accessed by changing the selector and adapting the chopper frequency. Such measurements would be separated in time.

The final pulse length  $p$  is a defining parameter of the gain. Increasing it would lead to a gain for both source types: The chopper opening at the continuous source can be increased, see Eqn. 5.3, whereas at the pulsed source, the chopper opening and the wavelength band increase. Overall, for a given distance, the relative gain remains similar. However, increasing  $p$  draws toward the continuous mode, dismissing the purpose of the pulsed mode: a better control of systematics, as a large  $p$  means a less localized pulse. A possible optimization of the decay volume length for the use of a PERC-like experiment at a pulsed source is limited if compared to the same exact set-up at a continuous source. In the set-up of the continuous source, the wavelength band width is fix and given by the velocity selector with a fixed resolution. Naturally, for a given final pulse length, its efficiency is the better the shorter the decay volume is and gets worse for longer volumes. With the assumed post-selector spectrum ranging from 4.5 to 5.5 Å, the  $p/l$  ratio has to be higher than 0.18 so that the chopper at the continuous source can still open. This means for a final pulse length of 2 m, the decay volume has to be shorter than 11 meters. For decay volumes longer than this distance, an installation at ESS is always advantageous at any distance from the source, as the configuration is impossible at a continuous source. However, it has to be analyzed whether an experiment of such a long decay volume would benefit in terms of statistics and systematics, as the average flux will tend to be low.

# 6

## Conclusion

This thesis has experimentally proven the feasibility of neutron polarization, polarimetry and flipping at an accuracy of  $10^{-4}$ , all the essential ingredients necessary for *polarized* neutron beta decay experiments. The contribution of imperfect neutron polarization to the systematic errors of such experiments can thus be reduced to a level competitive to other systematic influences, pushing the accuracy beyond  $10^{-3}$  for the new generation of experiments. In this thesis, two methods were used to polarize neutrons to a high degree: helium spin filters and polarizing supermirrors. With both methods, polarization in a satisfying range were reached. The polarization by helium was driven over 99.99% by enhancing the opacity of the cell. A detailed study on depolarization in supermirrors with the help of the OTB revealed a better performance and oppression of wrongly oriented magnetic domains at high magnetic fields; subsequently, polarizations up to 99.97 % were measured in the crossed X-SM supermirror geometry. The detailed studies on depolarization in these mirrors confirms and generalizes preceding measurements on magnetism in ferromagnetic multilayers. Depolarizing effects could be attributed largely to incomplete polarization of the ferromagnetic supermirror layers. In addition to a large magnetic field, depolarization can

be minimized by using the lowest supermirror factor  $m$  appropriate for the beam divergence and bender curvature, generally low incidence angles and choosing CoTi mirrors at low and FeSi mirrors at high fields.

The two methods possible to polarize a large, divergent, polychromatic neutron beam, supermirrors and helium cells, have both been experimentally proven to provide satisfactory polarization in this thesis. A third idea would be to combine the two methods, by first polarizing the beam with a single super mirror bender and then further filter out the remaining "wrong" spin orientation with a helium cell. The following section discusses the advantages and disadvantages of the three methods with respect to an experiment like PERC. The last part of the chapter gives an outlook and direction for future work.

## 6.1 Comparison Of Polarization Methods

The primary key numbers for a polarizer system for PERC is the polarizing power and the transmission of the system. The polarizing power for all three systems is estimated feasible to a level satisfactory for PERC. The transmission of the X-SM geometry is constant over time, as it is built solely from supermirrors. It has a transmission of about 12.5% of the unpolarized beam, as in addition to the intensity loss due to polarization, each bender geometry cuts off about half the remaining intensity [26]. For helium cells, the enhanced polarizing performance is paid with reduced transmission due to the increased opacity. Opacities necessary for 99.99 % polarization have a transmission in the order of 6 % of the unpolarized beam. Furthermore, this polarization and transmission change over time due to the depolarization of the helium. In the following, a single helium cell is compared to the combination of the bender and a supplementary cell and their performance over time is considered. Later, the different systematic errors from all three polarization methods are discussed.

In order to compare a single cell and a combined system, a cell  $Z$  with a length of 14 cm and a  $T_1$  of 240 hours is assumed; calculations are performed for a wavelength of 5.3 . For the bender  $\mathbf{B}$  , an average polarization degree of 98 % is assumed, the intensity loss due to geometry is estimated to be

50% for the beam based on McStas simulations. We assume that the up-component is the desired spin orientation, the polarizing components can thus be expressed as:

$$\mathbf{Z} = \begin{bmatrix} \exp(-Q(1 - P_{\text{He}}(t))) & 0 \\ 0 & \exp(-Q(1 + P_{\text{He}}(t))) \end{bmatrix}, \quad \mathbf{B} = \begin{bmatrix} 0.99 \cdot 0.5 & 0 \\ 0 & 0.01 \cdot 0.5 \end{bmatrix}. \quad (6.1)$$

The condition is that after 24 hours the resulting polarization as defined in Eqn. 3.4 is still 0.9999. The calculation is compared to a single helium cell that has the same requirement and it is assumed that the helium polarization decreases strictly exponentially as in Eqn. 3.30. The only parameter changing between the two cells is the cell pressure. Tab. 6.1 gives an overview on the pressures required.

Initial $P_{\text{He}}$	pressure in cell combined with bender [bar]	pressure in single cell [bar]
0.75	0.72	1.35
0.80	0.66	1.22

Table 6.1: Necessary pressure for a neutron polarization of 0.9999 after 24 hours in use, given for two initial helium polarization values.

While by definition of the problem the neutron polarization is fixed to 0.9999, the transmission (Eqn. 3.28) is shown in Tab. 6.2 and compared to the case where the polarization takes place by a single helium cell, Tab. 6.3.

The transmission in the combined set-up is a few percents higher than for the helium cell alone. Due to the lower opacity of the cell as a result of the pre-polarization by the bender, the sensitivity to time and initial helium polarization is smaller. In comparison, the transmission obtained by the supermirror based X-SM geometry is 12.5 %.

Initial $P_{\text{He}}$	transmission after 24 hours	transmission loss since filling	polarization loss since filling $\cdot 10^{-5}$
0.75	0.0704	-0.0227	-4.28
0.80	0.0899	-0.0289	-4.28

Table 6.2: Transmission of the combination bender and cell after 24 hours in use. The pressure in the cell is adjusted such that the polarization is 0.9999 after the 24 hours, given for two initial helium polarization values.

Initial $P_{He}$	transmission after 24 hours	transmission loss	polarization loss $\cdot 10^{-5}$
0.75	0.0479	-0.0327	-6.47
0.80	0.0756	-0.0517	-6.47

Table 6.3: Transmission of a single helium cell after 24 hours in use. The pressure in the cell is adjusted such that the polarization is 0.9999 after the 24 hours

A polarizer system that includes helium cells is confronted with two systematic effects: The polarization is time and wavelength dependent. The wavelength dependence can be corrected for easily from the analytical model, Eqn. (3.29). The time dependence of the performance is more challenging:

- The depolarization of the helium necessitates a regular exchange of the helium cells. In our experiments, performed with state-of-the-art equipment, changes were necessary at least every 24 hours to remain sufficiently high in polarizing/analyzing power.
- A regular change of the cells also implies access to the polarizing area. Due to the flux loss at the bender entry and consequential irradiation and activation of beamline material, a helium and bender combination would be problematic for safety reasons. An impasse would be to either install a tube by which helium can be exchanged from a distance, taking into account helium polarization losses, or to adapt an in-beam polarizer like [79] that constantly re-polarizes helium in-situ. One can also think of adding a valve, such that the helium opacity can be adjusted to accommodate for different wavelength bands.
- Magnetic shielding: On the PERC beamline, the polarization of the beam takes place close to the decay volume that is equipped with a 1.5 T field. Polarized helium necessitates a highly homogeneous holding field and if flipping of the helium is desired, an equally clean flipping signal. Therefore, shielding of the helium unit has to be chosen carefully due to possible contamination from the decay volume magnet system.

On the other hand, a polarizer system that includes a supermirror bender, while stable in time and over wavelength, the bender changes the beam direction and beam distribution. In the crossed geometry, the beam

is deflected in two, perpendicular directions. This must be considered when aligning subsequent components behind the bender(s), e.g. the PERC decay volume. The inhomogeneous beam distribution can lead to an increase of systematics due to a non-uniform beam.

A bender is less sensitive to stray fields from the decay volume than a helium cell. However, in the single helium cell, the spin orientation can be directly selected while a polarization system that includes a bender necessitates an additional spin flipper. Care must be taken that the spin flipper is in an appropriate field in order to perform the spin flip over the distance available between the polarizer system and the decay volume.

In conclusion: Polarization by a single helium cell provides the best performance for polarization, but has several disadvantages in terms of time and wavelength-stability and the transmission is low. The combination of such a cell with a polarizing supermirror bender reduces the time dependence and offers a better transmission. The combination of two bendings in the X-SM geometry has an even better transmission. While the polarization reached is  $2 \cdot 10^{-4}$  times lower than with a helium cell involved, the performance of the supermirrors is constant. If this polarization degree is not sufficient, the use of a combined system with a bender and a helium cell is recommended, as the time dependence is lower than for a single cell. However, this method combines the time difficulties from helium with the change in beam distribution of the bender.

The reduction of intensity due to high polarization is high for any of the presented polarization methods, their transmission ranges from 5-12.5 %.

## 6.2 Future Work

In the future, the necessary modifications on the presented techniques have to be made to accommodate for neutron beta decay experiments [23, 12, 13]. In particular, a polarizer for PERC has to be designed and tested. Alternatives are to adjust an on-line helium pumping station similar to [79] or to use a supermirror crossed geometry. For reasons of statistics, stability and logistics, a supermirror geometry is advised. The current results of the X-SM geometry were obtained for a typical wavelength band



at  $5.3 \text{ \AA} \pm \frac{0.1-5.3}{5.3} \lambda$  for a narrow, well-collimated beam. In application to neutron decay experiment, it will be necessary to prove it's application to the complete cross-section and the acceptance of all incidence angles and a resulting uniformity of the polarization. The opaque test bench is an ideal tool for these tests.

Special care has to be given to the design of the magnetizing field of the polarizer: The data presented in this experiment show that a field of at least 0.8 T is needed to optimize the mirrors' performance. The magnetizing field should not interfere with the longitudinal field of the decay volume nor with spin flipping and spin turning devices between the polarizer and the decay volume and it has to maintain the quantization axis over the complete beam cross-section. Similarly, for the case of a helium spin filter, extensive magnetic shielding would be necessary to create a suitably homogeneous field in the order of 10-40 Gauss to maintain and reliably flip the helium polarization. In addition, the spin has to be turned between the polarizer system and the PERC decay volume in order to align with the magnetic field of the decay volume.

For any polarizing system for PERC, it will be necessary to determine the created background radiation and its influence on the spectroscopy of the decay particles downstream.

It has been shown in this thesis that the PERC experiment would statistically benefit from a long pulsed spallation source like the ESS. More detailed calculations and simulations with realistic source spectra are needed to verify the results and further optimize the beamline.

As shown in this thesis, the polarized supermirror performance can be enhanced considerably by applying strong magnetizing fields oppressing depolarization. This suppresses off-specular scattering originating from varying lateral magnetic potentials (misaligned domains). Even higher polarization degrees could be achieved by shielding the remaining off-specular scattering of the last reflection. This technique requires intimate knowledge of the location of the specular scattering on the supermirror and is appropriate for small, highly collimated beams with low divergence.

For two samples, the polarizing power was tested at varying magnetizing fields and for both of them, the polarizing power at maximum field dropped. More data on more different mirrors and at higher fields could shed more

light on the issue. If this tendency is confirmed, it would be suitable in a polarizer system that necessitates several reflections that the first reflection takes place in a lower field to gain maximum polarizing power. Subsequent reflections, more sensitive to depolarization should take place at high fields in order to suppress these depolarizing effects. The drop in polarizing power at high field might possibly come from an altered neutron optical contrast for the  $\uparrow$  and  $\downarrow$  spin at high fields in the ferromagnetic material, leading to an undesired reflection of the  $\downarrow$ -component at the frontier to the non-magnetic layer.

The techniques shown are not limited to neutron beta decay experiments. A high precision reflectometer can be constructed with the presented polarization techniques, specifically by combining the Opaque Test Bench with an improved, precise angular control of the sample and a well defined, monochromatic, collimated beam in addition to a position-sensitive detector. Such a high-precision instrument would have plenty applications, in particular for clear imaging of the size and dynamic of magnetic domains in materials.

# Bibliography

- [1] J. Grimm, and W. Grimm. *Die schönsten Kinder- und Hausmärchen*. Hille und Partner, 2011.
- [2] J. Beringer, et al. Review of particle physics. *Phys. Rev. D*, 86:010001, 2012.
- [3] H. Abele. The neutron alphabet: Exploring the properties of fundamental interactions. *Nuclear Instruments and Methods in Physics Research Section A: Accelerators, Spectrometers, Detectors and Associated Equipment*, 611(2-3):193 – 197, 2009.
- [4] D. Dubbers, and M. G. Schmidt. The neutron and its role in cosmology and particle physics. *Rev. Mod. Phys.*, 83:1111–1171, Oct 2011.
- [5] C. S. Wu, et al. Experimental test of parity conservation in beta decay. *Phys. Rev.*, 105:1413–1415, 1957.
- [6] T. D. Lee, and C. N. Yang. Question of parity conservation in weak interactions. *Phys. Rev.*, 104:254–258, 1956.
- [7] M.J. Ramsey-Musolf. Neutrons and the new standard model. *Nuclear Instruments and Methods in Physics Research Section A: Accelerators, Spectrometers, Detectors and Associated Equipment*, 611(2–3):111 – 116, 2009.
- [8] J. Liu, et al. Determination of the Axial-Vector Weak Coupling Constant with Ultracold Neutrons. *Phys.Rev.Lett.*, 105:181803, 2010.
- [9] M. P. Mendenhall, et al. Precision measurement of the neutron  $\beta$ -decay asymmetry. *Phys. Rev. C*, 87:032501, Mar 2013.
- [10] Y.i Arimoto, et al. Present status of neutron fundamental physics at j-parc. *Progress of Theoretical and Experimental Physics*, 2012(1), 2012.

- [11] W.S. Wilburn, et.al. Measurement of neutron decay parameters—the abba experiment. *NIST Journal of Research*, 110:389–393, 2005.
- [12] L. Barrón-Palos, et al. A measurement of correlation parameters in the decay of polarized free neutrons: The abba experiment. *Journal of Physics: Conference Series*, 239(1):012013, 2010.
- [13] "<http://research.physics.lsa.umich.edu/chupp/panda>". accessed 7th August 2013, 14:15.
- [14] B. Plaster, et al. A solenoidal electron spectrometer for a precision measurement of the neutron -asymmetry with ultracold neutrons. *Nuclear Instruments and Methods in Physics Research Section A: Accelerators, Spectrometers, Detectors and Associated Equipment*, 595(3):587 – 598, 2008.
- [15] W.S. Wilburn, et.al. Measurement of the neutrino-spin correlation parameter B in neutron decay using ultracold neutrons. *Revista Mexicana de Fisica*, page 119, 2009.
- [16] B. Märkisch, et al. The new neutron decay spectrometer Perkeo III. *Nuclear Instruments and Methods in Physics Research Section A: Accelerators, Spectrometers, Detectors and Associated Equipment*, 611(2 - 3):216 – 218, 2009.
- [17] O. Zimmer, et al. "aSPECT"— a new spectrometer for the measurement of the angular correlation coefficient a in neutron beta decay. *Nuclear Instruments and Methods in Physics Research Section A: Accelerators, Spectrometers, Detectors and Associated Equipment*, 440(3):548 – 556, 2000.
- [18] P. Bopp, et al. The superconducting neutron decay spectrometer PERKEO. *Nuclear Instruments and Methods in Physics Research Section A: Accelerators, Spectrometers, Detectors and Associated Equipment*, 267(2 - 3):436 – 447, 1988.
- [19] J. Reich, et al. A measurement of the beta asymmetry in neutron decay with PERKEO II. *Nuclear Instruments and Methods in Physics Research Section A: Accelerators, Spectrometers, Detectors and Associated Equipment*, 440(3):535 – 538, 2000.

- [20] M. Schumann, et al. Measurement of the proton asymmetry parameter in neutron beta decay. *Phys. Rev. Lett.*, 100:151801, 2008.
- [21] M. Schumann, et al. Measurement of the neutrino asymmetry parameter  $B$  in neutron decay. *Phys. Rev. Lett.*, 99:191803, 2007.
- [22] D. Mund, et al. Determination of the weak axial vector coupling  $\lambda=g_A/g_V$  from a measurement of the  $\beta$ -asymmetry parameter  $a$  in neutron beta decay. *Phys. Rev. Lett.*, 110:172502, Apr 2013.
- [23] D. Dubbers, et al. A clean, bright, and versatile source of neutron decay products. *Nuclear Instruments and Methods in Physics Research Section A: Accelerators, Spectrometers, Detectors and Associated Equipment*, 596(2):238 – 247, 2008.
- [24] X. Wang, G. Konrad, and H. Abele. RxB drift momentum spectrometer with high resolution and large phase space acceptance. *Nuclear Instruments and Methods in Physics Research Section A: Accelerators, Spectrometers, Detectors and Associated Equipment*, 701(0):254 – 261, 2013.
- [25] G. Konrad, et al. Neutron decay with PERC: a progress report. *Journal of Physics: Conference Series*, 340(1):012048, 2012.
- [26] M. Kreuz, et al. The crossed geometry of two super mirror polarisers—a new method for neutron beam polarisation and polarisation analysis. *Nuclear Instruments and Methods in Physics Research Section A: Accelerators, Spectrometers, Detectors and Associated Equipment*, 547(2-3):583 – 591, 2005.
- [27] N. Rebrova, Heidelberg University. private communication, 2011.
- [28] W. Gavin Williams. *Polarized Neutrons*. Clarendon Press - Oxford, 1988.
- [29] F. Bloch. On the magnetic scattering of neutrons. *Physical Review*, 50:259–260, 1936.
- [30] O. Halpern. Double refraction and polarization of neutron beam. *Physical Review*, 75, 1949.

- [31] Masahiko Utsuro, and Vladimir K. Ignatovich. *Handbook of Neutron Optics*. Wiley-Vch, 2010.
- [32] W.R. Leo. *Techniques for Nuclear and Particle Physics Experiments*. Springer-Verlag, 1994.
- [33] A.P. Serebrov, et al. New method for precise determination of neutron beam polarization. *Nuclear Instruments and Methods in Physics Research Section A: Accelerators, Spectrometers, Detectors and Associated Equipment*, 357(2-3):503 – 510, 1995.
- [34] S.V. Grigoriev, et al. Spatial spin resonance of polarized neutrons in amplitude-modulated magnetic fields. *Nuclear Instruments and Methods in Physics Research Section A: Accelerators, Spectrometers, Detectors and Associated Equipment*, 389(3):441 – 446, 1997.
- [35] D.J. Griffiths. *Introduction to Quantum Mechanics*. Addison Wesley, 2004.
- [36] C.J. Christensen, V.E. Krohn, and G.R. Ringo. Measurement of Angular Correlations in the Decay of Polarized Neutrons. *Phys.Rev.*, C1:1693–1698, 1970.
- [37] B.G. Erozolinskii, et al. New measurements of the electron-neutron spin asymmetry in neutron beta-decay. *Physics Letters B*, 263(1):33 – 38, 1991.
- [38] G. Badurek, H. Rauch, and A. Zeilinger. Dynamic concepts in neutron polarization. *Zeitschrift für Physik B Condensed Matter*, 38(4):303–311, 1980.
- [39] U. Schmidt, et al. Neutron polarization induced by radio frequency radiation. *Phys. Rev. Lett.*, 84:3270–3273, 2000.
- [40] Christoph Gösselsberger. *Entwicklung eines Wanderwellen-Neutronenspinresonators*. PhD thesis, Technische Universität Wien, Austria, 2012.
- [41] V. F. Sears. Neutron scattering lengths and cross sections. *Neutron News*, 3(3):26–37, 1992.

- [42] F. Mezei. Novel polarized neutron devices: supermirror and spin component amplifier. *Communications on Physics*, pages 81–85, 1976.
- [43] F. Mezei. Novel approach to polarized neutron scattering. *Physica B+C*, 86-88(Part 3):1049 – 1052, 1977.
- [44] P. Böni, et al. Challenges in the field of large-m supermirrors. *Physica B: Condensed Matter*, 241 - 243(0):1060 – 1067, 1997.
- [45] O. Schaerpf. Comparison of theoretical and experimental behaviour of supermirrors and discussion of limitations. *Physica B: Condensed Matter*, 156-157:631–638, 1989.
- [46] O. Zimmer, et al. Spin filters and supermirrors: a comparison study of two methods of high-precision neutron polarisation analysis. *Nuclear Instruments and Methods in Physics Research Section A: Accelerators, Spectrometers, Detectors and Associated Equipment*, 440(3):764 – 771, 2000.
- [47] J. B. Hayter, J. Penfold, and W. G. Williams. Compact polarising soler guides for cold neutrons. *Journal of Physics E: Scientific Instruments*, 11(5):454, 1978.
- [48] K.P. Coulter, et al. Neutron polarization with polarized  $^3\text{He}$ . *Nuclear Instruments and Methods in Physics Research Section A: Accelerators, Spectrometers, Detectors and Associated Equipment*, 270(1):90 – 94, 1988.
- [49] W. Heil, et al.  $^3\text{He}$  neutron spin filter. *Physica B: Condensed Matter*, 267-268(0):328 – 335, 1999.
- [50] W. Heil, et al.  $^3\text{He}$  neutron spin filter at ill. *Physica B: Condensed Matter*, 241 - 243(0):56 – 63, 1997.
- [51] C.Y. Jiang, et al. Polarized  $^3\text{He}$  neutron spin filters at Oak Ridge National Laboratory. *Physics Procedia*, 42(0):191 – 199, 2013.
- [52] A.K. Petoukhov, et al. Compact magnetostatic cavity for polarised  $^3\text{He}$  neutron spin filter cells. *Nuclear Instruments and Methods in Physics Research Section A: Accelerators, Spectrometers, Detectors and Associated Equipment*, 560(2):480 – 484, 2006.

- [53] O. Zimmer, et al. High-precision neutron polarization analysis using opaque spin filters. *Physics Letters B*, 455(1-4):62 – 68, 1999.
- [54] O. Zimmer. A method for precise neutron beam polarisation analysis using an opaque spin filter. *Physics Letters B*, 461(4):307 – 314, 1999.
- [55] M. Sharma, et al. Neutron beam effects on spin-exchange-polarized  $^3\text{He}$ . *Phys. Rev. Lett.*, 101:083002, 2008.
- [56] A. Devishvili, et al. SuperADAM: Upgraded polarized neutron reflectometer at the Institut Laue-Langevin. *Review of Scientific Instruments*, 84(2):025112, 2013.
- [57] H. Abele, et al. Characterization of a ballistic supermirror neutron guide. *Nuclear Instruments and Methods in Physics Research Section A: Accelerators, Spectrometers, Detectors and Associated Equipment*, 562(1):407 – 417, 2006.
- [58] T. Bigault, Service d’Optique des Neutrons. private communication, 2012.
- [59] O. Halpern, and T. Holstein. On the passage of neutrons through ferromagnets. *Phys. Rev.*, 59:960–981, 1941.
- [60] E.I Kentzinger, et al. Depth-resolved investigation of the lateral magnetic correlations in a gradient nanocrystalline multilayer. *Phys. Rev. B*, 77:104435, 2008.
- [61] W.H. Kraan, et al. Study of domain structures in FeCo/TiZr multilayers by means of 3d neutron depolarisation. *Journal of Magnetism and Magnetic Materials*, 236(3):302 – 311, 2001.
- [62] M. T. Rekveldt. Transmission of polarised neutrons in magnetic materials. *Physica B: Condensed Matter*, 267–268(0):60 – 68, 1999.
- [63] F. Ott. Réflectivité hors spéculaire et diffraction de surface. *J. Phys. IV France*, 11:67–101, 2001.
- [64] T. Bigault, Service d’Optique des Neutrons. private communication, 2012.



- [65] C. Klauser, et al. Ultra-sensitive depolarization study of polarizing coti supermirrors with the opaque test bench. *Physics Procedia*, 42(0):99 – 105, 2013.
- [66] Th. Lauer, Mainz University. private communication, 2011.
- [67] W.H. Kraan, et al. Domain structure in FeCo/TiZr multilayers analysed from 3d neutron depolarisation. *Physica B: Condensed Matter*, 267–268(0):75 – 78, 1999.
- [68] R.W.E van de Kruijs., et al. Polarization analysis of off-specular neutron scattering from domains and rough interfaces in a FeCoV/TiZr multilayer. *Applied Physics A*, 74(1):s1550–s1553, 2002.
- [69] C. Klauser, et al. High precision depolarisation measurements with an opaque test bench. *Journal of Physics: Conference Series*, 340(1):012011, 2012.
- [70] Gary J. Feldman, and Robert D. Cousins. Unified approach to the classical statistical analysis of small signals. *Phys. Rev. D*, 57:3873–3889, Apr 1998.
- [71] Neutron velocity selector, blade rotor developed by dornier/gkss/ptb. Technical report, Daimler-Benz Aerospace, Dornier Satellitensysteme GmbH.
- [72] U. Schmidt, Heidelberg University. private communication, 2012.
- [73] P. Willendrup, et al. *McStas Manual*. 2012.
- [74] T. Soldner, A. Petoukhov, and C. Plonka. Installation and first tests of the new PF1b polariser. Technical Report ILL03SO10T, Institut Laue-Langevin, 2002.
- [75] J. Klenke, FRM II. private communication, 2010.
- [76] Ess technical design report. Technical report, European Spallation Source, Lund, April 2013. [http://esss.se/documents/tdr/TDR\\_final.pdf](http://esss.se/documents/tdr/TDR_final.pdf), accessed 4th June 2013, 9:12.

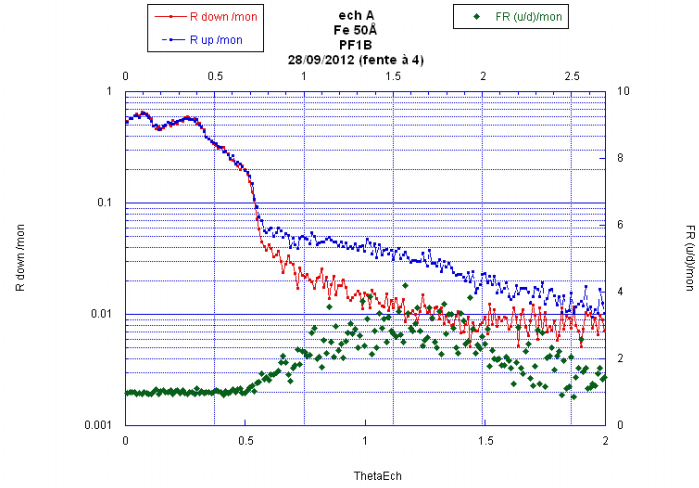
- [77] B. Märkisch. Measurements of correlation coefficients in pulsed neutron beams. *Physics Procedia*, submitted.
- [78] C. Klauser, H. Abele, and T. Soldner. Beam line parameters for perc at the long-pulse spallation source. *Physics Procedia*, accepted.
- [79] X. Tong, et al. In situ polarized  $^3\text{He}$  system for the magnetism reflectometer at the spallation neutron source. *Review of Scientific Instruments*, 83(7):075101, 2012.



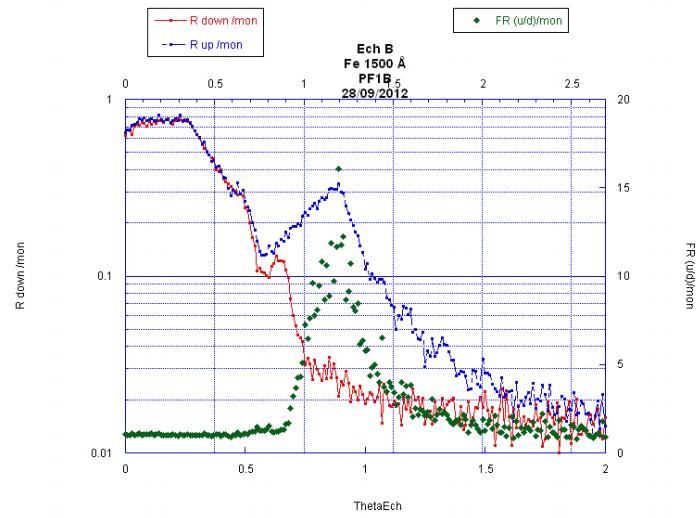
## Reflectivity Curves of Samples From T3

Figure A.1: Monolayers

(a) Fe 50 Å, sample A



(b) Fe 1500 Å, sample B



(c) Fe 1500 Å, sample K

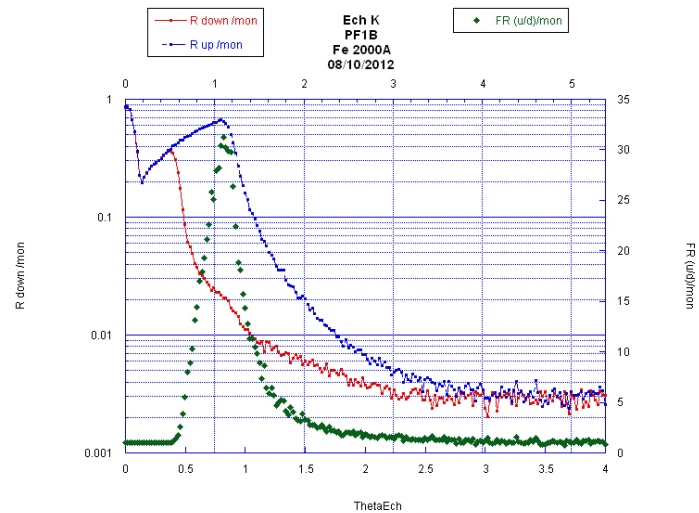
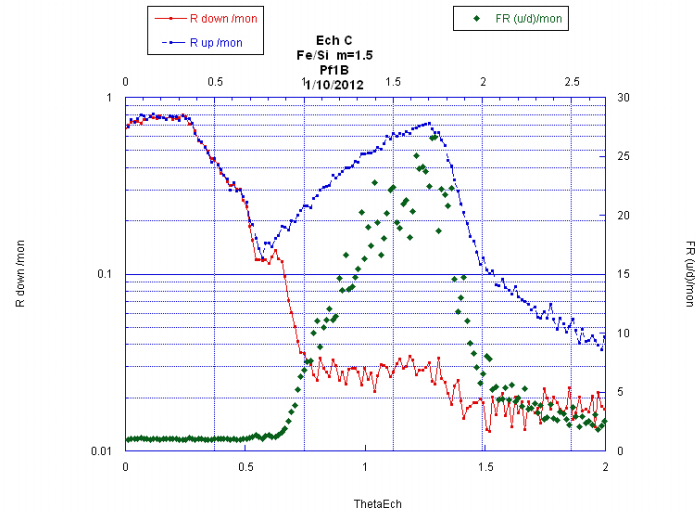
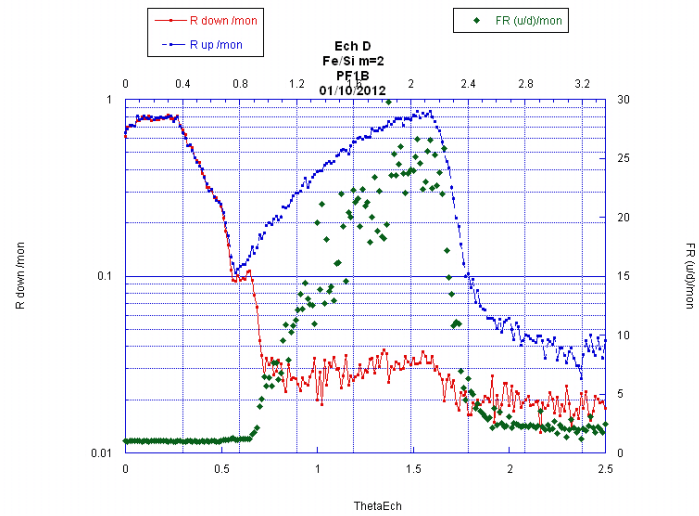
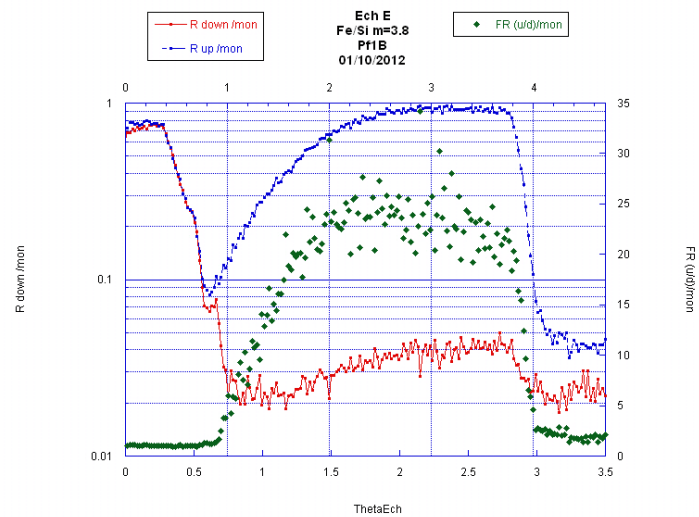
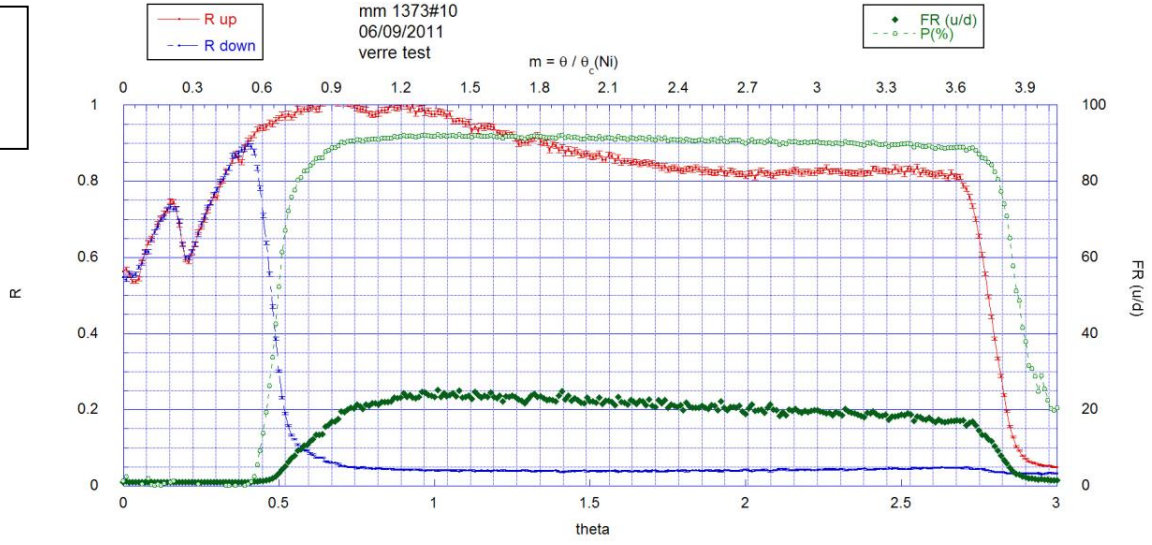


Figure A.2: FeSi supermirrors

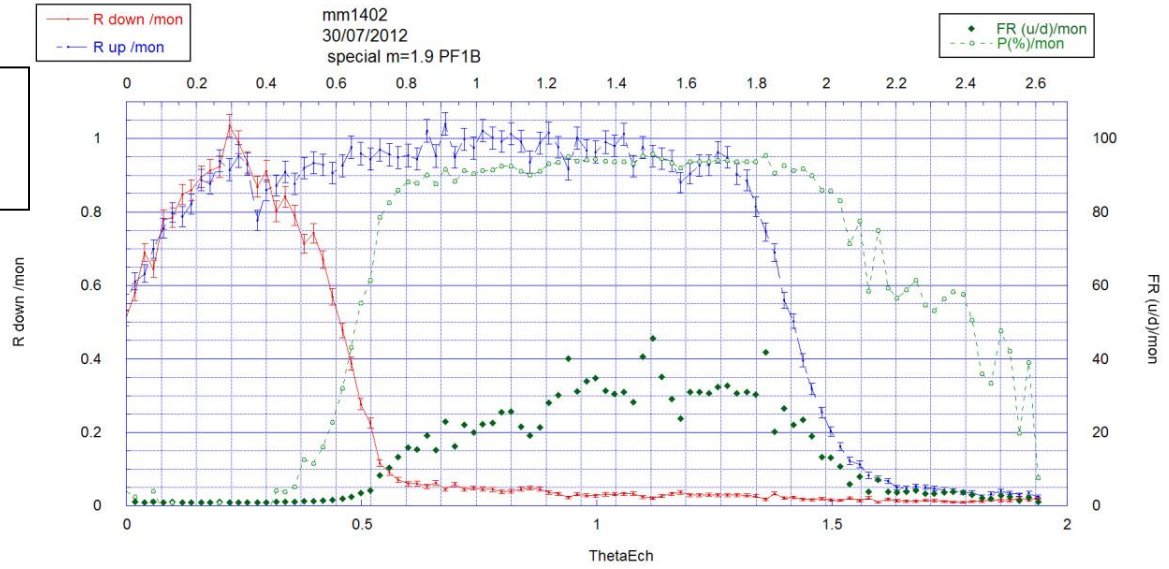
(a) FeSi  $m=1.5$ , sample C(b) FeSi  $m=2.0$ , sample D(c) FeSi  $m=3.8$ , sample E

112 APPENDIX A. REFLECTIVITY CURVES OF SAMPLES FROM T3

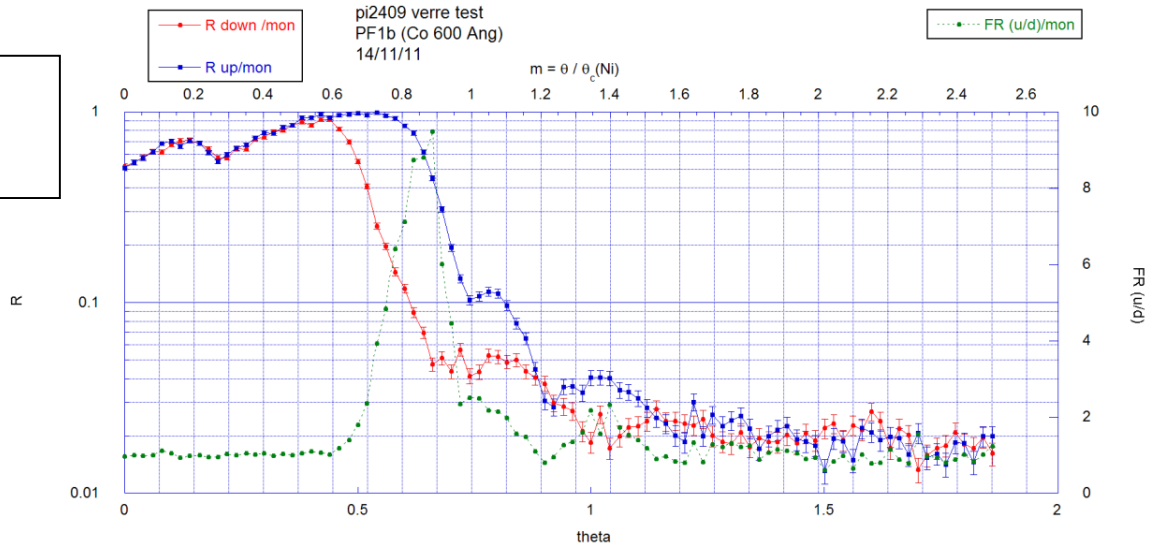
FeSi m=3.6  
Sample 2



FeSi m=1.9  
Sample J



Co 600 Å  
Sample 11



Co 2000 Å  
Sample 9

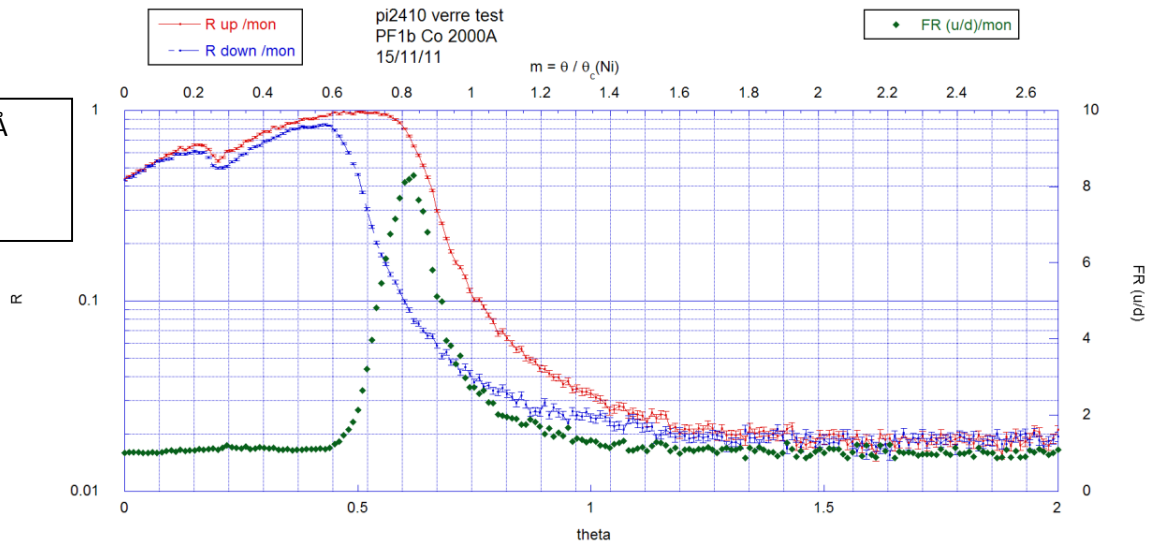
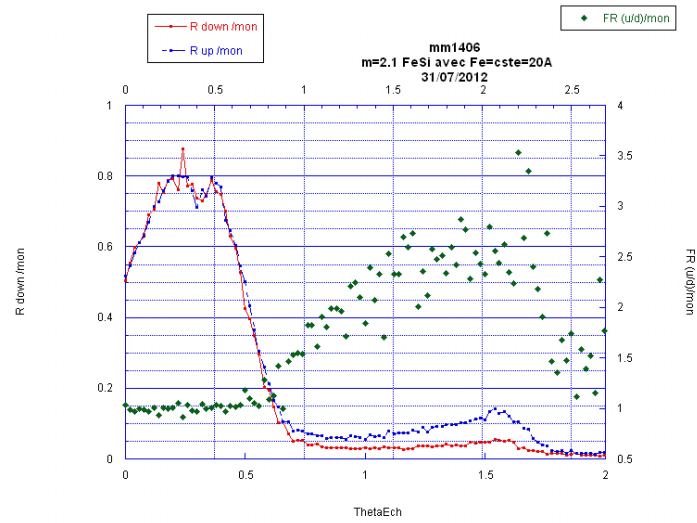
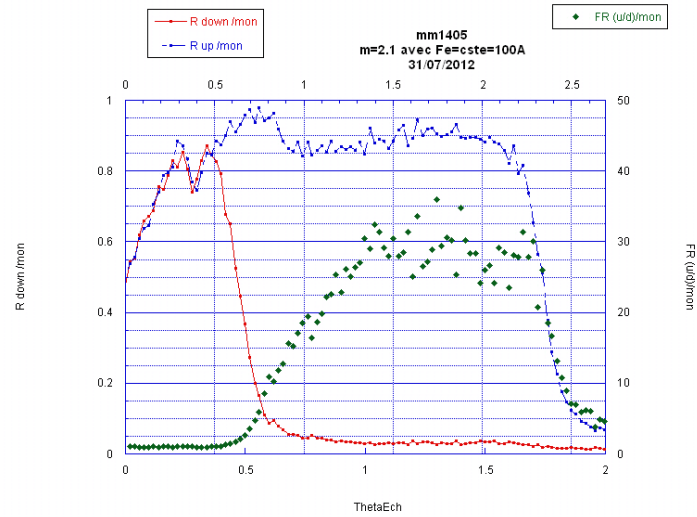


Figure A.3: FeSi Pseudo-supermirrors

(a) Pseudo  $m=2.0$ ,  $20 \text{ \AA}$  spacing, sample M

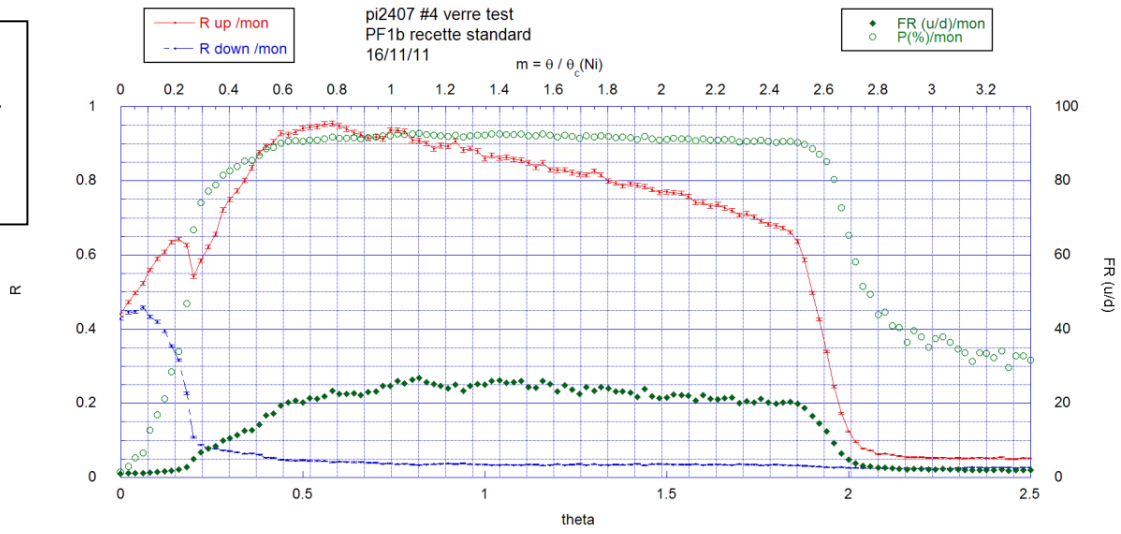


(b) Pseudo  $m=2.0$ ,  $100 \text{ \AA}$  spacing, sample M

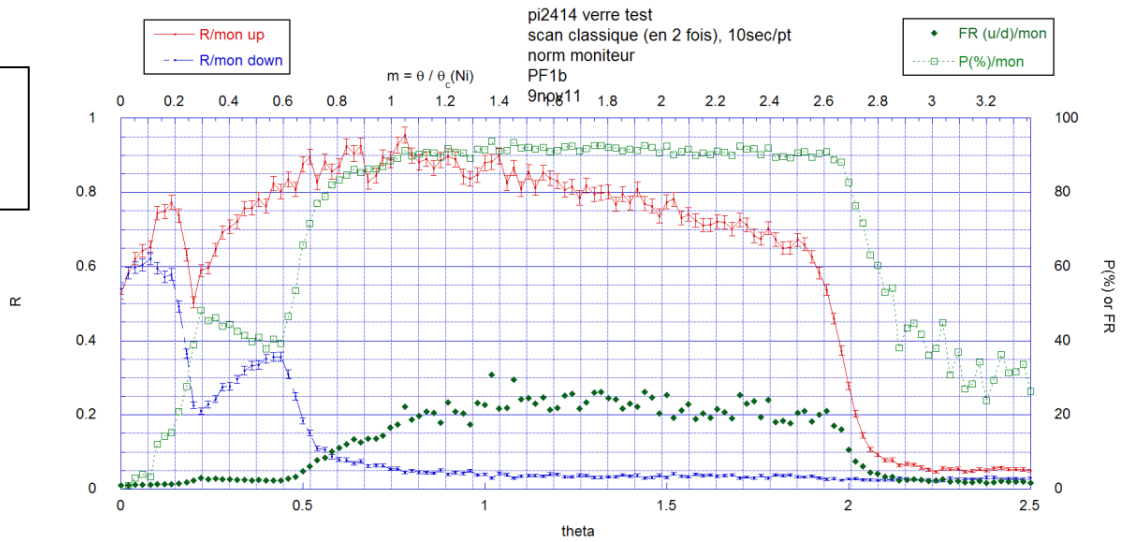




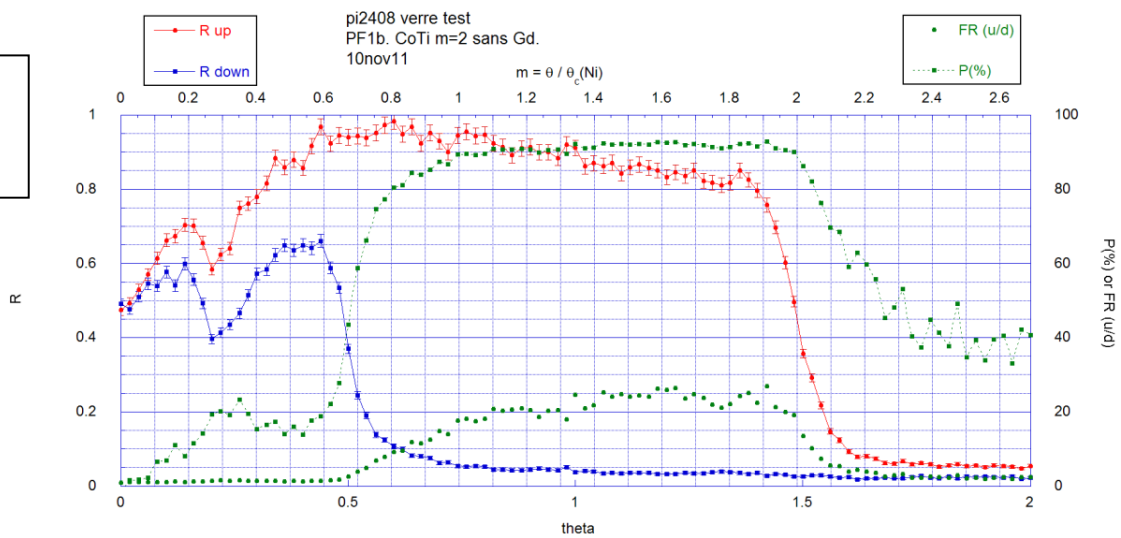
CoTi m=2.8  
with Gd layer  
Sample 5



CoTi m=2.8  
Sample 1



CoTi m=2.0  
Sample 3



# B

PERC in McStas

```

/*****INITIALIZE-Section*****/
R0_perc=0.99;
Qc_perc=0.0217;
waviness_perc=0.0115;

M_perc_tb=2.05;
M_perc_l =2.05;
M_perc_r =2.05;
alpha_perc_tb=2.305;
alpha_perc_l =2.305;
alpha_perc_r =2.305;
W_perc_tb=0.003;
W_perc_l =0.003;
W_perc_r =0.003;

plarm_selecteur=2.0017;
plarm_bender=1.725;
plarm_2e_guide=2.0;
plarm_perc=0;

/*****
/*****
/*****TRACE-Section: PERC Beamline*****/

COMPONENT arm_selecteur = Arm()
  AT (0,0,plarm_selecteur) RELATIVE AN19
  ROTATED (0,0,0) RELATIVE AN19

COMPONENT Blende=Slit(xmin=-0.03, xmax=0.03, ymin=-0.03, ymax=0.03)
AT (0,0,0.00001) RELATIVE arm_selecteur
ROTATED (0,0,0) RELATIVE arm_selecteur
/*****
COMPONENT Selektor=Selector(
xmin=-0.075, xmax=0.075, ymin=-0.0325, ymax=0.0325, len=0.25, num=72, width=0.0004, radius=0.145,
alfa=48.27, feq=424)
AT (0,0,0.0001)RELATIVE arm_selecteur
ROTATED (0,0,0) RELATIVE arm_selecteur

COMPONENT Osthalle_guide =Guide_wavy( //guide through wall (60 cm wall + 20)
  w1=0.06,h1=0.06,
  w2=0.06,h2=0.06,
  l=1.325,
  R0=R0_perc,
  Qc=Qc_perc,
  alpha1=alpha_perc_l,alpha2=alpha_perc_r,
  alpha3=alpha_perc_tb,alpha4=alpha_perc_tb,
  m1=M_perc_l,m2=M_perc_r,
  m3=M_perc_tb,m4=M_perc_tb,
  W1=W_perc_l,W2=W_perc_r,
  W3=W_perc_tb,W4=W_perc_tb,
  wavy_z=waviness_perc,
  wavy_xy=waviness_perc)

```

```
AT (0,0,0.4) RELATIVE arm_selecteur
ROTATED (0,0,0) RELATIVE arm_selecteur
```

```
/******
```

```
COMPONENT arm_bender=Arm()
  AT (0,0,plarm_bender) RELATIVE arm_selecteur
  ROTATED (0,0,0) RELATIVE arm_selecteur
COMPONENT Bender=Bender
(
w=0.08, h=0.08, r=30, l=0.8, k=29, d=0.00074,
R0a=0.99,
Qca=0.0217,
ma=M_pola,
alphaa =alpha_pola ,
Wa=W_pola,
R0i=0.99,
Qci=0.0217,
mi=M_pola,
alpha_i =alpha_pola,
Wi=W_pola,
R0a=0.99,
Qcs=0.0217,
ms=M_pola,
alphas =alpha_pola,
Ws=W_pola)
AT (0,0,0.0) RELATIVE arm_bender
ROTATED (0,0,0) RELATIVE arm_bender
```

```
COMPONENT Zwischenstruktur = Guide_wavy(
w1=0.06,h1=0.06,
w2=0.06,h2=0.06,
l=1.0,
R0=R0_perc,
Qc=Qc_perc,
alpha1=alpha_perc_l,alpha2=alpha_perc_r,
alpha3=alpha_perc_tb,alpha4=alpha_perc_tb,
m1=M_perc_l,m2=M_perc_r,
m3=M_perc_tb,m4=M_perc_tb,
W1=W_perc_l,W2=W_perc_r,
W3=W_perc_tb,W4=W_perc_tb,
wavy_z=waviness_perc,
wavy_xy=waviness_perc
)
AT (0,0,0.81) RELATIVE arm_bender
ROTATED (0,0,0) RELATIVE arm_bender
```

```
/******
```

```
/* Messpunkt vor PERC */
```

```
/******
```

```
COMPONENT arm_guide=Arm()
AT (0,0,plarm_2e_guide) RELATIVE arm_bender
ROTATED (0,0,0) RELATIVE arm_bender
```

```
COMPONENT APERC = Arm()
AT (0,0,plarm_perc) RELATIVE arm_guide
ROTATED(0,0,0) RELATIVE arm_guide
COMPONENT Inperc = PSD_monitor(
  xmin=-0.03, xmax=0.03,
  ymin=-0.03, ymax=0.03,
  nx=200, ny=200,
  filename="inperc.psd")
AT (0,0,0.0001) RELATIVE APERC
ROTATED (0,0,0) RELATIVE APERC
```

```
/******PERC*****
```

```
//1er
COMPONENT Perc_Leiter_1 = Guide_wavy(
  w1=0.06,h1=0.06,
  w2=0.06,h2=0.06,
  l=0.999,
  R0=R0_perc,
  Qc=Qc_perc,
  alpha1=alpha_perc_l,alpha2=alpha_perc_r,
  alpha3=alpha_perc_tb,alpha4=alpha_perc_tb,
  m1=M_perc_l,m2=M_perc_r,
  m3=M_perc_tb,m4=M_perc_tb,
  W1=W_perc_l,W2=W_perc_r,
  W3=W_perc_tb,W4=W_perc_tb,
  wavy_z=waviness_perc,
  wavy_xy=waviness_perc
)
AT (0,0,0.01) RELATIVE APERC
ROTATED (0,0,0) RELATIVE APERC
```

```
//2e
COMPONENT Perc_Leiter_2 = Guide_wavy(
  w1=0.06,h1=0.06,
  w2=0.06,h2=0.06,
  l=0.999,
  R0=R0_perc,
  Qc=Qc_perc,
  alpha1=alpha_perc_l,alpha2=alpha_perc_r,
  alpha3=alpha_perc_tb,alpha4=alpha_perc_tb,
  m1=M_perc_l,m2=M_perc_r,
  m3=M_perc_tb,m4=M_perc_tb,
  W1=W_perc_l,W2=W_perc_r,
  W3=W_perc_tb,W4=W_perc_tb,
```

```

wavy_z=waviness_perc,
wavy_xy=waviness_perc
//, nz=80, filename="absorbed.psd",nchan=84, Lmin=0.2, Lmax=17.0, mon_fichier="absorbed_wavelength.psd",
//ndiv=50, maxdiv=7, my_divergence_file="absorbed_divergence.psd"
)
AT (0,0,0.01+1.0) RELATIVE APERC
ROTATED (0,0,0) RELATIVE APERC
//3e
COMPONENT Perc_Leiter_3 = Guide_wavy(
w1=0.06,h1=0.06,
w2=0.06,h2=0.06,
l=0.999,
R0=R0_perc,
Qc=Qc_perc,
alpha1=alpha_perc_l,alpha2=alpha_perc_r,
alpha3=alpha_perc_tb,alpha4=alpha_perc_tb,
m1=M_perc_l,m2=M_perc_r,
m3=M_perc_tb,m4=M_perc_tb,
W1=W_perc_l,W2=W_perc_r,
W3=W_perc_tb,W4=W_perc_tb,
wavy_z=waviness_perc,
wavy_xy=waviness_perc
//,nz=80, filename="absorbed.psd",nchan=84, Lmin=0.2, Lmax=17.0, mon_fichier="absorbed_wavelength.psd",
//ndiv=50, maxdiv=7, my_divergence_file="absorbed_divergence.psd"
)
AT (0,0,0.01+2.0) RELATIVE APERC
ROTATED (0,0,0) RELATIVE APERC

//4e
COMPONENT Perc_Leiter_4 = Guide_wavy(
w1=0.06,h1=0.06,
w2=0.06,h2=0.06,
l=0.999,
R0=R0_perc,
Qc=Qc_perc,
alpha1=alpha_perc_l,alpha2=alpha_perc_r,
alpha3=alpha_perc_tb,alpha4=alpha_perc_tb,
m1=M_perc_l,m2=M_perc_r,
m3=M_perc_tb,m4=M_perc_tb,
W1=W_perc_l,W2=W_perc_r,
W3=W_perc_tb,W4=W_perc_tb,
wavy_z=waviness_perc,
wavy_xy=waviness_perc
//,nz=80, filename="absorbed.psd",nchan=84, Lmin=0.2, Lmax=17.0, mon_fichier="absorbed_wavelength.psd",
//ndiv=50, maxdiv=7, my_divergence_file="absorbed_divergence.psd"
)
AT (0,0,0.01+3.0) RELATIVE APERC
ROTATED (0,0,0) RELATIVE APERC

//5e
COMPONENT Perc_Leiter_5 = Guide_wavy(
w1=0.06,h1=0.06,
w2=0.06,h2=0.06,

```

```

l=0.999,
R0=R0_perc,
Qc=Qc_perc,
alpha1=alpha_perc_l,alpha2=alpha_perc_r,
alpha3=alpha_perc_tb,alpha4=alpha_perc_tb,
m1=M_perc_l,m2=M_perc_r,
m3=M_perc_tb,m4=M_perc_tb,
W1=W_perc_l,W2=W_perc_r,
W3=W_perc_tb,W4=W_perc_tb,
wavy_z=waviness_perc,
wavy_xy=waviness_perc
//, nz=80, filename="absorbed.psd",nchan=84, Lmin=0.2, Lmax=17.0, mon_fichier="absorbed_wavelength.psd",
//ndiv=50, maxdiv=7, my_divergence_file="absorbed_divergence.psd"
)
AT (0,0,0.01+4.0) RELATIVE APERC
ROTATED (0,0,0) RELATIVE APERC

//6e
COMPONENT Perc_Leiter_6 = Guide_wavy(
w1=0.06,h1=0.06,
w2=0.06,h2=0.06,
l=0.999,
R0=R0_perc,
Qc=Qc_perc,
alpha1=alpha_perc_l,alpha2=alpha_perc_r,
alpha3=alpha_perc_tb,alpha4=alpha_perc_tb,
m1=M_perc_l,m2=M_perc_r,
m3=M_perc_tb,m4=M_perc_tb,
W1=W_perc_l,W2=W_perc_r,
W3=W_perc_tb,W4=W_perc_tb,
wavy_z=waviness_perc,
wavy_xy=waviness_perc
//, nz=80, filename="absorbed.psd",nchan=84, Lmin=0.2, Lmax=17.0, mon_fichier="absorbed_wavelength.psd",
//ndiv=50, maxdiv=7, my_divergence_file="absorbed_divergence.psd"
)
AT (0,0,0.01+5.0) RELATIVE APERC
ROTATED (0,0,0) RELATIVE APERC

//7e
COMPONENT Perc_Leiter_7 = Guide_wavy(
w1=0.06,h1=0.06,
w2=0.06,h2=0.06,
l=0.999,
R0=R0_perc,
Qc=Qc_perc,
alpha1=alpha_perc_l,alpha2=alpha_perc_r,
alpha3=alpha_perc_tb,alpha4=alpha_perc_tb,
m1=M_perc_l,m2=M_perc_r,
m3=M_perc_tb,m4=M_perc_tb,
W1=W_perc_l,W2=W_perc_r,
W3=W_perc_tb,W4=W_perc_tb,
wavy_z=waviness_perc,

```

```

wavy_xy=waviness_perc
//, nz=80, filename="absorbed.psd",nchan=84, Lmin=0.2, Lmax=17.0, mon_fichier="absorbed_wavelength.psd",
//ndiv=50, maxdiv=7, my_divergence_file="absorbed_divergence.psd"
)
AT (0,0,0.01+6.0) RELATIVE APERC
ROTATED (0,0,0) RELATIVE APERC

// 8e
COMPONENT Perc_Leiter_8 = Guide_wavy(
w1=0.06,h1=0.06,
w2=0.06,h2=0.06,
l=0.999,
R0=R0_perc,
Qc=Qc_perc,
alpha1=alpha_perc_l,alpha2=alpha_perc_r,
alpha3=alpha_perc_tb,alpha4=alpha_perc_tb,
m1=M_perc_l,m2=M_perc_r,
m3=M_perc_tb,m4=M_perc_tb,
W1=W_perc_l,W2=W_perc_r,
W3=W_perc_tb,W4=W_perc_tb,
wavy_z=waviness_perc,
wavy_xy=waviness_perc
//, nz=80, filename="absorbed.psd",nchan=84, Lmin=0.2, Lmax=17.0, mon_fichier="absorbed_wavelength.psd",
//ndiv=50, maxdiv=7, my_divergence_file="absorbed_divergence.psd"
)
AT (0,0,0.01+7.0) RELATIVE APERC
ROTATED (0,0,0) RELATIVE APERC

```



# Acknowledgements

Many people have contributed to this thesis in various ways. My thanks belong to

Torsten Soldner who has largely supervised this thesis for his continuous support of the project. I am grateful for his guidance in all the time of research, his patience and experimental experience.

Hartmut Abele for giving me the opportunity to conduct this work as his thesis student.

Klaus Kirch for accepting to be the second referee.

The ILL's Service Optique de Neutrons. Thierry Bigault and Pierre Courtois helped with the conception of the experiment and provided various mirror samples. David Jullien, Pascal Mouveau and Antonello Rizzo provided well-polarized helium cells and a smile at every moment during beamtimes. Amandine Vittoz measured the reflectivity profiles on T3. Jérémie Chastagnier helped with the set-up of the 2010 beamtime, repaired a neutron spin-flipper electronics on the fly and helped with the field map of the ADAM-Magnet.

Anton Devishvili who made beamtime on the SuperADAM instrument possible and helped with its data analysis. He also patiently answered any questions I had about magnetism and neutron scattering and discussion with him was always fruitful.

My colleagues from the NPP group at ILL, Grenoble. In particular Didier Berruyer for the manufacturing of the sample holder and a nightly repair of the leaking magnet cooling system, Sasha Petoukhov for discussion, Martin Simson for several small reparations and correcting this thesis, Thomas Brenner for help with the Gd paint and Oliver Zimmer for lending me a Gaussmeter and correcting this thesis.

My colleagues from the Abele group in Vienna, in particular Jacqueline Erhart, Christoph Gösselsberger, Erwin Jericha and Gertrud Konrad.

Despite the physical distance between Grenoble and Vienna, I always felt welcome in the group and they helped me navigate the mysterious jungle that is a university's administration.

Jens Klenke from FRMII for introducing me to McStas, his help with my first steps, a basic McStas version of the PERC-Beamline and a realistic view on the world of neutron physics.

Peter Böni and Michael Schneider from SwissNeutronics. They kindly provided a test series of FeSi and FeCoV mirrors. Thorsten Lauer from Mainz University who provided a FeSi mirror and two Fe monolayers.

Daniel Bourgault from the laboratoire CRETA at CNRS who kindly measured the SQUID hysteresis curves for a Fe and a Co monolayer. Bastian Märkisch, Utz Schmidt and Frédéric Ott for discussion.

Anne Stunault from D3 for lending me her magnet, Sébastien Vial for helping me with its transport and installation and Frédéric Thomas from the Bureau d'Etudes for quick calculation of field maps for polar inserts for the D3 magnet.

Nataliya Rebrova for her help during the 2011 beamtime and insights on the fabrication of supermirrors, Pilar Guimerà Millàn for her help and a croissant during the 2012 beamtime and Daniel Payne for his help with the measurement of the field map of the D3 electro-magnet.

The Deutsche Forschungsgesellschaft which has given the financial support for this thesis through SSP 1491 project SO 1058/1-1.

Jacqueline and Felix. Pour tout ce qui reste.

Thank you.

# Christine Klauser

## Education

- 04.2011-11.2013 Technische Universität Wien (A), PhD student  
09.2008- 03.2010 Ecole Polytechnique Fédérale de Lausanne (CH): **MSc of Physics**  
(ingénieur-physicien dipl. EPF)  
Master thesis: *Analysis of ERANOS Modelling of The Gas-Fast Reactor Demonstrator ALLEGRO In Comparison to TRIPOLI*  
09.2007-05.2008 University of Waterloo(CA): undergraduate studies in Physics (exchange)  
09.2005- 08.2008 Ecole Polytechnique Fédérale de Lausanne (CH): **Bachelor of Physics**  
08.2001-07.2005 Kantonsschule Trogen (CH): **eidgenössische Matura**

## Experience

- 12.2010-11.2013 PhD student at Institut Laue-Langevin, Grenoble (F) , Nuclear and Particle Physics group  
06.2010-11.2010 scientific assistant at Technische Universität München (D), Institut für Experimentalphysik E18  
09.2008-06.2009 Student assistant at Ecole Polytechnique Fédérale de Lausanne (CH)  
06.2008 -08.2008 Internship at Eidgenössisch-Technische Universität Zürich (CH), Labor für Kernenergiesysteme

## Peer-reviewed publications

- C. Klauser et al, 2012 *J. Phys.: Conf. Ser.* 340 012011  
*High precision depolarisation measurements with an opaque test bench*  
<http://iopscience.iop.org/1742-6596/340/1/012011/>
- C. Klauser et al, *Physics Procedia PNCMI 2012 - Polarized Neutrons for Condensed Matter Investigations 2012,*  
*Ultra-Sensitive Depolarization Study of Polarizing CoTi Supermirrors with the Opaque Test Bench*  
<http://dx.doi.org/10.1016/j.phpro.2013.03.181>
- G. Konrad et al, 2012 *J. Phys.: Conf. Ser.* 340 012048  
*Neutron Decay with PERC: a Progress Report*  
<http://iopscience.iop.org/1742-6596/340/1/012048/>
- C. Klauser et al, *Physics Procedia NPPat LPS 2013,*  
*Beam Line Parameters for PERC at the Long-Pulse Spallation Source ESS (accepted)*

## Languages

- German: native  
French: outstanding (C2)  
English: excellent (C1)